

Long Spin Lifetime in Rare-Earth Single-Atom Magnets at Surfaces

Présentée le 29 septembre 2022

Faculté des sciences de base
Laboratoire de nanostructures superficielles
Programme doctoral en physique

pour l'obtention du grade de Docteur ès Sciences

par

Boris SOROKIN

Acceptée sur proposition du jury

Prof. F. Mila, président du jury
Dr S. Rusponi, Prof. H. Brune, directeurs de thèse
Prof. H. Wende, rapporteur
Dr R. Westerström, rapporteur
Prof. D. Grundler, rapporteur

Acknowledgements

First and foremost, I would like to express my heartfelt gratitude to my thesis advisor Dr. Stefano Rusponi. I deeply appreciate his devoted involvement in this project and his patience with which he answered all my innumerable questions. I'm equally thankful to Prof. Dr. Harald Brune for giving me the opportunity to be a part of his group and co-directing my thesis. My sincere gratitude goes to Dr. Marina Pivetta for her invaluable support throughout my years at EPFL. I would also like to thank Dr. Alessandro Barla for his knowledge and wisdom he shared with me during our numerous joint beamtimes.

My life at EPFL would not be so smooth trouble-free without the impeccable job of our secreteris Nathalie Guex and Carole Pascalon, many thanks go to them. Besides, I highly appreciate all my group mates with whom I had the pleasure of spending such wonderful time; Alberto Curcella, Johannes Schwenk, Dante Sblendorio, Darius Merk, Sébastien Reynaud, Clément Soulard, Jean-Guillaume de Groot, Tobias Bilgeri, Fabian Natterer, Aparajita Singha, Hao Yin, Edgar Fernandes and others.

Last but not least, I genuinely thank my entire family for their support and patience during this long-lasting project. Without them I would never be where I am right now. Especially, I would like to thank my wife Vera, who was there for me all these years.

Lausanne, June 1, 2022

B. S.

Abstract

Further miniaturisation of magnetic storage devices requires an advent of new types of magnets, since classical ferromagnetic materials show lack of remanence at nano- and sub-nanoscale. A single atom can represent the smallest possible bit of information. Even though the isolated single atoms are paramagnetic, the interaction of surface adsorbed atoms with a substrate can result in high magnetic anisotropy energy and long magnetisation lifetime. In this thesis the magnetic properties of surface supported rare-earth single atoms are investigated with X-ray absorption spectroscopy, X-ray magnetic circular dichroism and multiplet simulations. The first goal of the project was to find new adatom/substrate combinations that exhibit a long adatom magnetic lifetime, possibly extending the current limits of the atomic magnetic moment stability to higher temperatures and longer spin relaxation times. The second objective was to implement the external electric field control of the adatom magnetic properties.

Firstly, we present the experimental and theoretical research on Dy and Ho single atoms deposited on BaO. A comparison of our results with similar studies sheds light on the impact of the substrate crystal field, in particular Dy-O bond covalency, on the magnetic stability of the rare-earth adatoms. Next, the detailed experimental investigation of Dy single atoms on ZnO is presented. This adatom/substrate pair is used as first attempt to implement the electric field control of the adatom magnetic properties. Lastly, we study the Dy adatoms on graphene layers grown on various metals. The vibrational modes of the metallic substrates are shown to strongly affect the Dy spin lifetime, while addition of a second graphene layer does not allow to significantly improve the adatom magnetic stability.

Key words: single-atom magnets, rare-earth atoms, dysprosium, X-ray absorption spectroscopy, X-ray magnetic circular dichroism, multiplet simulations

Résumé

Une miniaturisation plus poussée des appareils de mémoire magnétique nécessite l'apparition de nouveaux types d'aimants, car les matériaux ferromagnétiques classiques présentent un manque de rémanence à l'échelle nanométrique et subnanométrique. Un seul atome peut représenter le plus petit bit d'information possible. Même si les atomes isolés sont paramagnétiques, l'interaction des atomes adsorbés en surface avec un substrat peut entraîner une énergie d'anisotropie magnétique élevée et une longue durée de vie de l'aimantation. Dans cette thèse, les propriétés magnétiques des atomes isolés de terres rares supportés en surface sont étudiées par spectroscopie d'absorption des rayons X, dichroïsme circulaire magnétique des rayons X et simulations de multiplets. Le premier objectif du projet était de trouver de nouvelles combinaisons adatome/substrat qui présentent une longue durée de vie magnétique de l'adatome, en étendant possiblement les limites actuelles de la stabilité du moment magnétique atomique à des températures plus élevées et à des temps de relaxation de spin plus longs. Le second objectif était de mettre en œuvre le contrôle par champ électrique externe des propriétés magnétiques de l'adatome.

Tout d'abord, nous présentons la recherche expérimentale et théorique sur les atomes isolés de Dy et Ho déposés sur BaO. Une comparaison de nos résultats avec des études similaires met en évidence l'impact du champ cristallin du substrat, en particulier la covalence de la liaison Dy-O, sur la stabilité magnétique des adatoms de terres rares. Ensuite, l'étude expérimentale détaillée des atomes isolés de Dy sur ZnO est présentée. Cette paire adatome/substrat est utilisée comme première tentative pour mettre en œuvre le contrôle par champ électrique des propriétés magnétiques de l'adatome. Enfin, nous étudions les adatoms de Dy sur des couches de graphène croissant sur différents métaux. Nous montrons que les modes vibrationnels des substrats métalliques affectent fortement la durée de vie du spin du Dy, tandis que l'ajout d'une seconde couche de graphène ne permet pas d'améliorer significativement la stabilité magnétique de l'adatome.

Mots clés : aimants à un unique atome, atomes de terres rares, dysprosium, spectroscopie d'absorption des rayons X, dichroïsme circulaire magnétique des rayons X, simulations de multiplets.

Contents

Acknowledgements	i
Abstract (English/Français/Deutsch)	iii
List of Figures	ix
List of Tables	xi
Introduction	1
1 The Fundamental Principles of Single-Atom Magnets	5
1.1 Magnetism of a free atom	5
1.2 Substrate-adatom interaction	8
1.2.1 Stevens operators	10
1.2.2 Quantum tunnelling of magnetisation	11
1.3 Conclusion	12
2 Methods	13
2.1 X-ray absorption spectroscopy	13
2.2 X-ray magnetic circular dichroism	14
2.3 X-ray magnetic linear dichroism	16
2.4 EPFL/PSI X-Treme beamline	16
2.5 Total electron yield	17
2.6 Experimental geometry and data analysis	18
2.7 Multiplet calculations	19
3 Magnetic stability of Dy and Ho single atoms on BaO	21
3.1 Main text	22
3.1.1 Introduction	22
3.2 Results and discussion	22
3.2.1 Conclusion	32
3.2.2 Methods	32
3.3 Supporting information	33
3.3.1 BaO thin film characterisation	33
3.3.2 Additional results of multiplet simulations	35

Contents

3.3.3	DFT calculations: simulation cell	36
3.4	Conclusion and outlook	36
4	Electric field control of single atom spin lifetime	39
4.1	ZnO thin films on Au(111) single crystals	41
4.2	Dy single atoms on ZnO/Au(111)	42
4.2.1	Dy coverage dependence	44
4.2.2	ZnO-thickness dependence	46
4.2.3	Dy magnetic relaxation times	47
4.2.4	Temperature dependence	48
4.3	Ho single atoms on ZnO/Au(111)	49
4.4	ZnO thin films on SrTiO ₃ (110) single crystals	49
4.4.1	Characterisation of ZnO/STO(110) films for field effect measurements .	51
4.5	Dy single atoms on ZnO/STO(110)	52
4.5.1	Electric field control of the Dy magnetic lifetime	52
4.6	Conclusion and outlook	54
5	Electron and Phonon Induced Demagnetisation of Single-Atom Magnets	57
5.1	Substrates preparation and characterisation	58
5.2	X-ray absorption spectra	59
5.3	Magnetisation curves	60
5.4	CF level splitting and external subshell occupation	62
5.5	Substrate electron- and phonon-assisted spin relaxation	64
5.6	Conclusion and outlook	65
	Conclusions and Outlook	67
A	Bader charges and atom coordinates for RE/BaO and RE/MgO	69
A.1	DFT calculations	69
A.2	CF point charges used in the multiplet calculations	73
	Bibliography	75
	Curriculum Vitae	

List of Figures

1.1	Stabilisation of atomic magnetic moment by crystal field	9
1.2	Mechanism of quantum tunnelling of magnetisation	11
2.1	Typical Dy ³⁺ XAS spectrum	13
2.2	Typical Dy ³⁺ XMCD spectrum	14
2.3	Schematic representation of the X-Treme beamline end station	17
3.1	X-ray spectra, magnetisation and relaxation curves of Dy atoms on BaO/Pt(100)	23
3.2	X-ray spectra and magnetisation curves of Ho atoms on BaO/Pt(100)	24
3.3	Charge density isosurfaces for Dy adatoms on top-O and bridge sites on BaO and MgO	26
3.4	Schematic representation of RE adsorption sites on BaO; XMCD angular dependence of Dy on BaO	27
3.5	Energy diagrams of the lowest energy multiplets for Dy ^{top} and Dy ^{br-xz}	28
3.6	Energy diagrams of the lowest energy multiplets for Ho ^{top} and Ho ^{br-xz}	31
3.7	LEED images of Pt(100) single crystal and BaO(100) thin film	34
3.8	XLD spectrum of BaO at O K-edge	34
3.9	Energy diagrams of the bridge species lowest J-multiplets	35
3.10	Simulation cells for RE adatoms on BaO (or MgO) surface	37
4.1	ZnO wurtzite crystal structure	40
4.2	LEED image of a ZnO/Au(111)	41
4.3	XLD spectra of a ZnO/Au(111)	42
4.4	X-ray spectra and magnetisation curves of Dy atoms on ZnO/Au(111)	43
4.5	Coverage dependence of XAS and XMCD spectra for Dy/ZnO/Au(111)	44
4.6	Coverage dependence of XMLD spectrum for Dy/ZnO/Au(111)	45
4.7	Coverage dependence of magnetisation curves for Dy/ZnO/Au(111)	46
4.8	ZnO-thickness dependence of magnetisation curves for Dy/ZnO/Au(111)	46
4.9	Spin relaxation dynamics of Dy/ZnO/Au(111)	47
4.10	Temperature dependence of the magnetisation curve for Dy/ZnO/Au(111)	49
4.11	X-ray spectra and magnetisation curves of Ho atoms on ZnO/Au(111)	50
4.12	ZnO/STO(110) sample in a sample holder	51
4.13	Field effect in ZnO/STO(110)	52
4.14	X-ray spectra and magnetisation curves of Dy atoms on ZnO/STO(110)	53

List of Figures

4.15 Dependence of the Dy XMCD signal on the external electric field	54
4.16 Dependence of the Dy hysteresis loops on the external electric field	54
4.17 Ferroelectric hysteresis loop of a ZnO/STO(110)	55
5.1 STM images of graphene/Cu	58
5.2 XLD spectra of graphene/Cu at C K-edge	59
5.3 X-ray spectra of Dy atoms on graphene/metals.	60
5.4 Magnetisation curves of Dy atoms on graphene/metals	61
5.5 Energy diagrams of the lowest Dy states	62
5.6 Spin resolved DOS of 5d and 6s electrons of Dy atoms on gr/Cu(100) and gr/Cu(111)	63
5.7 Single layer and bilayer graphene phonon energy dispersions	64

List of Tables

1.1	Ground multiplet quantum numbers of Dy and Ho atoms.	8
3.1	Total energies of Dy and Ho on BaO and MgO substrates for the top-O and bridge adsorption sites	25
4.1	Coverage dependence of Dy magnetic moments for Dy/ZnO/Au(111)	45
A.1	DFT simulated coordination shells around Dy adatom on top-O adsorption site on BaO	69
A.2	DFT simulated coordination shells around Dy adatom on bridge adsorption site on BaO	70
A.3	DFT simulated coordination shells around Ho adatom on top-O adsorption site on BaO	70
A.4	DFT simulated coordination shells around Ho adatom on bridge adsorption site on BaO	71
A.5	DFT simulated coordination shells around Dy adatom on top-O adsorption site on MgO	71
A.6	DFT simulated coordination shells around Dy adatom on bridge adsorption site on MgO	72
A.7	DFT simulated coordination shells around Ho adatom on top-O adsorption site on MgO	72
A.8	DFT simulated coordination shells around Ho adatom on bridge adsorption site on MgO	73
A.9	CF point charges for RE adatoms on BaO	73

Introduction

Already ancient Greeks came up with the idea that the matter consists of tiny particles, which they called *atomos*. The literal translation is ‘indivisible’. Nowadays we call them atoms. The modern concept of an atom was devised in the beginning of the 20th century by a New Zealander Ernest Rutherford in his famous ‘gold foil experiment’ [1]. Since then we have learnt a lot about these once mysterious particles, including a fairly accurate quantum mechanical description of their structure. The present-day periodic table contains 118 different elements and the process of search and creation of new atoms is going on [2]. Particle beams were used in early experiments with isolated atoms [1, 3, 4]. With modern technology we are able to capture and store both charged atomic ions in ion traps [5, 6] and neutral single atoms in magneto-optical traps [7]. The first prototypes of quantum devices based on trapped single atoms have been realised using these capturing methods [8–11].

An important role in the current scientific research is dedicated to surface adsorbed single atoms. The advent of atomic resolution microscopies (scanning tunnelling microscopy (STM) [12], atomic force microscopy (AFM) [13] and aberration corrected transmission electron microscopy (TEM) [14]) resulted in images with atomic resolution of, first, crystal lattices and, later, surface adsorbed single atoms. The same experimental tools can be utilised to control the position of the adatoms on the surface. The atomic manipulation was first demonstrated with a help of STM in 1990 [15]. Moreover, STM does not only allow to study the topography of the samples but also to investigate the excitation states. The latter technique is called the scanning tunnelling spectroscopy (STS). The main limitation of the STM and STS methods is that they are only applicable to conducting surfaces. Nevertheless, the atomic manipulation on an insulating substrate has also been recently achieved with AFM technique [16], while TEM was used to engineer a single atom dynamics with electron irradiation [17]. X-ray spectroscopy is another appropriate method for studies of surface adsorbed single atoms. Its elemental selectivity together with the high sensitivity of total electron yield detection scheme allows to measure surface coverages as low as 0.5% of a monolayer, while circularly polarised X-ray photons can provide information about adatom spin and orbital magnetic moments non-accessible directly to other techniques [18, 19].

In the last three decades, surface adsorbed single atoms and atomic clusters have been extensively studied as prototypical systems for quantum devices and due to the high scientific importance of their fundamental properties. This research can be divided into two main

topics: single-atom magnetism [20–22] and single-atom catalysis [23, 24]. In the following we will focus on the magnetic properties of surface adatoms, since they represent the topic of this work. The magnetic excitations of various atomic clusters have been studied with both STS and X-rays [25–30]. A linear chain of atoms can be considered as a special case of an atomic cluster that is very helpful in verification of fundamental principles of adatom interactions, hence, such systems have attracted heightened attention [31–37]. Furthermore, the measurement of Ruderman–Kittel–Kasuya–Yosida exchange interaction between single atoms has been performed [29, 37–39]. Loth and co-workers were able to demonstrate control of the adatom magnetic quantum state with electric current in STM experimental setup [40], while Khajetoorians *et al.* have realised an atomic-spin-based logic gate [41]. One should separately mention a series of works based on ESR-STM. This is a newly developed experimental technique that utilises a spin polarised STM tip to excite and detect an electron spin resonance in an isolated surface atom [42, 43]. ESR-STM method was used to measure the magnetic dipolar and exchange interactions between single atoms [44–49], their quantum coherence [50–52], hyperfine structure [53, 54], resonating valence bond states in artificial quantum magnets [55], and to perform magnetic resonance imaging of single atoms [56].

One of the most important parameters of magnetic objects for practical applications is the magnetisation lifetime. It characterises the magnetic stability of the object or, in other words, the rate at which the magnetisation decays towards its equilibrium value. The so-called exchange interaction helps to stabilise the orientation of the individual atomic magnetic moments and, consequently, to retain the net magnetisation of the bulk ferromagnetic samples for years [57]. Thereby, such magnetic materials are extensively used in information storage. Nevertheless, the overall trend towards minituarisation of information processing devices and the advent of new quantum computing technologies call for a significant increase in information storage density or, equivalently, for a size reduction of magnetic bits [58]. In bulk ferromagnets each atom contributes for a certain degree to the stability of the whole magnet. The relatively low number of atoms in nano- and subnanoscale objects leads to a degradation of their magnetic stability, thus, one should find new ways to obtain long magnetic moment lifetime for such systems. There exists two viable paths to pursuit this goal. In the first approach one concentrates on nanoscaled obojects at the borderline between the classical and quantum description in an attempt to either preserve the classical magnetic behaviour or make use of the emerging quantum phenomena. This is for example the case of skyrmions, which are the topologically protected nanoscale magnetic quasiparticles [59, 60]. The other approach consists in the stabilisation of magnetic moments of isolated single atoms or small atomic clusters, so that they can function as single bits of information [20–22]. The magnetic moment of a single atom can be stabilised by either encapsulation into a molecular shell [61–80] or adsorbtion onto a surface [20–22, 46, 49, 81–90]. In the first case one speaks about single-molecule magnets (SMMs, or single-ion magnets (SIMs) if the magnetic core consists of a single ion), while the second type of systems is called single-atom magnets (SAMs).

In the beginning, the research on SAMs was focused on the 3d transition metal elements

[86, 88, 91–102]. The work of Rau and co-workers [88], where the magnetic anisotropy limit imposed by spin-orbit interaction was reached for Co single atoms, is a highlight of this research. Nonetheless, the magnetic lifetime of Co atoms was found to be only $\approx 230 \mu\text{s}$. A breakthrough was achieved in 2016 with the help of rare-earth (RE) elements [81, 83]. X-ray spectroscopy measurement showed that Ho single atoms adsorbed on MgO thin films exhibit magnetic remanence up to 30 K and a relaxation time of $\approx 1500 \text{ s}$ at 10 K [83]. An STM study of the same system revealed a coercive field of more than 8 T and magnetic bistability for many minutes, both at 35 K [87]. The possibility to read and write the magnetic moment of Ho SAMs has also been demonstrated [49], while their magnetic stability has been studied in a wide range of magnetic fields between 0 T and 8 T [84, 85]. At the same time, Dy single atoms self-assembled into a superlattice on graphene grown on Ir(111) surface show magnetic lifetime of $\approx 1000 \text{ s}$ at 2.5 K [81]. The most stable SAM up to now, whose magnetic lifetime exceeds days at $\approx 1 \text{ K}$, is a Dy atom adsorbed on top of O on MgO thin film, as has been demonstrated with the help of ESR-STM [46]. The correlation between its electronic configuration and magnetic stability has been also shown [82].

In this work we pursued two goals. First, we searched for new adatom/substrate combinations that can serve as SAMs. The new systems should shed light on the adatom-substrate interaction and enhance our understanding of the magnetic moment stabilisation together with the ability to predict new promising candidates for SAMs. We also aim to extend the magnetic stability of single atoms to higher temperatures and longer relaxation times. The second objective of the project is to demonstrate the possibility of the electric field control of the SAM spin. Indeed, to be used in the modern magnetic memory devices single-atom bits should not only preserve their magnetic moment for a sufficiently long period of time, but also allow an externally controlled spin flipping. To this end, magnetic fields are currently employed in present-day magnetic hard disk drives. However, it is very hard to localise the magnetic field on a single atom, while magnetic field production involves an electric current flowing through a resistive circuit, which is inevitably associated with the high energy consumption and Joule heating. Furthermore, slow writing speed is one of the main reasons why hard disk drives are currently losing the competition to the solid-state drives on the market of personal computers. All these limitations can be overcome with the electric field manipulation of magnetism [103]. In particular, ferroelectricity and field effect are two viable routes to achieve the electric field control of SAMs.

As the main experimental tools we employed the X-ray spectroscopy techniques, namely X-ray absorption spectroscopy (XAS), X-ray magnetic circular dichroism (XMCD) and X-ray magnetic linear dichroism (XMLD). To rationalise the experimental data the multiplet calculations using the multiX code were performed [104].

The thesis is organised as follows:

In Chapter 1 the main fundamental principles of SAMs are introduced. The magnetic properties of free atoms as well as adatom-substrate interaction are discussed. In this chapter we

Introduction

introduce the concepts of Stevens operators and quantum tunnelling of magnetisation, and also discuss their relation to the magnetic stability of SAMs.

Chapter 2 describes the experimental and computational methods used in this work. The basics of XAS, XMCD and XMLD spectroscopies are discussed. In this chapter we also describe the experimental setup, measurement configurations and details of the data analysis. The basic principles of the multiplet calculations are introduced at the end of the chapter.

In Chapter 3 we attempted to optimise the crystal field (CF) at the adatom position by using the BaO supporting substrate, which has a very similar crystal structure to MgO, but exhibit a different charge distribution between O and alkaline earth metal. This chapter is based on the manuscript ‘Magnetic Stability of Dy and Ho Single Atoms on Alkaline Earth Oxides’, which was prepared for the publication. In this manuscript we discuss in detail the magnetic properties of Dy and Ho SAMs on BaO/Pt(100) thin films and compare the results to the similar studies of Dy and Ho SAMs on MgO. Further, the influence of the Dy-O bond covalency on the magnetic stability is elaborated.

Chapter 4 is dedicated to the Dy single atoms deposited on ZnO, which is expected to exhibit the desired axial CF. In addition, the non-centrosymmetric wurtzite structure and the semi-conducting electronic properties of ZnO could open the way to an electric field control of the magnetic properties of individual surface supported atoms. Firstly, the detailed experimental study of the magnetic properties of Dy deposited on ZnO/Au(111) thin films is presented. Then, the possibility of the electric field control of the adatom magnetic properties via field effect for Dy/ZnO/STO(110) system is discussed.

In Chapter 5 we show the influence of the substrate conduction electrons and phonons on the magnetic stability of Dy SAMs. To this end we compare the magnetic properties of Dy on graphene grown on three different metals. The difference between single layer and bilayer graphene as substrates for SAMs is also discussed.

Finally, the summary of the main results together with the future perspective is presented at the end of the thesis.

1 The Fundamental Principles of Single-Atom Magnets

1.1 Magnetism of a free atom

Magnetic properties of an isolated atom are defined by its magnetic moment. The latter consists of two components: a nuclear magnetic moment and the resultant magnetic moment of the surrounding electrons. The electron magnetic moment has an order of magnitude of the Bohr magneton

$$\mu_B = \frac{|e|\hbar}{2m_e} = 5.79 \times 10^{-5} \text{ eV/T} = 9.27 \times 10^{-24} \text{ J/T}, \quad (1.1)$$

where e is the electron charge, $\hbar = \frac{h}{2\pi}$ is the reduced Planck constant and m_e is the electron mass. The analogous expression for the nuclear magnetic moment can be derived by a substitution of the electron mass m_e by the proton mass m_p . The corresponding physical constant is called the nuclear magneton

$$\mu_N = \frac{|e|\hbar}{2m_p} = 3.15 \times 10^{-8} \text{ eV/T} = 5.05 \times 10^{-27} \text{ J/T}. \quad (1.2)$$

Since protons are approximately 2000 times heavier than electrons, the electron magnetic moment is much stronger than its nuclear counterpart. Further we will focus on the magnetic moment created by the atomic electrons as it is exactly this moment that one stabilises in single-atom magnets.

The magnetic moments are closely related to the angular momentum via a so-called gyro-magnetic ratio γ , hence we will first describe the physics of the atomic angular momentum and then show how one can use it to calculate the atomic magnetic moment. Each electron has an orbital angular momentum \mathbf{L} , which is the consequence of its circular motion around the atomic nucleus, and a spin angular momentum¹ \mathbf{s} intrinsic for an electron (just like a charge or a mass). The spin of the elemental particles has a quantum relativistic nature and, thus, cannot be explained by classical physics or derived from the Schrödinger equation. The

¹For brevity it is often simply called a 'spin'.

strict theoretical description of the spin was performed by Dirac in his relativistic theory of the electron [105]. Both types of angular momentum are coupled by the spin-orbit interaction $\zeta \mathbf{l} \cdot \mathbf{s}$. In general, this interaction gets stronger with the atomic number Z [106]. The angular momentum of an atom is a sum of all angular momenta of its electrons. Moreover, the electron subshells consist of pairs of atomic orbitals, such that for each atomic orbital with orbital angular momentum \mathbf{l} and spin \mathbf{s} there exists another orbital with orbital angular momentum $-\mathbf{l}$ and spin $-\mathbf{s}$. As a result, the total angular momentum of a fully occupied subshell is equal to zero. That is why only the partially filled (open) subshells contribute to the total angular momentum and, consequently, to the magnetic properties of the atom.

In real atoms the orbital angular momentum interacts not only with the spin of the same electron but also with the orbital momenta of the other atomic electrons. Depending on the relative strength of these interactions different schemes of coupling of single electron angular momenta into an atomic angular momentum are possible. If the spin-orbit coupling is weaker than the electron-electron interactions, then the individual orbital \mathbf{l} and spin \mathbf{s} angular momenta are coupled into atomic orbital \mathbf{L} and spin \mathbf{S} momenta. The resultant total angular momentum \mathbf{J} of the atom is just a sum of \mathbf{L} and \mathbf{S} :

$$\mathbf{J} = \mathbf{L} + \mathbf{S} = \sum_i \mathbf{l}_i + \sum_i \mathbf{s}_i, \quad (1.3)$$

where summation is performed over the electrons of the open subshell. Such coupling scheme is called Russell–Saunders coupling or LS coupling [107] and it describes well light elements, in particular 3d transition metals. For the heavy atoms the strong spin-orbit interaction link together the spin \mathbf{s} and orbital \mathbf{l} momenta of individual electrons into a total angular momentum \mathbf{j} of a single electron. The total atomic angular momentum \mathbf{J} is then found as a sum of total angular momenta of individual electrons \mathbf{j} :

$$\mathbf{J} = \sum_i \mathbf{j}_i = \sum_i (\mathbf{l}_i + \mathbf{s}_i). \quad (1.4)$$

This approach is known as jj coupling and it is applicable, in particular, to 4f RE elements.

The magnetic properties of an atom are explained using the quantum mechanical approach, in which the result of the measurement of a physical quantity is equal to one of the eigenvalues of the corresponding operator. Moreover, according to the uncertainty principle, only the physical quantities whose quantum operators commute can be measured simultaneously. Since the angular momentum \mathbf{J} is a vector, in quantum mechanics it is described by 3 operators \hat{J}_x , \hat{J}_y and \hat{J}_z corresponding to the x , y and z components. For convenience and as it is widely accepted in the literature, we use here the dimensionless forms of the angular momentum operators. This means that the eigenvalues of these operators should be multiplied by \hbar to obtain the real observable values of the angular momenta. The commutation relations are

$$[\hat{J}_x, \hat{J}_y] = i\hat{J}_z, \quad [\hat{J}_y, \hat{J}_z] = i\hat{J}_x, \quad [\hat{J}_z, \hat{J}_x] = i\hat{J}_y. \quad (1.5)$$

As one can see, none of the two components can be measured simultaneously. However, the operator of the squared angular momentum commutes with all of the components:

$$[\hat{J}^2, \hat{J}_\alpha] = 0, \quad \alpha = x, y, z. \quad (1.6)$$

By convention, one uses \hat{J}^2 and \hat{J}_z operators to describe the angular momentum of an atom. Their quantisation happens according to the following eigenequations:

$$\hat{J}^2 \phi = J(J+1)\phi, \quad (1.7)$$

$$\hat{J}_z \phi = J_z \phi, \quad (1.8)$$

where ϕ is an eigenfunction of \hat{J}^2 and \hat{J}_z operators² while J and J_z are the quantum numbers that describe the angular momentum of an atom. J can be an integer or half-integer, at the same time J_z can take any of $2J+1$ values

$$-J, -(J-1), \dots, -1, 0, +1, \dots, +(J-1), +J.$$

These quantum numbers are sometimes called total angular momentum quantum numbers. Here we show the quantisation of the total angular momentum, but formulas similar to eqs. (1.7) and (1.8) can be obtained for orbital L and spin S angular momenta. The main difference between the three types of angular momentum is that, unlike total angular momentum and spin quantum numbers J and S , the orbital quantum number L can take only integer values.

The magnetic moments can be derived from the atomic angular momenta as follows:

$$\boldsymbol{\mu}_L = g_L \mu_B \mathbf{L}, \quad \boldsymbol{\mu}_S = g_S \mu_B \mathbf{S}, \quad \boldsymbol{\mu}_J = g_J \mu_B \mathbf{J}, \quad (1.9)$$

where g_L , g_S and g_J are called g -factors. For the orbital magnetic moment $g_L = 1$, while for the spin magnetic moment it is a good approximation to put $g_S = 2$.³ The last g -factor is also known as Landé g -factor and it can be calculated using the formula [109]

$$g_J = 1 + \frac{J(J+1) + S(S+1) - L(L+1)}{2J(J+1)}. \quad (1.10)$$

The distribution of atomic electrons over the subshells is known as electronic configuration. As an example, the electronic configuration of a neutral Dy atom is $[\text{Xe}]6s^2 4f^{10}$. The electronic configuration does not uniquely define the atomic quantum state; for instance, Dy atom in $4f^{10}$ configuration exhibits 1001 different quantum states. The latter can be grouped into terms based on their L and S quantum numbers. The energy difference between the terms is defined by electron-electron interaction, while each term is $(2L+1)(2S+1)$ degenerate. The lowest energy term can be obtained with the help of semiempirical Hund's rules [110]. The spin-orbit

²It is the same eigenfunction for both operators as they commute.

³The exact value for an electron spin is 2.00231930436256(35) [108].

Table 1.1 – The quantum numbers of the ground multiplets of Dy and Ho atoms.

Atom	Electronic configuration	L	S	J	g_J	$ \mu_J $ (eV/T)	$ \mu_J $ (μ_B)
Dy	$4f^9$	5	$\frac{5}{2}$	$\frac{15}{2}$	1.33	6.16×10^{-4}	10.65
Ho	$4f^{10}$	6	2	8	1.25	6.14×10^{-4}	10.61

coupling further splits each term into multiplets characterised by L , S and J quantum numbers. Each separate multiplet is $2J + 1$ times degenerate. This picture describes well the elements with Russell–Saunders coupling scheme. On the other hand, for the jj coupling the spin-orbit interaction can mix the states from the different terms, so that L and S are not good quantum numbers anymore. Nevertheless, J stays a good quantum number at any coupling scheme. The ground multiplets of some RE atoms studied in this work are shown in table 1.1. We note that the values of the magnetic moment mentioned in the table correspond to the absolute value of the former, obtained using the formula:

$$|\mu_J| = g_J \mu_B \sqrt{J(J+1)}. \quad (1.11)$$

The magnetic moment cannot be fully aligned with the quantisation z axis, since this would violate the uncertainty principle.

In this work we will use J and J_z quantum numbers to characterise the magnetic state of the atom. In the literature the term ‘spin’ is often used interchangeably with ‘total magnetic moment’. Technically, this is not correct as spin is an intrinsic angular momentum of a particle. Nonetheless, since these two physical quantities are closely related, we would use the terms like ‘spin lifetime’ as synonyms to magnetic moment lifetime, magnetisation lifetime or magnetic lifetime. The more detailed description of the topics discussed in this section can be found in [111, 112].

1.2 Substrate-atom interaction

An isolated atom, which does not interact with other objects, is known to exhibit paramagnetic behaviour. In other words, since there exists no preferential direction for the atomic spin, its ground multiplet is completely degenerate (fig. 1.1a). Even smallest external magnetic field applied to such atom would lift this degeneracy due to the Zeeman effect (fig. 1.1b) [113]. The energy shift of each individual quantum state can be found from the Zeeman Hamiltonian:

$$\hat{H}_{Zeeman} = -\mu_B g_J B \hat{J}_z, \quad (1.12)$$

where the magnetic field \mathbf{B} is aligned along the z axis. The state that corresponds to the biggest projection of the atomic magnetic moment onto the direction of the magnetic field (taking into account the sign) will have the lowest energy and *vice versa*. If the thermal excitations are negligible, the atom will occupy the lowest energy magnetic state, which corresponds

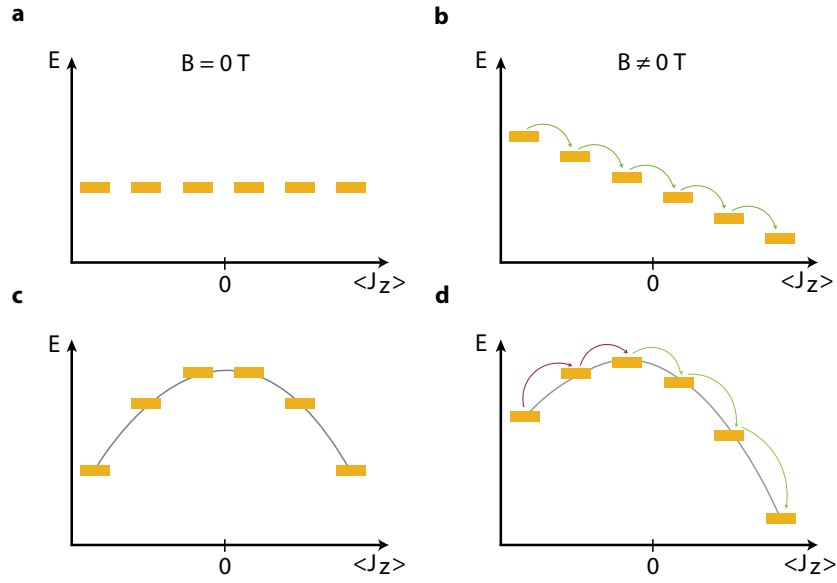


Figure 1.1 – Stabilisation of atomic magnetic moment by CF. (a) Magnetic quantum states of a free atom. (b) Zeeman splitting of the free atom magnetic states. (c) MAB introduced by the adatom-substrate interaction. (d) Magnetic stability of the surface adsorbed atoms in non-zero magnetic field. The yellow bars represent the eigenstates with given J_z , while the arrows show the path of the spin relaxation to the ground state.

to the alignment of the atomic spin along the magnetic field in classical physics. On the other hand, if there exists a magnetic easy axis, the energy diagram of the atomic magnetic states will follow a quasi-parabolic curve⁴, which is called the magnetic anisotropy barrier (MAB, fig. 1.1c). In this case the two lowest states correspond to the atomic magnetic moment aligned along the easy magnetisation axis and pointing along the two opposite directions. In case of RE adatoms such magnetic anisotropy is induced by the electrostatic interaction between the adatom and the substrate, which is known as crystal field (CF) interaction. In this section we will neglect the quantum tunneling of magnetisation (QTM), whose impact on the adatom magnetic stability will be considered in section 1.2.2. The MAB prevents the spin flipping at both zero and relatively low magnetic fields (fig. 1.1d). When the magnetic field is applied in the opposite direction with respect to the atomic magnetic moment, a metastable quantum state higher in energy than the ground state is occupied. Nevertheless, the adatom spin cannot quickly decay to the lower energy state as the relaxation path would require it to overcome the MAB. One can say that the atom is blocked in the higher energy metastable state. The relaxation occurs through a series of transitions between the atomic magnetic states. Each of these transitions needs to fulfill the energy and angular momentum conservation laws, which is only possible via substrate phonons or electrons scattering. Hence, the role of the substrate is twofold: on the one hand, it induces the MAB helping to stabilise the atoms spin; on the other hand, it also facilitates the spin relaxation. The height of the MAB is called

⁴the exact shape depends on the axial Stevens operators, see section 1.2.1

magnetic anisotropy energy (MAE). The higher is the MAE the more stable is the SAM.

The valence electrons of the 3d transition metals take part in both the formation of the adatom-substrate bond and the determination of the magnetic properties of the adatom. This makes the atomic magnetic moment of a 3d atom highly exposed to the substrate phonons and electrons prompting the spin relaxation. Contrarily, the 4f electrons responsible for the magnetism of RE atoms are screened from the substrate by the electrons of the outer 5s, 5p and 6s subshells. This explains why all currently known surface adsorbed SAMs with spin relaxation rate of the order of minutes are based on RE elements.

1.2.1 Stevens operators

There are several ways to compute the substrate electrostatic potential at the adatom position. The simplest approach consists in a representation of adatom nearest neighbours as point charges. This so-called point charge model was introduced in 1929 by Bethe [114]. Even though we make use of this model in the current work, in this section we will resort to a different approach, which better demonstrates the main involved physical phenomena. In the second method the CF is decomposed into a series of spherical harmonics

$$\hat{H}_{CF} = \sum_{k=0}^{\infty} \sum_{q=-k}^k B_k^q \hat{O}_k^q, \quad (1.13)$$

where \hat{O}_k^q are extended Stevens operators and B_k^q are Stevens coefficients [115, 116]. The latter are real numbers and are usually used as fitting parameters in attempt to find the CF that fits best the experimental data. At the same time, the Stevens operators are hermitian and they should reflect the symmetry of the CF. This fact significantly reduces the total number of the terms in eq. (1.13). In particular, the terms with odd k disappear, while q is defined by the order n of the highest rotational symmetry axis C_{nv} of the CF, such that $q = \beta n$, where $\beta = 0, 1, 2, \dots$ is a non-negative integer. The \hat{O}_0^0 term can also be omitted as it adds a constant energy shift to the whole multiplet without affecting the internal splitting of the latter. Moreover, we are interested in the effect of the Stevens operators on the orbitals that define the magnetic properties of the adatom, *i. e.*, 3d or 4f orbitals. This further simplifies the picture, since the matrix elements are equal to zero for $k > 4$ for 3d elements, and for $k > 6$ for 4f elements [117].

The Stevens operators can be separated into two groups. If $q = 0$, then the corresponding operator is a function of \hat{J}_z and the eigenfunctions of \hat{J}_z operator are also the eigenfunctions of \hat{O}_k^0 operators. Consequently, Stevens operators with $q = 0$ only lift the degeneracy of the multiplet quantum states retaining J_z as a good quantum number. These Stevens operators are usually referred to as axial terms. They define the shape of the MAB; a proper combination of axial terms ensures that there exists a well isolated doublet of ground states. On the other hand, if $q \neq 0$, the \hat{O}_k^q operator is a function of \hat{J}_z and $(\hat{J}_{\pm})^q$ operators, where \hat{J}_{\pm} are called ladder operators ($\hat{J}_{\pm} = \hat{J}_x \pm i\hat{J}_y$). The latter connects the magnetic states, whose J_z numbers differs by 1. Thereby, \hat{O}_k^q operators mix the states, whose J_z quantum numbers differs by multiples of

q . We will refer to this second type of Stevens operators as transverse terms. The strength of the induced mixing depends on the relative magnitude of the transverse term in comparison to all the other Hamiltonian terms (not only axial CF terms but also Zeeman term and *etc.*) and the difference in energy between the mixed states. In particular, for degenerate states the transverse term leads to a formation of an avoided level crossing between the quantum states on which it acts.

1.2.2 Quantum tunnelling of magnetisation

Consider a hypothetical 3d atom⁵ with $J = \frac{5}{2}$, which is located in a CF with C_{4v} symmetry (similar considerations are applicable to lanthanides). The energy diagram of its lowest magnetic states is shown in fig. 1.2. In this case, apart from the axial terms, the CF Hamiltonian has one \hat{O}_4^4 transverse term, which mixes $J_z = \frac{5}{2}$ (red triangle) with $J_z = -\frac{3}{2}$ (red circle) and $J_z = -\frac{5}{2}$ with $J_z = \frac{3}{2}$ states. First, we assume that the external magnetic field is equal to zero (fig. 1.2a). If the splitting between the two lowest doublets is high enough, we won't see the effect of the mixing on the $\langle J_z \rangle$ expectation values of the states. Then we start to introduce the external magnetic field (fig. 1.2b). The energy difference between the $J_z = \frac{5}{2}$ and $J_z = -\frac{3}{2}$ states decreases promoting the mixing between these states. The absolute value of the $\langle J_z \rangle$ expectation value becomes smaller for both mixed states. When the magnetic field reaches the so-called resonant field (fig. 1.2c), the $\langle J_z \rangle$ expectation values of both states are equal to $\frac{1}{2}(\frac{5}{2}) + \frac{1}{2}(-\frac{3}{2}) = \frac{1}{2}$, while there still remains an energy gap between them. The size of the gap is defined by the strength of the transverse CF term. If one continues to increase the magnetic

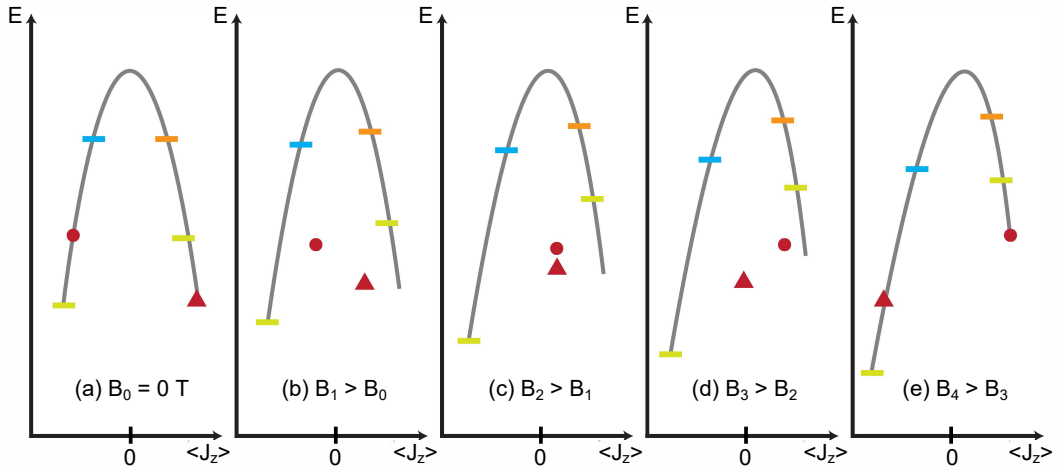


Figure 1.2 – The E - $\langle J_z \rangle$ diagrams demonstrating the QTM. The magnetic field is equal to zero in panel (a) and linearly increases towards panel (e); the colour code denotes the quantum states that are mixed by the \hat{O}_4^4 transverse term.

⁵In reality it can be Sc or Mn

field (fig. 1.2d), the lower energy state of the mixed pair will go down both in energy and $\langle J_z \rangle$, while the higher energy state will move in the opposite direction on the diagram. At some point, the former $J_z = \frac{5}{2}$ state will be located at the position on the $E-\langle J_z \rangle$ diagram where the $J_z = -\frac{3}{2}$ would have been in absence of \hat{O}_4^A term in the CF Hamiltonian, and *vice versa* (fig. 1.2e). As a result, if in the beginning the atom was in the $J_z = \frac{5}{2}$ quantum state, it will end up in the $J_z = -\frac{3}{2}$ state at the end of the process without taking a single transition between the quantum states or overcoming the MAB.

The described phenomenon is known as quantum tunnelling of magnetisation (QTM). It was first reported in 1996 for the superparamagnetic manganese clusters ($\text{Mn}_{12}\text{-ac}$) [118]. Experimentally it reveals itself as ‘steps’ in the magnetisation curves, with each ‘step’ occurring at the resonant field of a pair of mixed states. The QTM that happens between two ground states of the MAB is called a direct QTM. Otherwise, one speaks about (phonon or electron) assisted QTM. The mixing between two excited states can also lead to QTM. In this case it doesn’t affect the population of the ground states directly, but it can significantly reduce the effective height of the MAB and, hence, reduce the spin lifetime.

Kramers theorem states that every energy level of a time-reversal symmetric system with half-integer total spin is at least doubly degenerate [111, 119]. The Hamiltonian of a time-reversal symmetric system commutes with the time-reversal operator $[\hat{H}, \hat{T}] = 0$. Therefore, if ϕ is an eigenfunction of \hat{H} , then $\hat{T}\phi$ would also be its eigenfunction with the same energy. Since time reversal flips all angular momenta ($J_z \rightarrow -J_z$), the systems with the integer J can have non-degenerate levels (with $J_z = 0$), but not the half-integer J systems. For the SAMs this theorem can be applied only at $B = 0\text{ T}$ as external magnetic field breaks the time-reversal symmetry. In other words, adatoms with half-integer J don’t exhibit the QTM exactly at zero magnetic field.

1.3 Conclusion

The ideal CF for a single-atom magnet would exhibit a perfectly axial $C_{\infty v}$ symmetry with a dominating negative \hat{O}_2^0 term. The axuality of the CF will fully suppress the QTM, while the strong \hat{O}_2^0 term will promote the proper shape of the MAB (a parabola with branches pointing downwards). In the point charge model this would correspond to a single negative point charge located just below the adatom, or two negative point charges located one above and one below the adatom [75, 76, 80]. The real crystals never consist of one or two atoms, so the actual symmetry of the adatom adsorption sites is always lower. Moreover, one needs to protect the adatom from the substrate electron and phonon scattering as they facilitate the magnetic moment reversal over the MAB.

Recently, there has been an active search for the systems exhibiting such perfectly axial CF. Examples include dysprosocenium [67] and dysprosium metallocene [70] molecules as well as Ho [83] and Dy [46] single atoms deposited on MgO(100) surface. Furthermore, this is one of the main objectives of the current project.

2 Methods

2.1 X-ray absorption spectroscopy

XAS is a widely used experimental method of characterisation of the local geometry and electronic structure of matter. It consists in the energy resolved measurement of the absorption of the X-ray light by the sample. Like all the other core hole spectroscopies, XAS exhibits the elemental selectivity. The XAS spectra feature the sharp rises in absorption at the specific photon energies, which are called X-ray absorption edges. These edges correspond to the energies required to excite an atomic core electron into unoccupied energy levels. Depending on the type of a sample, the latter can be a valence shell (for single atoms), a lowest unoccupied molecular orbital (for molecules), a valence band or Fermi level (for solids). These transitions are distinctive characteristics of a chemical element. Thereby, one obtains an elemental and shell specificity in XAS by tuning the photon energy to a corresponding X-ray edge.

Since we are interested in the magnetic properties of RE single atoms, the spectra of $M_{4,5}$

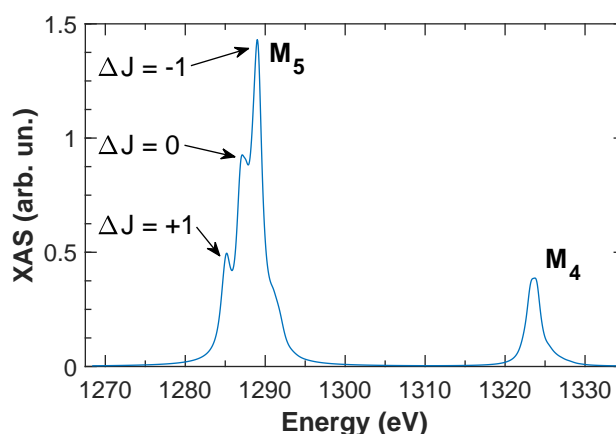


Figure 2.1 – A typical XAS spectrum of Dy^{3+} calculated for $B = 0$ T and $T = 3$ K by neglecting the CF interaction.

edges, which correspond to the $3d \rightarrow 4f$ transitions, were measured in our experiments. A typical XAS spectrum of a Dy^{3+} ion is shown in fig. 2.1. It consists of two distinct groups of lines located around 1289 eV and 1323 eV, which correspond to M_5 and M_4 edges, respectively. In the first approximation that neglects the electron-electron interaction they can be attributed to the spin-orbit split $3d_{5/2}$ and $3d_{3/2}$ core hole states. Furthermore, the XAS transitions are subject to dipole selection rules $\Delta J = 0, \pm 1$ and $\Delta J_z = 0, \pm 1$.¹ Dy M_5 edge exhibits a clear multiplet structure comprising 3 pronounced peaks, which can be assigned to $\Delta J = +1$, $\Delta J = 0$ and $\Delta J = -1$ transitions [120, 121]. The information about the atomic electronic structure, including the subshell occupation and the quantum ground state, can be extracted from the XAS spectrum with the help of the multiplet simulations (see section 2.7).

2.2 X-ray magnetic circular dichroism

Each peak of the Dy M_5 spectrum includes transitions of 3 types: $\Delta J_z = +1$, $\Delta J_z = 0$ and $\Delta J_z = -1$, which can be studied independently by means of polarised X-ray photons. Right(left)-hand circularly polarised light induces $\Delta J_z = +1(-1)$ transitions, while $\Delta J_z = 0$ transitions are accessible via X-ray photons linearly polarised along the z axis. At zero magnetic field the number of $\Delta J_z = +1$ and $\Delta J_z = -1$ transitions is equal and they occur with the same probability. The external magnetic field introduces the imbalance in the population of the states participating in these transitions, which reveals itself in the difference between the absorption of right-hand and left-hand polarised light (fig. 2.2). This effect is called XMCD and it provides the information on the magnetism at the subshell level.

The atomic orbital and spin magnetic moments can be deduced from the XMCD spectrum. To this end, one uses the so-called sum rules [18, 19], which are slightly different for 3d and

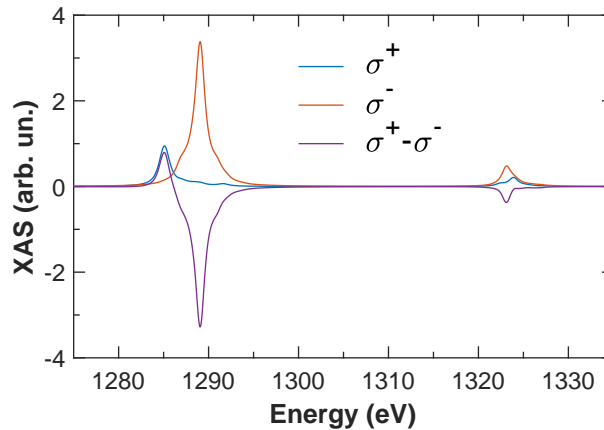


Figure 2.2 – Dy^{3+} XAS spectra of right-hand (σ^+) and left-hand (σ^-) circularly polarised light together with the XMCD spectrum ($\sigma^+ - \sigma^-$) calculated for $B = 5.5$ T and $T = 3$ K by neglecting the CF interaction.

¹Though, the $J = 0 \rightarrow J = 0$ transitions are strictly forbidden.

4f elements. Here, we provide only the 4f versions; the sum rules for the 3d elements can be found elsewhere [18, 19, 122]. If the photon flux is parallel to the z axis, then

$$\langle \hat{L}_z \rangle = -3(14 - n) \frac{X_{4,5}}{I}, \quad (2.1)$$

$$2 \langle \hat{S}_z \rangle + 6 \langle \hat{T}_z \rangle = -\frac{3}{2}(14 - n) \frac{5X_5 - 3X_{4,5}}{I}, \quad (2.2)$$

where n is the number of electrons in the 4f subshell in the initial state, T_z is the spin quadrupole angular momentum, $X_{4,5}$ and X_5 are the integrals of the XMCD signals over both M_4 and M_5 , and only M_5 edges, respectively. The normalisation factor I is the integral over both edges of the absorption intensity of unpolarised X-ray light, which can be decomposed into three components:

$$I = I_x + I_y + I_z, \quad (2.3)$$

where I_x , I_y and I_z are X-ray absorption of linearly polarised along the x , y and z axes light. Taking into account that photon beam is parallel to the z axis and using the $I_x + I_y = I_+ + I_-$ relation, where I_+ and I_- are X-ray absorption of right-hand and left-hand circularly polarised light, we obtain

$$I = I_+ + I_- + I_z. \quad (2.4)$$

Since I_z component is usually inaccessible in the experiments, one commonly makes an assumption of the isotropic adsorption, which gives us

$$I = \frac{3}{2}(I_+ + I_-) = \frac{3}{2}(I_x + I_y) = \frac{3}{2}I'. \quad (2.5)$$

Combining eqs. (2.1), (2.2) and (2.5), we get

$$\langle \hat{L}_z \rangle = -2(14 - n) \frac{X_{4,5}}{I'}, \quad (2.6)$$

$$2 \langle \hat{S}_z \rangle + 6 \langle \hat{T}_z \rangle = -(14 - n) \frac{5X_5 - 3X_{4,5}}{I'}. \quad (2.7)$$

In the last two equations the normalisation factor I' is measured only with two types of light polarisations: either right-hand and left-hand circular polarisations, or two linear polarisations perpendicular to each other. Exactly these equations were used to estimate the orbital and spin magnetic moments of the adatoms in this work. Even though the L_z angular momentum can be obtained from the eq. (2.6), one needs further information to separate the S_z momentum from the T_z momentum in the eq. (2.7). As the CF interaction is much weaker than the spin-orbit coupling for the RE atoms, we suppose that the $\frac{T_z}{S_z}$ ratio does not change upon surface adsorption [123]. Hence, with the help of the $\frac{T_z^{gas}}{S_z^{gas}}$ ratio calculated for the gas-phase atoms we can compute the S_z magnetic moment. For example, for the Dy^{3+} $\frac{T_z^{gas}}{S_z^{gas}} = -0.06$ [123, 124] and

we obtain

$$2 \langle \hat{S}_z \rangle + 6 \langle \hat{T}_z \rangle = 2 \langle \hat{S}_z \rangle + 6 \frac{\langle T_z^{gas} \rangle}{\langle S_z^{gas} \rangle} \langle \hat{S}_z \rangle = 1.64 \langle \hat{S}_z \rangle. \quad (2.8)$$

The strong spin-orbit coupling in RE elements keeps the orbital and spin magnetic moments collinear to each other, thereby, the intensity of the XMCD signal is proportional not only to the orbital moment μ_{Lz} but also to the total magnetic moment of the atom μ_{Jz} . This fact is exploited in the magnetic hysteresis loop and spin relaxation time measurements (see section 2.6). We note that the intensity of the XMCD signal is proportional to the projection of the sample magnetisation onto the direction of the X-ray beam.

2.3 X-ray magnetic linear dichroism

XMLD is a technique, which is experimentally very similar to XMCD. The main distinction is that in XMLD one measures the difference in absorption of the linearly polarised light, instead of circularly polarised one. It is widely used to study the antiferromagnetic samples [125, 126], in which the ordered magnetic spins induce the anisotropy of the valence electron charge density via the spin-orbit coupling. Linearly polarised X-ray photons then are used to determine the direction of the induced charge anisotropy. The measurements show the highest contrast when the first polarisation is parallel to the magnetic axis, while the second one is perpendicular.

In this work, we utilised the XMLD technique to probe the anisotropy of the 4f electron charge distribution. The latter directly influences the magnetic properties of RE atoms. Intuitively, one can claim that prolate charge distribution along the surface normal should lead to an in-plane magnetic anisotropy, while oblate to an out-of-plane anisotropy [127]. Thus, XMLD helps us to determine the magnetic anisotropy of the adatoms [128]. Moreover, XMLD provides us with additional experimental data, which allows to increase the accuracy of the CF fitting via multiplet simulations (see section 2.7).

2.4 EPFL/PSI X-Treme beamline

The X-rays were discovered by Röntgen in 1895 by means of a device, which we would call today an X-ray tube [129]. To this day, this is the simplest method of X-ray generation extensively used for medical purposes. In the X-ray tubes the special targets are bombarded with highly energetic electrons, which kick out the core electrons of the target material. This process creates the core holes, which are filled with the valence electrons of the target. A by-product of this relaxation is an X-ray photon. Nonetheless, X-ray tubes exhibit a number of drawbacks: they produce an uncollimated and relatively low photon flux. Modern scientific experiments with X-ray are generally performed at the synchrotrons, where the accelerated relativistic electrons are utilised to produce the X-rays [130]. Such method allows to obtain a well collimated beam, which is several orders of magnitude brighter than an X-ray tube

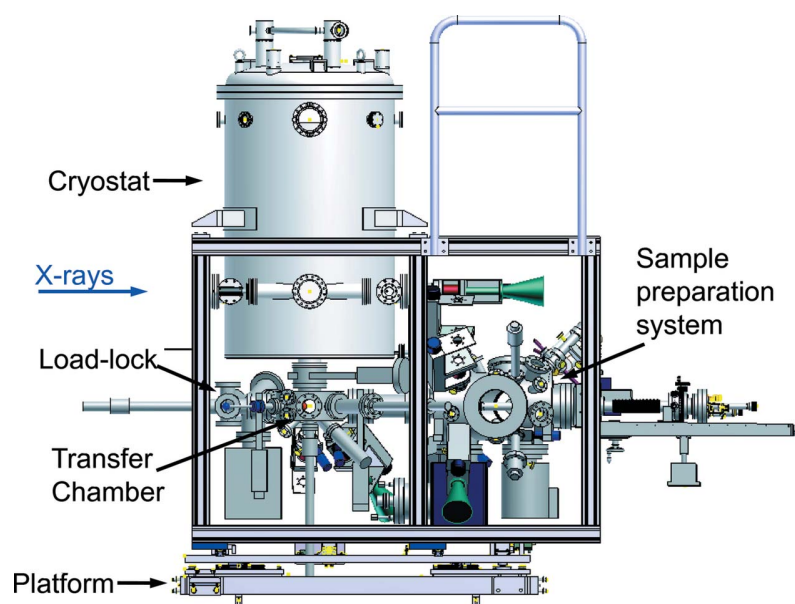


Figure 2.3 – A schematic representation of the EPFL/PSI X-Treme beamline end station taken from ref. [131].

produced beam.

All the experiments presented in this work were performed at the EPFL/PSI X-Treme beamline at Swiss Light Source (PSI, Villigen, Switzerland) [131]. The beamline end station consists of a cryostat, preparation chamber, transfer chamber and a load-lock (fig. 2.3). All the X-ray measurements are performed in the cryostat with a base temperature of 2.5 K and a base pressure in the low 10^{-11} mbar. Moreover, the cryostat is equipped with a 7 T superconducting magnet. All these specifications are mandatory to perform the experiments with SAMs. The preparation chamber is used for the surface preparation and characterisation. It includes a low energy electron diffraction/Auger spectroscopy setup, a variable temperature STM/AFM and multiple ports for various evaporators, which are used for the thin film growths. The transfer chamber connects together all the chambers of the station, while the samples are introduced into the system through the load-lock.

2.5 Total electron yield

There exist three X-ray absorption detection modes: transmission, total fluorescence yield (TFY) and total electron yield (TEY). The simplest approach consists in detection of the number of X-ray photons penetrating through the sample. The higher is the number of such photons, the lower is the X-ray absorption. Quantitatively, the XAS intensity is described by a linear absorption coefficient μ . A reduction of the X-ray beam intensity in the absorption

medium is given by the Beer–Lambert law:

$$I(z) = I_0 e^{-\mu z}, \quad (2.9)$$

where I_0 is the beam intensity at $z = 0$. The absorption coefficient is measured in reciprocal units of length, while the inverse value to the absorption coefficient is known as the attenuation length. In our experiments the RE adatoms were deposited on a millimetre-scale thick substrates completely non-transparent for the X-rays in our energy range of interest (1000 eV to 1500 eV), making impossible any measurements in transmission mode.

The X-ray photons are adsorbed by the core electrons of the sample, which leads to a formation of a highly energetic core-hole state. The excited atom relaxes on a subfemtosecond time scale by filling the core hole with one of the valence electrons. The energy lost by this electron can be transmitted to a photon (fluorescence effect) or another electron (Auger effect). The ratio of probabilities between the two relaxation processes can be deemed constant on an energy scale of a single XAS spectrum (≈ 100 eV), thereby, both fluorescence photons and Auger electrons can be used to evaluate the XAS intensity. In the first case the detection mode is called TFY, in the second TEY.

If the Auger electron was created within the mean free electron path (≈ 5 nm) from the sample surface, it has a high probability of leaving the sample, thus, charging it. Furthermore, if the sample is grounded, this will cause a difference of the potentials between the sample and the ground. The resultant current, which is called TEY current, is proportional to the number of electrons leaving the sample and, hence, to the X-ray absorption signal. This current basically keeps the sample neutral by providing it the electrons, which it loses due to the photoelectric effect. All our X-ray absorption signals were obtained via the TEY current. Moreover, highly energetic Auger electrons undergo a series of scattering events generating a cascade of secondary electrons, which significantly increases the total number of photoelectrons. Therefore, in TEY mode the detected XAS signal is amplified by means of processes similar to those taking place in an avalanche photodiode. This detection scheme exhibits the required surface sensitivity to study as dilute samples as 0.005 ML, where 1 ML correspond to one RE adatom per substrate unit cell.

2.6 Experimental geometry and data analysis

The experiments, when not otherwise specified, were performed at $\theta = 0^\circ$ and $\theta = 60^\circ$ angles between the photon flux and surface normal, which we will label as normal incidence and grazing incidence, respectively. The magnetic field was kept parallel to the X-ray beam all the time. A typical set of data includes XMCD spectra measured at normal and grazing incidences at high enough magnetic field (usually 5.5 T) to ensure the sample saturation, and XMLD spectra recorded at grazing incidence at high (5.5 T) and low (0.1 T) magnetic fields. For all types of spectra the absorption of the substrates at the energies of the RE $M_{4,5}$ edges was recorded before the adatom deposition. These background measurements were then

subtracted from the RE adsorption spectra. Right-hand (σ^+) and left-hand (σ^-) circularly polarised light was recorded during the XMCD measurements. XAS spectrum corresponds to $\sigma^+ + \sigma^-$, while XMCD to $\sigma^+ - \sigma^-$. For the XMLD measurements we used horizontally (σ^h) and vertically (σ^v) polarised X-rays, where σ^v is parallel to the substrate surface, while σ^h is perpendicular to σ^v and inclined by 30° from the surface normal. The XMLD signal was obtained as $\sigma^v - \sigma^h$. In this configuration XMLD is sensitive to the out-of-plane anisotropy of the 4f charge distribution. All the spectra were normalised to the integral over the XAS M_5 adsorption edge to compensate the variance in the RE coverage between different samples.

Magnetisation curves were measured as the dependence of the XMCD signal on the external magnetic field. The photon energy at which to measure the loop was chosen as the maximum of the XMCD absolute value at the RE M_5 edge to maximise the signal-to-noise ratio. The opening of the hysteresis curve indicates long spin relaxation time and depends on the ramp rate. To maximise the magnetisation loop openings we swept the magnetic field at the highest possible rate of 2 T/min. Furthermore, the X-ray photons are known to induce demagnetisation of SAMs and surface adsorbed SMMs [66, 77, 81, 83]. To minimise this effect we used the defocused beam with the spot size of approximately 2 mm^2 . This allowed us to significantly reduce the photon flux while maintaining high signal-to-noise ratio by increasing the total number of adatoms participating in the measurement. Unless the contrary is explicitly stated, all the magnetisation curves in this work are normalised to the saturation magnetisation.

The spin relaxation curves show the rate at which the magnetisation of the adatom ensemble decays from saturation to the equilibrium value at the specific magnetic field. They were obtained as follows: first, the sample is magnetised to the saturation at high enough magnetic field; next, the magnetic field is swept to the value at which the relaxation curve will be recorded at the maximum possible ramp rate of 2 T/min; the relaxation curve is then measured as the time dependence of the XMCD signal. The same X-ray energies were used for the relaxation curve and magnetisation curve measurements.

2.7 Multiplet calculations

For some samples information about the magnetic properties was obtained with the help of the multiplet calculations. The latter provide a way to simulate XAS, XMCD and XMLD spectra as well as the equilibrium magnetisation curves. In this approach all the possible quantum states of the initial ($3d^{10}4f^n$) and final ($3d^94f^{n+1}$) electronic configurations are calculated through the diagonalisation of the following Hamiltonian [132–134]:

$$\hat{H} = \sum_i \frac{\hat{p}_i^2}{2m_e} + \sum_i \frac{-Ze^2}{r_i} + \sum_{ij} \frac{e^2}{r_{ij}} + \sum_i \zeta(r_i) \hbar^2 \hat{\mathbf{l}}_i \cdot \hat{\mathbf{s}}_i + \hat{H}_{CF} + \sum_i \mu_B \mathbf{B}(\hat{\mathbf{l}}_i + 2\hat{\mathbf{s}}_i), \quad (2.10)$$

where the summation takes place over all the atomic electrons. The first term represents the electron kinetic energy, the second electron-nucleus interaction and the third electron-electron Coulomb repulsion. Spin-orbit interaction is described by the fourth term, while the

last two terms correspond to CF and Zeeman interactions, respectively. At the low temperature (≈ 3 K) only few lowest initial states are populated.

According to the Fermi's golden rule, the transition probabilities are defined by the squares of the transition operator matrix elements. In dipole approximation the transition operator is $\boldsymbol{\epsilon} \cdot \mathbf{r}$, where $\boldsymbol{\epsilon}$ is the photon polarisation vector. Taking into account the core hole broadening Γ_i , which is introduced through a Lorentzian function, we obtain a formula for the calculation of the X-ray absorption spectrum:

$$I(\omega) \propto \sum |\langle \phi_f | \boldsymbol{\epsilon} \cdot \mathbf{r} | \phi_i \rangle|^2 \frac{\Gamma_i / \pi}{(\hbar\omega + E_i - E_f)^2 + \Gamma_i^2}, \quad (2.11)$$

where E_i (E_f) and ϕ_i (ϕ_f) denote the energy and the wavefunction of the initial (final) state. The summation occurs over the all possible combinations of the initial and final states.

In section 1.2.1 we employed the Steven's operators to explicitly write down the CF Hamiltonian (eq. (1.13)). Although this approach is rather instructive, it introduces a lot of fitting parameters (Steven's coefficients), which can result in an overparametrisation. For instance, a system consisting of RE atoms adsorbed at two different C_{4v} and C_{2v} symmetric adsorption sites would require up to 14 fitting coefficients ($B_2^0, B_4^0, B_4^4, B_6^0$ and B_6^4 for the C_{4v} adsorption site, and $B_2^0, B_2^2, B_4^0, B_4^2, B_4^4, B_6^0, B_6^2, B_6^4$ and B_6^6 for the C_{2v} site). Even though some of the higher order parameters are likely equal to zero, we chose to use a model based on point charges for the calculation of the CF interaction, which is more practical, especially for the systems with multiple adsorption sites.

The multiplet simulations presented in this thesis were performed with the multiX code [104]. Unlike the nonrelativistic Schrödinger equation approach presented above, this code is based on the solution of the atomic central field relativistic Dirac equation in the density functional theory formalism (for details see ref. [104]). The investigated chemical element and its electronic configuration are defined in the input file. Only integer subshell occupations are allowed. In the simulation the CF is manually defined by the user within the point charge model, while the Coulomb electron-electron and spin-orbit interactions can be scaled separately for core and valence subshells with respect to their Hartree-Fock values. As an output the code provides the simulated XAS, XMCD or XMLD spectra calculated with eq. (2.11) for the experimental conditions specified in the input file. The core hole broadening Γ can be controlled by the user.

3 Magnetic stability of Dy and Ho single atoms on BaO

In this chapter the following manuscript currently in preparation for publication is reproduced:

- **Title:** Magnetic Stability of Dy and Ho Single Atoms on Alkaline Earth Oxides
- **Authors:** Boris Sorokin, Marina Pivetta, Valerio Bellini, Darius Merk, Sébastien Reynaud, Alessandro Barla, Harald Brune and Stefano Rusponi
- **Author contributions:** S.Rusponi and H.B. conceived the experiment. B.S., S.Rusponi, M.P., A.B., D.M. and S.Reynaud carried out the measurements. V.B. performed the DFT calculations. B.S. and S.Rusponi analysed the data and carried out the multiplet simulations. S.Rusponi calculated the phonon induced transitions. B.S., S.Rusponi and V.B. wrote the manuscript. H.B. and S.Rusponi supervised the project. All authors discussed the results and contributed to the manuscript.

Therein, we study the magnetic properties of Dy and Ho single atoms deposited on BaO thin films grown on Pt(100) single crystals. A long magnetic lifetime, manifested by an opening of the magnetisation curve, is demonstrated for Dy adatoms. The density functional theory (DFT) calculations revealed two possible adsorption sites for RE atoms: top-O and bridge. Furthermore, we propose a new approach for the CF point charges evaluation, which allows us to better incorporate the RE-substrate bond covalency. With the help of multiplet simulations we unravel the contributions of different adsorption species to the observed experimental spectra. The current results are compared to similar studies of Dy and Ho single atoms on MgO thin films. The longer magnetic lifetimes of the RE atoms on MgO than BaO are rationalised via adatom lowest energy level diagrams and physical properties of the supporting substrates.

3.1 Main text

3.1.1 Introduction

RE single atoms have been shown to be promising candidates for quantum technology applications [46, 49, 61, 63, 64, 67, 69–71, 73–77, 79–83, 85, 87, 135]. Being placed on a crystal surface or in a coordination complex, they are subject to a CF that lifts the degeneracy of the ground J-multiplet. Careful design of the CF can result in an energy level scheme suitable for atomic-size magnetic memories [46, 49, 67, 69, 70, 77, 81, 83, 87] or quantum computation devices [73, 135]. The spin lifetime serves as a main indicator of whether a lanthanide atom can be used as a bit of information. A CF level splitting that induces a sufficiently high MAB can lead to long magnetisation lifetimes by hampering thermally activated magnetic moment relaxation via the top of the barrier [76]. Other spin relaxation mechanisms are the direct or the assisted QTM, which originate from level mixing induced by the finite CF symmetry. Thereby, a perfectly axial CF is necessary to produce a stable atomic bit, since it both generates a high anisotropy barrier and suppresses QTM via retaining the pure character of the quantum states.

Among the whole lanthanide series, Dy and Ho exhibit the highest magnetic moments and recently have been successfully employed as SAMs [46, 49, 81–83, 85, 87] and SIMs [67, 69, 70, 79]. All these systems follow the same strategy: long relaxation times are obtained via uni-axial ligand field environments provided by one or two preponderant covalent bonds to the RE, while the other ligands provide a marginal contribution. A family of compounds corresponding to this strategy are the diatomic LnO complexes (where Ln is a RE atom), which have been predicted to provide long relaxation time for both divalent ($4f^n$) and trivalent ($4f^{n-1}$) electronic configurations ($n = 10$ for Dy, $n = 11$ for Ho) [75, 76, 80]. So far, the closest experimental realisation of such LnO unit is represented by a Ln atom adsorbed at the O-top site of MgO thin films grown on Ag(100) [46, 49, 82, 83, 85, 87]. Indeed, for this adsorption site, the trivalent configuration of both Ho and Dy show remarkable magnetic stability.

Like MgO, other alkaline earth oxides provide a similar CF environment with the different lattice constants and alkaline earth metal electronegativities as potential parameters to tune the axial *vs* transversal components of the CF. In this article we report on the electronic and magnetic properties of Dy and Ho single atoms adsorbed on BaO thin films grown on Pt(100) single crystals. The samples were studied with XAS, XMCD, XMLD and DFT. Both species exhibit only trivalent electronic configuration. Dy atoms show magnetic hysteresis, while paramagnetism is observed for Ho adatoms. DFT calculations revealed a higher degree of RE-O bond covalency for BaO as compared to MgO.

3.2 Results and discussion

We performed XAS, XMCD and XMLD measurements at the $M_{4,5}$ edges ($3d \rightarrow 4f$ transitions) of Dy (fig. 3.1) and Ho (fig. 3.2) atoms adsorbed on thin films of BaO grown on Pt(100) at

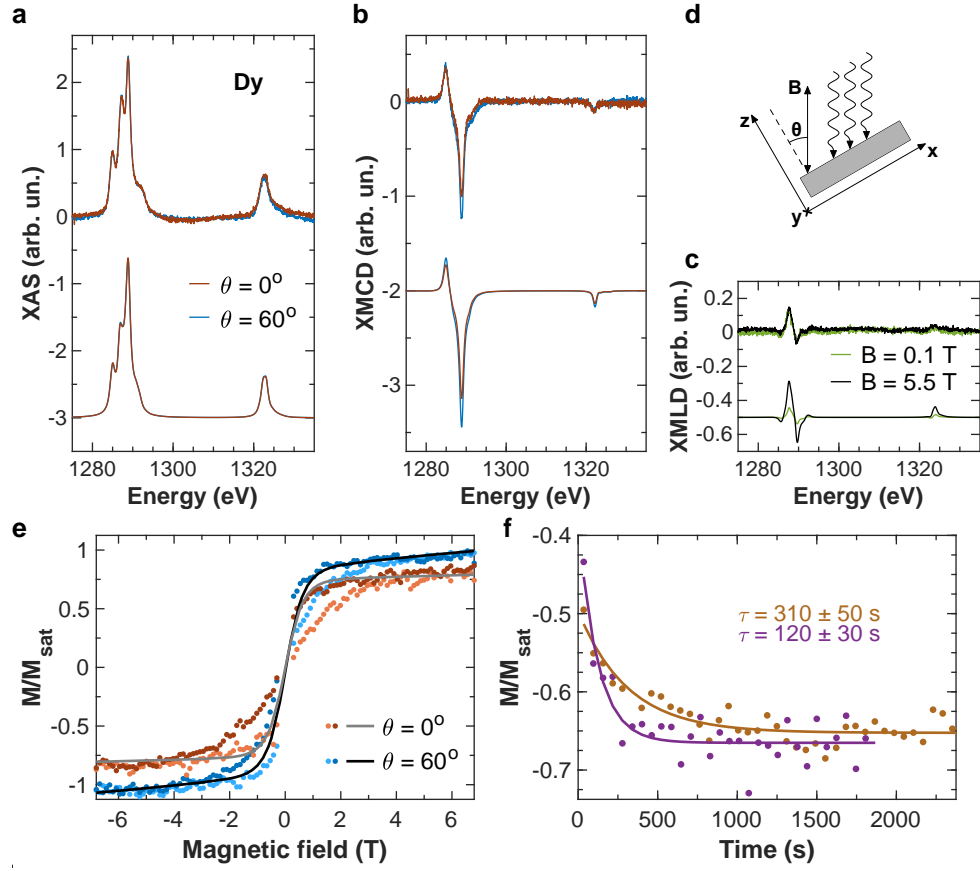


Figure 3.1 – Experimental and simulated (a) XAS, (b) XMCD and (c) XMLD spectra of 0.019 ML Dy on 5.5 ML thick BaO film grown on Pt(100). XAS and XMCD spectra were measured at normal (red lines) and grazing (blue lines) incidences ($B = 5.5$ T); XMLD spectra were recorded at grazing incidence at $B = 0.1$ T (green lines) and $B = 5.5$ T (black lines). The simulated data have been offset to lower values for clarity. (d) Schematic representation of the experimental geometry. (e) Magnetisation curves measured by acquiring the XMCD signal at 1288.8 eV as a function of magnetic field ($\phi = 5.4 \times 10^{-3}$ photon/(nm²s), $|\dot{B}| = 33$ mT/s). Dots denote the experimental values: red - normal incidence, blue - grazing incidence; the simulated equilibrium curves are shown with solid lines. All experimental data were acquired at $T \approx 3$ K. (f) Time evolution of the XMCD intensity at 1288.8 eV measured at $B = -0.5$ T after saturation of the sample magnetisation at $B = 4$ T. Dots - experimental data, lines - single exponential fits. Purple - $\phi = 9.2 \times 10^{-4}$ photon/(nm²s), Ocher - $\phi = 1.4 \times 10^{-3}$ photon/(nm²s). $T \approx 3$ K, $\theta = 60^\circ$.

the EPFL/PSI X-Treme beamline of the Swiss Light Source [131] to determine the 4f orbital occupation and magnetic properties. We focused on BaO thin films with a thicknesses ranging from 5 to 8 ML; no significant difference in the adatom magnetic properties has been observed in this thickness range. The spectra have been acquired at $\theta = 0^\circ$ (normal incidence) and $\theta = 60^\circ$ (grazing incidence) angles between the photon flux, kept parallel to the magnetic field, and the surface normal. For simplicity of discussion, we introduce a Cartesian coordinate

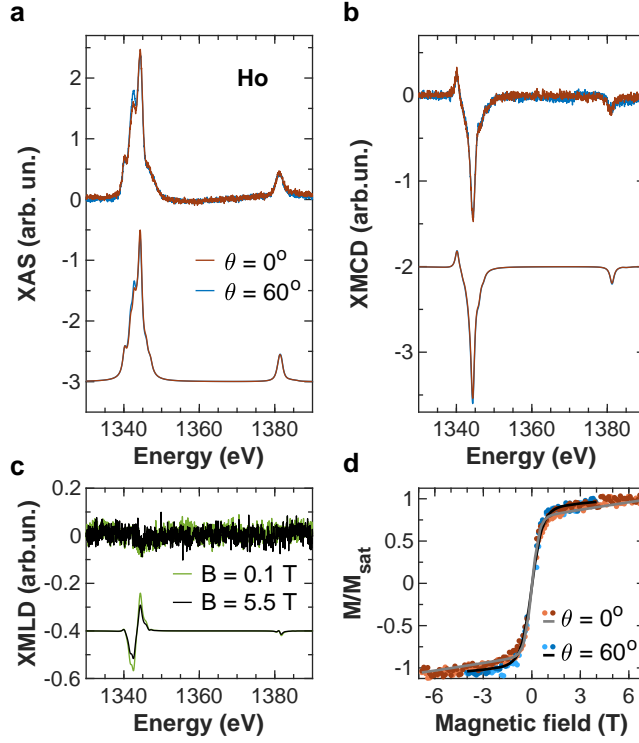


Figure 3.2 – Experimental and simulated (a) XAS, (b) XMCD and (c) XMLD spectra of 0.009 ML Ho on 5.9 ML thick BaO film grown on Pt(100) ($B = 5.5$ T, $T \approx 3$ K). The simulated data have been offset to lower values for clarity. (d) Magnetisation curves measured by acquiring the XMCD signal at 1344 eV as a function of magnetic field ($\phi = 4.7 \times 10^{-3}$ photon/(nm² s), $|\dot{B}| = 33$ mT/s, $T \approx 3$ K). The colour code is identical to the fig. 3.1.

system with the z axis directed along the surface normal and the y axis perpendicular to the magnetic field (fig. 3.1d). From the XAS and XMCD spectra we infer a $4f^9$ electronic configuration of Dy adatoms [136], up to a BaO film thickness of 8 ML. For comparison, Dy on MgO/Ag(100) exhibits 2 distinct configurations: $4f^9$ and $4f^{10}$ [82]. The relative abundance of the two electronic configurations depends on the MgO film thickness: the $4f^9$ configuration dominates for MgO thicknesses smaller than 5 ML, while the $4f^{10}$ configuration becomes predominant for substrate thicknesses greater than approximately 6 ML. The XMCD spectrum of Dy atoms on BaO acquired at $B = 5.5$ T demonstrates a slightly stronger intensity at grazing than at normal incidence, hinting at in-plane magnetic anisotropy of the adatom ensemble. Furthermore, we acquired magnetisation hysteresis curves by measuring the XMCD signal at the peak of the M_5 edge (1288.8 eV) while sweeping the magnetic field between ± 6.8 T at the rate of 33 mT/s (fig. 3.1e). Both normal and grazing magnetisation loops show a narrow opening, which extends up to about 3 T. Such hysteretic behaviour is a sign of a long spin lifetime in SAMs [81–83]. To quantitatively estimate the spin relaxation dynamics we fully magnetised our sample at $B = 4$ T and $\theta = 60^\circ$, then swept the magnetic field down to $B = -0.5$ T at the maximum possible rate of 33 mT/s and measured the subsequent decay of the XMCD signal (fig. 3.1f). The observed relaxation time of about 300 s is shorter than the record long

Table 3.1 – Total energies (in eV) of Dy and Ho on BaO and MgO substrates (the values are relative to the ground state adsorption site) for the top-O and bridge adsorption sites. The occupation of the 4f orbital (integrated over spheres of radius of 2.4 a.u. centered on the nuclei positions) of the RE adatoms is reported as well.

System	Energy (eV)		n (e^-)	
	Top-O	Bridge	Top-O	Bridge
Dy/BaO	0	0.07	9.56	8.96
Ho/BaO	0	0.03	9.93	9.93
Dy/MgO	0	0.44	9.75	9.77
Ho/MgO	0	0.65	9.93	9.92

spin lifetimes (>1000 s) reported for Ho atoms on MgO/Ag(100) [83] under similar photon flux conditions, in agreement with the tight opening of the corresponding magnetisation curve.

Similarly to Dy, also Ho on BaO is found in the trivalent electronic configuration ($4f^{10}$), as can be deduced from the XAS and XMCD spectra [136]. The corresponding XMCD signal reveals no preferential direction for the magnetic moment of the adatom ensemble. The magnetisation curve of Ho adatoms measured in normal incidence seems to show a tiny opening, however comparable with our statistical accuracy; no signs of hysteresis has been observed for the grazing incidence magnetization loop (fig. 3.2d).

In order to assist the interpretation of the experimental data, we have analysed by DFT calculations the adsorption site energetics for Dy and Ho adatoms on a BaO substrate, as reported in table 3.1 (see section 3.3.3 for details about DFT calculations). For comparison, the results for the MgO substrate are given as well. The direct adsorption of RE on the alkaline earth metal sites, Ba and Mg, is highly unfavorable and it is not discussed further. While on MgO the top-O site is clearly preferred, in agreement with previous calculations [137], on BaO the bridge site is found to be very close in energy to the top-O site, for both Dy and Ho. This suggests that for BaO, in contrast to the MgO case, the population of the bridge site should be comparable to that of the top-O one. The comparison of the Dy 4f occupation on the two substrates reveals a tendency towards a trivalent configuration on BaO, particularly evident for the bridge site, in agreement with our experimental observations. This contrasts with the divalent configuration we find on MgO, in agreement with a previous study of Dy adatoms on thick MgO films [82]. For Ho, DFT finds an occupation close to $4f^{10}$ for both substrates, again in line with the experimental evidence [83].

Since BaO and MgO have very different lattice constants, it is instructive to look at the charge density distribution to unravel the interplay between the ionic arrangement and the electronic properties, and to find clues about the origin of the different magnetic anisotropy shown by the RE adatoms on BaO as compared to MgO. In fig. 3.3 we present isosurface 2D plots of the majority spin charge densities for Dy adatom on BaO [panels (a) and (b)] and MgO [panels

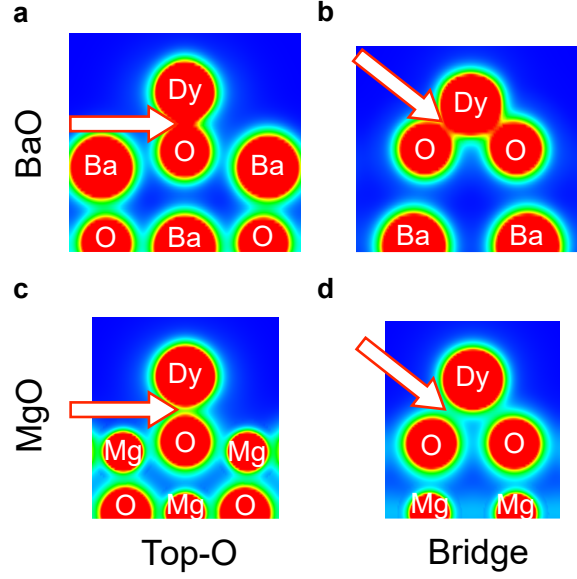


Figure 3.3 – Charge density isosurfaces (isovalue = $0.05 e^-/\text{\AA}^3$) for Dy adatoms on top-O and bridge sites on BaO and MgO.

(c) and (d)] for top-O and bridge sites, with cross-sections at the Dy-O-Ba(Mg) and O-Dy-O planes, respectively. The size of each panel is proportional to the lattice constants of BaO and MgO. The adsorption heights of Dy at the top-O sites are similar for the two substrates, while at bridge sites the adatom relaxes sensibly more towards the surface on BaO, due to the larger O-O distances, as compared to MgO (see appendix A.1). For both sites, it is evident that the electronic density in the mid-point of the Dy-O bonds (indicated by the arrows) is higher on BaO than on MgO, suggesting a higher degree of covalency of such bonds for the former surface. Bader analysis finds that O atoms attain a smaller net charge on BaO ($-1.36 e^-$) as compared to MgO ($-1.69 e^-$), the latter being closer to the nominal charge of $-2 e^-$ of a perfectly ionic compound (more details on Bader charges and atomic coordinates are given in the appendix A.1).

With this in mind, we performed multiplet calculations using the multiX code [104], which uses effective point charges to compute the CF. We considered both top-O and bridge adsorption sites. In the experiment, the samples have been oriented according to the sketch in fig. 3.4a (see section 3.3.1 for details on sample orientation). In order to reproduce the experimental conditions, two bridge adsorption sites, having different alignment with respect to the magnetic field orientation, were included in the multiplet calculations. The br-xz adsorption site has the two nearest O atoms lying along the x axis, while the br-yz one along the y axis (fig. 3.4a).

The choice of positions and values of the effective point charges is a recurring problem in such calculations, especially when covalent bonds are involved, due to the necessity to model the continuous spatial distribution of real charges with a few punctual ones [138, 139].

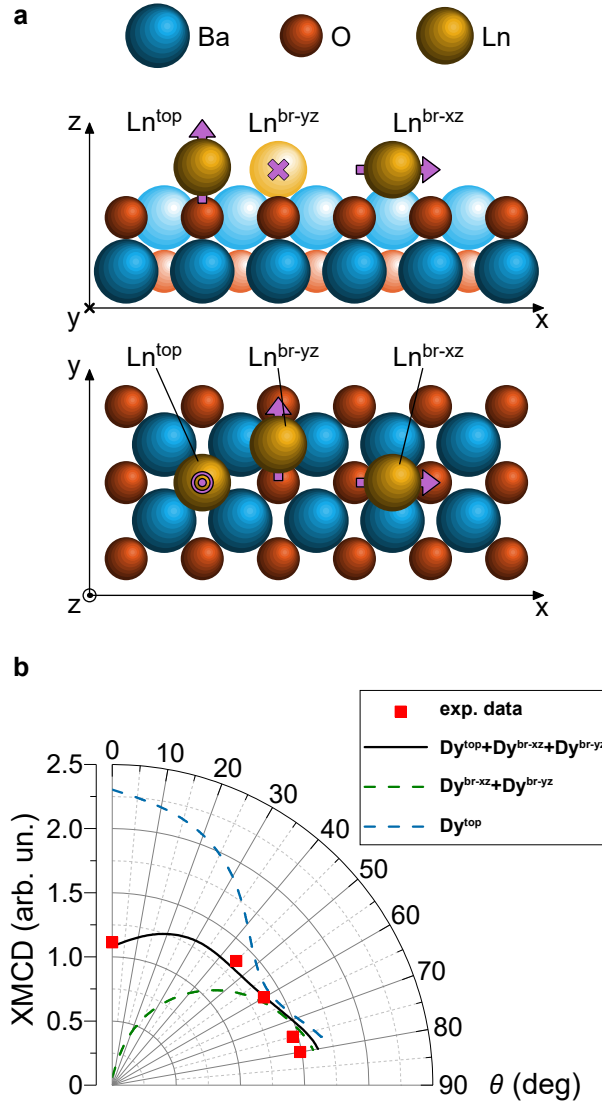


Figure 3.4 – (a) RE single atoms at top-O, br-xz and br-yz adsorption sites. Two projections (xz and xy) are shown for clarity; violet arrows indicate the easy magnetisation directions for different species as discussed in the text. Atoms depicted with lighter colours belong to the row that is shifted by half a lattice constant along the y axis. (b) Experimental and simulated XMCD angular dependence of 0.014 ML of Dy on 6.2 ML thick BaO ($B = 4$ T, $T \approx 3$ K). Red squares denote the experimental data; blue and green dashed lines simulation of Dy^{top} and Dy^{br} species, respectively; black solid line simulated data averaged over all species. The arbitrary units are identical to those in fig. 3.1a-c.

Several models have been proposed in the last decades; however, a general strategy is still missing [114, 140–143]. In the Dy/MgO case, the rather intuitive approach consisting in replacing the ionic charges calculated with DFT by point charges of same intensity and located at the atom positions works quite well, with only a 0.8 scaling factor required to match the experimental results [46, 82]. However, the same approach failed to reproduce our data on

BaO. We tested several strategies with the requirement that the same methodology must be applicable to both adsorption sites. Guided by the consideration that only O atoms bind to RE adatoms while Ba charges are not affected by RE deposition, we found as a suitable solution the following procedure: (1) Ba charges and positions as from DFT; (2) based on electronegativity arguments, the O-RE distances are scaled by a factor $\epsilon_O/(\epsilon_{Dy} + \epsilon_O)$ where $\epsilon_{O,Dy}$ are the Pauling electronegativities of the corresponding elements [140]; (3) the effective O charge is used as fitting parameter and kept identical for both top and bridge species.

The top-O adsorption site results in a pronounced out-of-plane magnetisation easy axis, while bridge sites produce a very strong in-plane anisotropy along the the O-RE-O axes. Since both solutions are at odds with our experimental findings, we considered a mixture of top and bridge adsorption sites, in agreement with the DFT analysis presented above. We assumed an equal population of the two bridge sites, while the relative occupancy of the top-O site served as a second fitting parameter. According to DFT, showing almost identical adsorption energies for both Ho and Dy, the ratio of bridge to top-O species was kept identical for both elements. In addition, we assumed the same effective O charge for both lanthanides, since their electronegativities differ by less than 1% ($\epsilon_{Dy} = 1.22$, $\epsilon_{Ho} = 1.23$).

The simulated XAS, XMCD, XMLD spectra and equilibrium magnetisation curves are shown in fig. 3.1a-c, fig. 3.1e (Dy) and fig. 3.2 (Ho). An excellent agreement is found between measured and calculated spectra with abundances of 40% for top-O, and of 30% each for br-xz and br-yz.

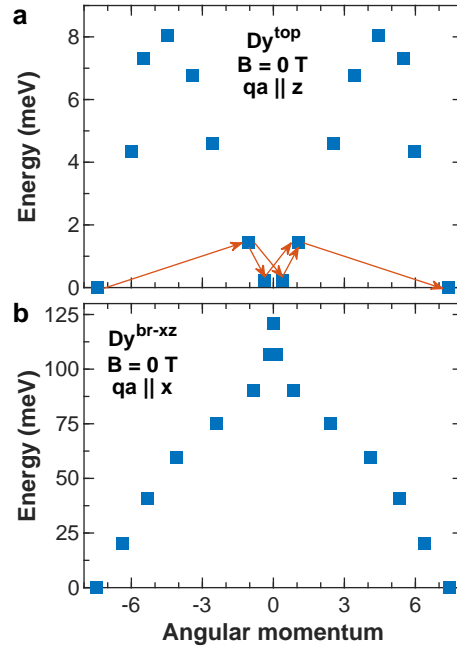


Figure 3.5 – Energy diagrams of the lowest energy multiplets for (a) Dy^{top} and (b) Dy^{br-xz} atoms. The quantisation axes (qa) are aligned with magnetisation easy axes (z - for top species, x - for bridge-xz species).

The relative abundances of RE atoms at top-O and bridges sites suggest that atoms landing on the highly unfavorable top-Ba sites diffuse with approximately the same probability to either of those sites. Indeed, from the statistics of impact sites (there are two bridge sites, one top-O and one top-Ba site per BaO unit cell) and in the case of equal diffusion probability from top-Ba to top-O and bridge, we infer relative abundances for these sites of 37.5% and 62.5%, respectively. The slightly higher population returned by the fitting procedure for top-O site with respect to the one expected from a pure statistical approach is in agreement with the trend found in the adsorption site energetics by DFT (table 3.1). To further corroborate the estimated values for the adsorption site populations, we measured the angular dependence of the Dy XMCD signal at 1288.8 eV. The plot confirms that a single adsorption site is clearly inadequate to describe the experimental trend, while an excellent agreement between experimental and simulated data is found with the estimated relative abundances (fig. 3.4b).

The magnetic anisotropies and spin lifetimes observed for the two RE elements can be understood with the help of the energy level schemes of the lowest multiplet calculated for the different adsorption sites. The Dy top-O (Dy^{top}) has a small out-of-plane anisotropy with a total barrier height of about 8 meV and a ground state with mainly a $|J_z\rangle = \pm \frac{15}{2}$ character (fig. 3.5a). The wavefunction compositions, in terms of $|J_z\rangle$ eigenstates, for the ground doublet are:

$$\begin{aligned} |\pm\psi_{\text{Dy}^{\text{top}}}\rangle : & 0.993 |\pm 15/2\rangle \\ & 0.104 |\mp 1/2\rangle \\ & 0.053 |\pm 7/2\rangle \\ & 0.004 |\mp 9/2\rangle \end{aligned} \quad (3.1)$$

with the C_{4v} symmetric CF mixing states whose J_z differs by multiples of 4. Conversely, the C_{2v} symmetric bridge sites have a strong in-plane anisotropy with the maximum projection of J along the x axis ($|J_x\rangle$) for $\text{Dy}^{\text{br-xz}}$ and along the y axis ($|J_y\rangle$) for $\text{Dy}^{\text{br-yz}}$ adatoms (fig. 3.5b). The wavefunctions in terms of $|J_x\rangle$ ($|J_y\rangle$) along the x (y) axis for the ground doublets are:

$$\begin{aligned} |\pm\psi_{\text{Dy}^{\text{br}}}\rangle : & 0.99050 |\pm 15/2\rangle \\ & 0.13576 |\pm 11/2\rangle \\ & 0.02165 |\pm 7/2\rangle \\ & 0.00360 |\pm 3/2\rangle \\ & 0.00063 |\mp 1/2\rangle \\ & 0.00012 |\mp 5/2\rangle \\ & 0.00003 |\mp 9/2\rangle \\ & 0.00001 |\mp 13/2\rangle. \end{aligned} \quad (3.2)$$

The ground doublet is well isolated from the first excited doublet ($\Delta E = 20.4$ meV) and the total barrier amounts to 121 meV. As a consequence of these strong in-plane easy axes, we find only a negligible projection of the Dy^{br} spins onto the surface normal direction even in high out-of-plane magnetic fields (see the green dashed line in fig. 3.4b). The experimentally observed slight in-plane anisotropy for the atom ensemble results then from the sum of the contributions of the different adsorption sites. At normal incidence the XMCD signal originates only from Dy^{top} adatoms, as the magnetic moments of both Dy^{br} species remain oriented in-plane in our experimental conditions. On the contrary, at grazing incidence the observed signal is a mixture of Dy^{top} and $\text{Dy}^{\text{br-xz}}$ contributions. The $\text{Dy}^{\text{br-yz}}$ atoms are inaccessible to XMCD in our experimental geometry because their magnetic moment maintains a perpendicular orientation with respect to the external magnetic field. They reveal themselves only in the XAS and XMLD spectra.

From the two energy schemes we also deduce a longer spin lifetime for Dy^{br} as compared to Dy^{top} . The Dy^{br} energy level diagram closely resembles the schemes reported for DyO complexes [75, 76, 80]. In all these cases, given the almost pure states, spin reversal takes place via the top of the barrier. The opposite situation is seen for Dy^{top} . By calculating the phonon induced transitions between the energy levels (see Methods) we find the shortcuts for spin reversal shown in fig. 3.5a with red arrows. Spin reversal involves the first two pairs of excited states. From the ground state, spin-phonon scattering with $\Delta J_z = \pm 2$ pushes the spin to the second excited doublet at 1.4 meV, having mainly a $|\mp \frac{3}{2}\rangle$ character, from where it decays on the first excited doublet at 0.2 meV and $|\mp \frac{1}{2}\rangle$ character. The spin is then again pushed to the second excited state from where it can finally relax to the ground state on the other side of the barrier.

Experimentally we observe very similar magnetisation hysteresis at normal and grazing incidences where only Dy^{top} or both Dy^{top} and Dy^{br} contribute, respectively. This reveals that the observed spin relaxation rates do not represent intrinsic values, as well exemplified in fig. 3.1f where τ decreases by increasing the photon flux. The $\tau = 310 \pm 50$ s reported for the lowest flux has then to be considered as a lower limit for the intrinsic spin lifetime.

The $\text{Dy}^{\text{top}}/\text{BaO}$ level scheme exhibits an avoided level crossing between $|\pm \frac{15}{2}\rangle$ and $|\mp \frac{1}{2}\rangle$ states at $B = \pm 350$ mT. This QTM channel reduces the effective magnetic anisotropy barrier and is expected to accelerate the magnetisation reversal in the $B = \pm 0.5$ T range. Even though the low magnetic fields are not experimentally easily accessible, we note that the most rapid decrease of the sample magnetisation takes place exactly in this range of fields (fig. 3.1e).

The corresponding energy schemes for Ho top-O (Ho^{top}) and Ho bridge (Ho^{br}) atoms are shown in fig. 3.6 (blue upward-pointing triangles). The Ho $4f^{10}$ electronic configuration leads to a $J = 8$ non-Kramers lowest energy multiplet. The ground state doublets of both Ho^{top} and Ho^{br} species are strongly mixed by the CF. To better resolve the nature of the split doublets, we calculated the energy diagrams at 100 mT, since at this magnetic field the Zeeman energy overcomes the CF mixing terms at least at the bottom of the barrier (red downward-pointing

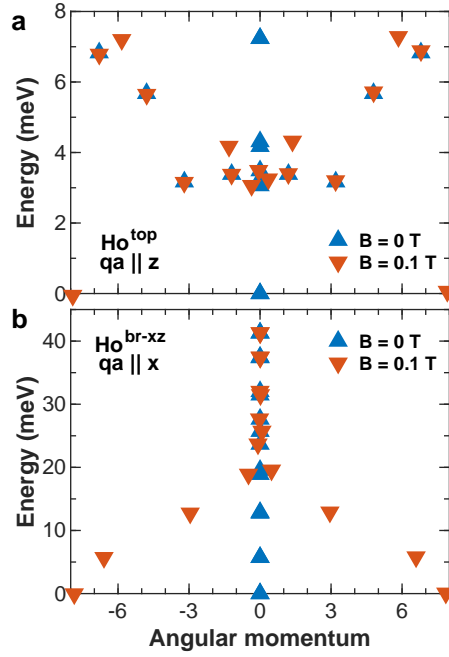


Figure 3.6 – Energy diagrams of lowest energy multiplets for (a) Ho^{top} and (b) $\text{Ho}^{\text{br-xz}}$ atoms. The quantisation axes (q_a) are aligned with magnetisation easy axes (z - for top species, x - for bridge- xz species). Blue upward-pointing triangles denote the simulation at $B = 0 \text{ T}$, while red downward-pointing triangles at $B = 100 \text{ mT}$.

triangles in fig. 3.6). Thereby, we find for Ho the same behaviour as for Dy: out-of-plane easy axis for Ho^{top} , and in-plane easy axes along the O-RE-O directions for Ho^{br} adatoms. For Ho^{top} species we deduce a similar height and shape of the magnetic anisotropy barrier as for Dy^{top} adatoms. Nonetheless, the C_{4v} CF causes a strong mixing of Ho^{top} quantum states, facilitating QTM. The Ho^{br} energy scheme has also a similar shape to the Dy^{br} one. However, the overall height of the Ho^{br} barrier is three times lower than that of the Dy^{br} , and the mixing of the states by the CF is even stronger than in the Ho^{top} case. Therefore, all Ho species (Ho^{top} , $\text{Ho}^{\text{br-xz}}$ and $\text{Ho}^{\text{br-yz}}$) contribute to both normal and grazing experimental spectra (see section 3.3.2). In addition, we attribute the fast spin relaxation of Ho species, revealed by the absence of openings in the magnetisation curves, to the QTM prompted by strong level mixing.

As a general trend, we find a reduced magnetic stability, for both Dy and Ho, on BaO as compared to MgO, consequence of smaller energy barriers and higher level mixing. On the BaO surface, the most stable species is the Dy^{br} characterised by almost pure states and a total barrier of about 120 meV. All other species show mixed states and total barriers of a few tens of meV or less. On the contrary, on MgO all species have almost pure states and barrier heights exceeding 100 meV. The situation is worsened by the fact that BaO (Debye temperature of about 340 K [144]) is softer than MgO (Debye temperature of about 760 K [145, 146]), with BaO phonon DOS showing a broad maximum around 10 meV [144] while MgO phonon DOS remains very low up to more than 30 meV. Consequently, spin relaxation via spin-phonon

scattering is much more efficient on BaO. This effect is well exemplified by the different photon limited τ values observed, at given photon flux, for Dy on BaO as compared to previously reported values of the order of 2000 s for Ho adatoms on MgO/Ag(100) [83, 84]. This difference can be rationalised by noting that the X-ray absorption coefficient for BaO at the Dy M_5 edge is more than 2 times higher as compared to the value for MgO at the Ho M_5 edge ($3.3 \mu\text{m}^{-1}$ against $1.5 \mu\text{m}^{-1}$) [147]. For a given photon flux, the X-ray absorption coefficient is a good measure of the number of secondary electrons generated by the radiation. These secondary electrons limit the spin lifetime by scattering either directly with the adatom spin or with substrate phonons, which, in turn, scatter with the adatom spin. The efficiency of the latter relaxation mechanism is higher for softer substrates.

3.2.1 Conclusion

To sum up, Dy and Ho single atoms have been shown to adsorb on top-O and bridge sites of BaO/Pt(100) thin films. The Dy^{top} species exhibit long spin lifetime of the order of 300 s. Comparison with the Dy single atoms adsorbed on the top-O site of MgO/Ag(100) thin films revealed the importance of the Dy-O bond character for the adatom magnetic stability. In case of Dy^{top} /BaO, a higher degree of covalency of this bond degrades the axially of the CF at the adatom position reducing the magnetic anisotropy barrier. Furthermore, the MgO substrate was found to be more suitable for SAMs from the point of view of phonon and secondary electron assisted sample demagnetisation. At the same time, Dy^{top} single atoms exhibit a higher stability of the magnetic moment than their Ho counterparts on both BaO and MgO substrates.

3.2.2 Methods

The Pt(100) single crystal was prepared *in situ* by repeated cycles of Ar^+ sputtering and annealing at a temperature $T \approx 1170$ K. The BaO thin films were grown by evaporation of Ba (Mateck, 99.3% purity) from an effusion cell in an O_2 partial pressure of 10^{-6} mbar onto a substrate held at 670 K, with subsequent annealing for 30 minutes at 920 K in UHV ($p \approx 10^{-8}$ mbar). The stoichiometry, crystallinity and thickness of BaO films were characterised by low energy electron diffraction (LEED), XAS and X-ray linear dichroism (XLD, see section 3.3.1). To calibrate the dependence of the Ba M_5 edge XAS intensity on the BaO film thickness, we grew at the EPFL a reference sample with a BaO coverage of 0.7 ML as determined by scanning tunneling microscopy. Dy and Ho adatoms were deposited from high purity rods (99.9%) using an e-beam evaporator at $T < 5$ K and $p \approx 3 \times 10^{-11}$ mbar.

The X-ray absorption experiments were performed at the EPFL/PSI X-Treme beamline at the Swiss Light Source [131]. The measurements were carried out in the TEY mode at a temperature $T \approx 3$ K. The XAS, XMCD and XMLD correspond to $(\sigma^+ + \sigma^-)$, $(\sigma^+ - \sigma^-)$ and $(\sigma^v - \sigma^h)$, respectively, where σ^+, σ^- are the absorption of right-handed and left-handed circularly polarised X-rays, and σ^h, σ^v the absorption of horizontal (x axis) and vertical (y axis)

linearly polarised X-rays. The background signals were recorded at RE $M_{4,5}$ edges on clean substrates prior to adatom deposition and subsequently subtracted from the corresponding lanthanides' spectra. To compensate for the possible differences in the adatom coverages all of the spectra were normalised to the integral over RE M_5 adsorption edge.

DFT calculations have been carried out by employing the augmented-plane wave+local orbital method as implemented in the Wien2K code [148]. The generalised-gradient approximation (GGA) [149] of the exchange and correlation functional has been considered for the structural characterisation, while the electronic structure analysis has been obtained by using an on-site version of the hybrid B3LYP functional [150]. In our experience this functional is better suited (as compared to the more standard +U methods) to achieve the correct 4f occupation in the ground state, which is a key issue in elements such as Dy that can attain different valencies. Moreover it bypasses the need of the U parameter's choice, that involves always some arbitrariness, particularly when results for different RE species are compared. Calculations have been done without spin-orbit interaction (details on the simulation cell can be found in section 3.3.3).

The multiX code was used to perform the multiplet simulations [104]. The Slater-Condon integrals were scaled to 75%, core electrons spin-orbit coupling to 97%, valence electrons spin-orbit coupling to 85%. We used a core-hole lifetime lorentzian broadening of 0.6 eV; the point charges can be found in appendix A.2.

In order to individuate the principal paths for spin reversal, we have adopted a master equation approach to calculate the transitions among the energy levels [151, 152]. The transitions are evaluated within a spin-lattice relaxation model, including direct and Orbach-type scattering mechanisms, based on Fermi's golden rule and the Hamiltonian proposed by Fort *et al.* [153], which involves transitions with $\Delta J_z = 0, \pm 1, \pm 2$. A Debye model was used for the low-energy phonon spectrum.

3.3 Supporting information

3.3.1 BaO thin film characterisation

LEED image of Pt(100) surface is shown in fig. 3.7a. The image exhibits a typical Pt(100)-hex surface reconstruction (also called Pt(100)-(5×20)) [154]. LEED image of 6 ML thick BaO(100) film grown on Pt(100) is given in fig. 3.7b. Pt single crystal orientation was not changed during the BaO growth procedure, therefore, these LEED images confirm epitaxiality of our growth procedure. The horizontal direction in fig. 3.7b is approximately parallel to x axis (see section 3.2 for the definition of the Cartesian coordinate system). Thus, we inferred an angle of about 5° between BaO [100] crystallographic direction and x axis. No influence of this misalignment on the results of the multiplet simulations was found. Hence, we neglected the mismatch and considered [100] direction parallel to x axis in our data analysis.

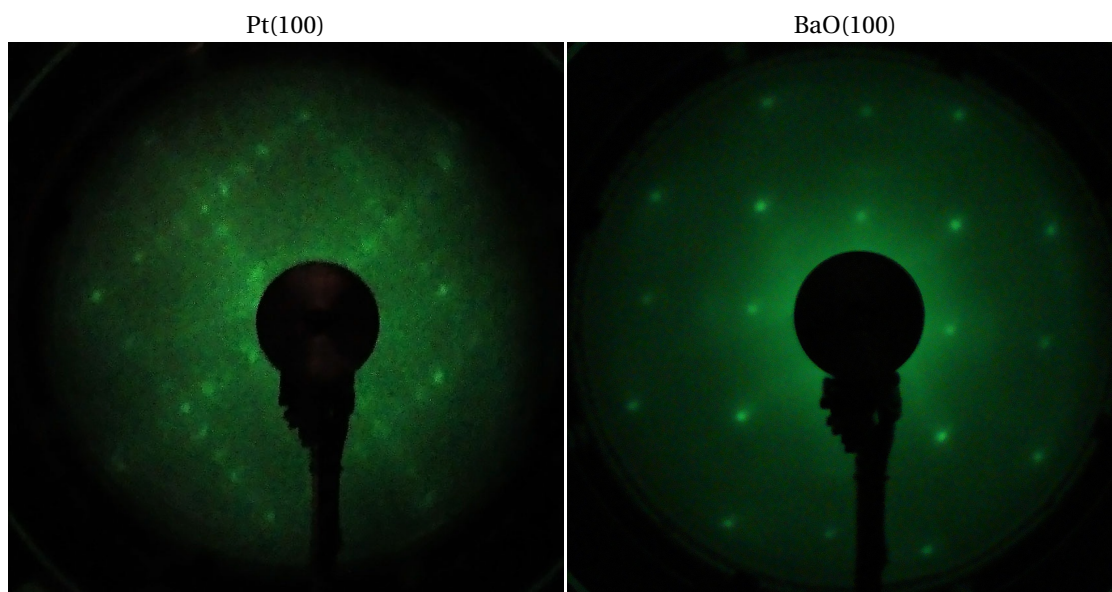


Figure 3.7 – LEED images of (a) Pt(100) single crystal and (b) BaO(100) thin film (6 ML).

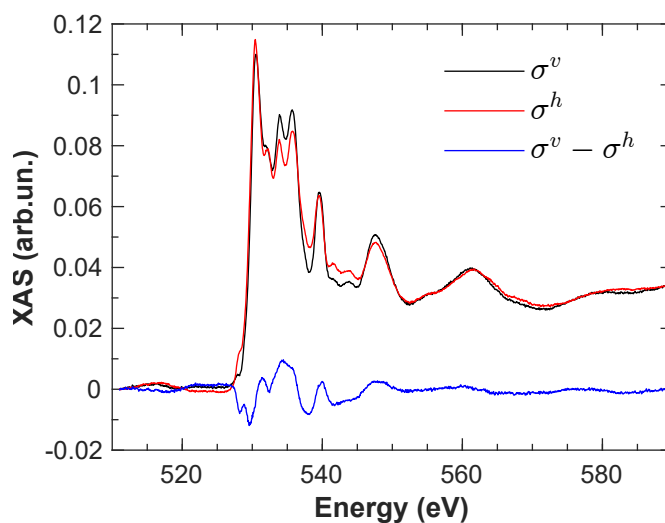


Figure 3.8 – O K-edge adsorption of vertically (σ^v , black line) and horizontally (σ^h , red line) polarised X-rays together with XLD ($\sigma^v - \sigma^h$, blue line).

XAS and XLD spectra were used to characterise the BaO thin films. A typical O K-edge XAS of vertically and horizontally polarised X-rays together with the corresponding XLD spectrum are shown in fig. 3.8. Well defined multiplet structure as well as linear dichroism signal indicate that O is found in a well oriented crystalline structure.

3.3.2 Additional results of multiplet simulations

To find out the bridge species spin orientations in our experimental conditions we calculated the energy diagrams of the lowest multiplets, while keeping both quantisation axis and magnetic field aligned with either normal or grazing direction (see the main text for the experimental geometry). In all cases only the ground doublets are populated at 3 K. Bridge-xz and bridge-yz adsorption sites exhibit identical energy schemes at normal orientation of the

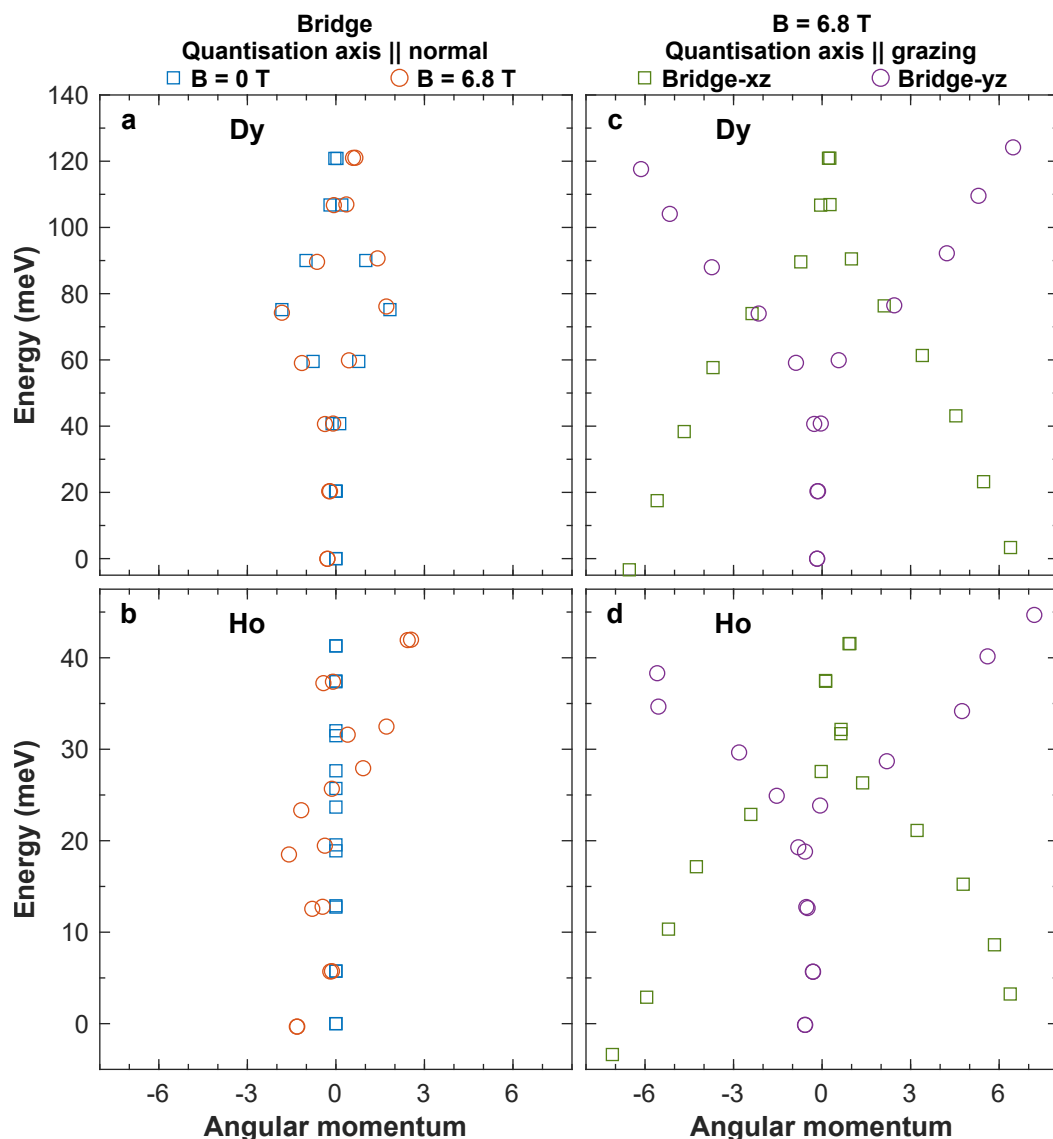


Figure 3.9 – Energy diagrams of the bridge species lowest J-multiplets. (a) Dy^{br} and (b) Ho^{br} energy diagrams calculated at $B = 0$ T (blue squares) and $B = 6.8$ T (red circles) with quantisation axis (qa) along the normal direction. (c) Dy and (d) Ho energy diagrams calculated for bridge-xz (green squares) and bridge-yz (violet circles) at $B = 6.8$ T and with quantisation axis aligned along the grazing direction.

quantisation axis, as expected from the symmetry considerations. The corresponding energy diagrams are shown in fig. 3.9a (Dy^{br}) and fig. 3.9b (Ho^{br}). From these schemes we see, that Dy^{br} species exhibit only a tiny expectation value of the magnetic moment along the normal direction even at $B = 6.8$ T. The exact value is $0.386 \mu_B$, which is only 4% of the same value for Dy^{top} adatoms ($9.906 \mu_B$). On the other hand, Ho^{br} species show a 4 times higher spin expectation value at the same experimental conditions ($1.643 \mu_B$), which corresponds to non-negligible 17% of the equivalent Ho^{top} value ($9.859 \mu_B$). Therefore, we can neglect the out-of-plane component of Dy^{br} spins, but not of Ho^{br} ones.

When the quantisation axis is parallel to the grazing direction, the energy diagrams of bridge-xz and bridge-yz species are not the same anymore (fig. 3.9c and fig. 3.9d). In this case we find a negligible magnetic moment of Dy^{br-yz} adatoms ($0.228 \mu_B$), which is only 3% of the Dy^{br-xz} spin ($8.635 \mu_B$). The latter is the highest magnetic moment among all three adsorption sites at grazing incidence. The same trend is found for Ho^{br-xz} and Ho^{br-yz} species. Nevertheless, Ho^{br-yz} magnetic moment ($0.719 \mu_B$) correspond to 8% of Ho^{br-xz} one ($8.806 \mu_B$). Hence, only Dy^{br-yz} spins can be neglected at grazing incidence.

3.3.3 DFT calculations: simulation cell

Since the electronic configuration of Dy and Ho does not change increasing the thickness (up to 5 ML) of BaO on Pt(100), the BaO(100) substrate has been simulated by a slab composed of 6 ML (2.5 BaO lattice constant) thick slab, without considering the presence of the Pt substrate, as depicted in fig. 3.10. Vacuum space is added in the direction normal to the surface in order to avoid spurious interaction between the slabs replica. In order to describe the case of isolated RE adatoms, a 2x2 in-plane periodicity has been assumed. Similarly, for MgO substrate, we have removed the Ag substrate, and considered the same simulation cells as for BaO. The experimental BaO and MgO lattice constants of $a_{BaO}^{latt} = 5.54 \text{ \AA}$ and $a_{MgO}^{latt} = 4.21 \text{ \AA}$ have been used. The coordinates of the RE adatoms and of the upper two substrate layer atoms have been relaxed until residual forces were less than 1 meV/a.u.

3.4 Conclusion and outlook

The dissimilarity in the Dy-O bond character can be explained by the difference in the lattice constant of BaO (3.97 \AA) and MgO (3.01 \AA). The shorter lattice constant of MgO facilitates the Mg-O interaction, preserves the ionic character of the MgO crystal and does not allow O to attract more electrons from Dy. On the contrary, longer distance between Ba and O atoms allows Dy to closer approach O and form a covalent bond. Moreover, a smaller charge transfer from Ba to O also explains why Dy tends to transfer more charge to O on BaO. Following this logic, one obtains that a metal oxide with a rock salt crystal structure and short lattice constant is needed to improve the magnetic stability of a SAM. The only alkaline-earth metal that is smaller than Mg is Be. However, BeO crystallises into a wurtzite structure. To our knowledge, no cubic BeO thin films have been grown so far. Nonetheless, the wurtzite crystal structure

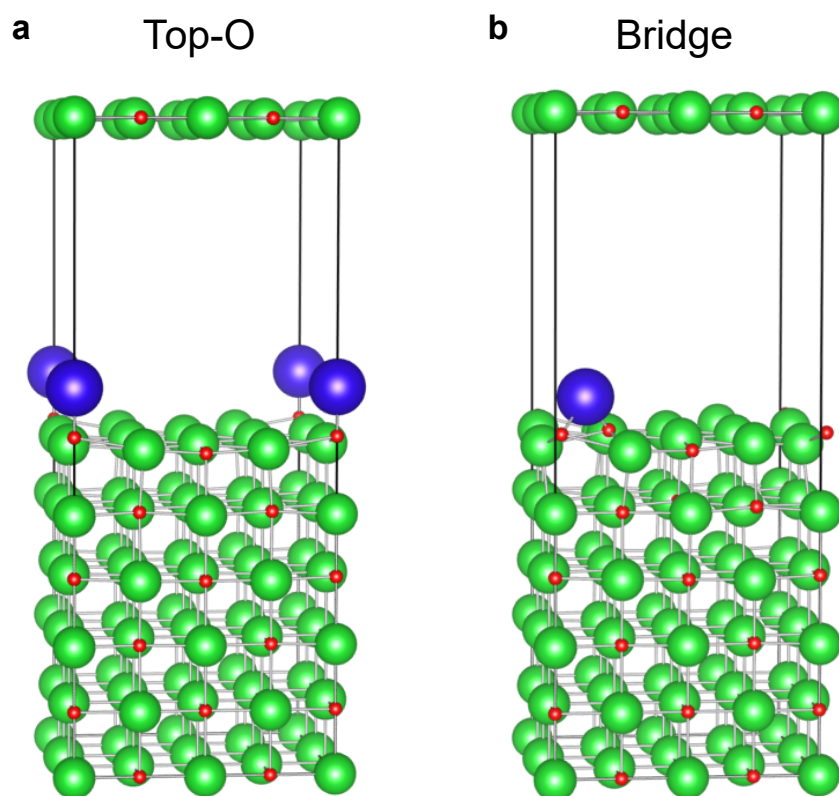


Figure 3.10 – Simulation cells for RE adatoms on BaO (or MgO) surface, for the (a) top-O and (b) bridge adsorption sites. O, Ba(Mg) and Dy(Ho) atoms are depicted with small red, medium green and large blue spheres, respectively.

can also provide a CF suitable for SAMs as will be demonstrated in the next chapter.

4 Electric field control of single atom spin lifetime

Electrical conductivity of a semiconductor can be modulated by an external electric field. This phenomenon is known as field effect. Electric field cannot penetrate into metals, since they possess a high number of free electrons that rearrange themselves in a way as to fully compensate the externally applied field. On the other hand, the concentration of such free charges is significantly reduced in semiconductors. Therefore, an external electric field partially penetrates into a semiconductor on a scale defined by Debye screening length, which is a function of charge carrier density and temperature. As a result, an accumulation or depletion surface layer is formed depending on the orientation of the external field. This charge carrier density modulation is the origin of the observed change in the electrical resistivity. At least three contacts are required to perform a field effect experiment: a source, a drain and a gate. The first two are used to measure the conductivity along the sample surface, while the gate is utilised to apply the external electric field perpendicular to this surface. Field effect plays a crucial role in contemporary electronics. It underlies the working principle of a metal-oxide-semiconductor field-effect transistor, which serves as a building block for modern computers.

In this work, however, we made use of a field effect to electrically control the magnetic stability of surface-adsorbed single atoms, whose spin lifetime strongly depends on the substrate charge carrier density. To this end, we deposited Dy single atoms on thin films of zinc oxide (ZnO). The latter is a well-known wide-band-gap semiconductor ($E_g = 3.3$ eV [155]), which is thoroughly studied due to its potential applications in optoelectronic, piezoelectronic, spintronic and photovoltaic devices [156, 157]. In addition, being doped with transition-metal ions it exhibits ferromagnetic behaviour [158]. Zinc oxide has a wurtzite crystal structure, which can be described as a combination of two hexagonal close-packed lattices shifted one relative to the other along the c axis (fig. 4.1). The first lattice consists only of Zn atoms, the second entirely of O ones. Moreover, its non-centrosymmetric $6mm$ crystal class makes ZnO a polar piezoelectric material.¹ This opens another viable path (in addition to field effect)

¹A non-centrosymmetric crystal structure is necessary but not sufficient for a material to be piezoelectric. Among 32 crystal classes 21 have no centres of symmetry, but only 20 are found to exhibit piezoelectricity with 432 cubic class being the only exception [159].

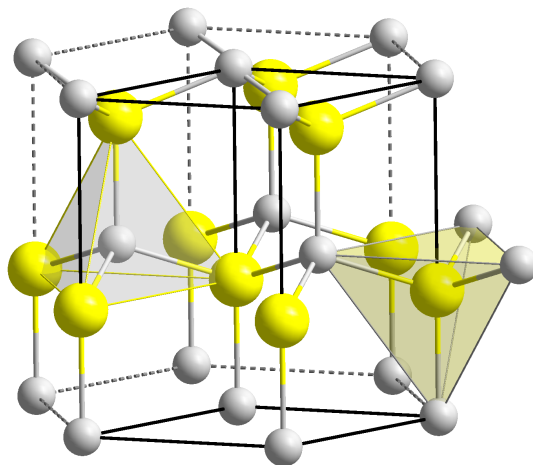


Figure 4.1 – Wurtzite crystal structure of ZnO. Yellow spheres represent Zn atoms, grey O atoms. Source: https://commons.wikimedia.org/wiki/File:Wurtzite_polyhedra.png, public domain.

for an electric field control of surface-adsorbed single-atom magnets. An application of an external electric field to a piezoelectric material brings about a mechanical deformation of the latter. This is so-called converse piezoelectric effect. The macroscopic deformation, in turn, is a result of the atomic displacements within the crystal unit cells. It is exactly these substrate atoms that create the CF, which plays a crucial role in the stability of an adatom spin. Thus, the external-field-controlled displacement of substrate atoms can affect the single adatom magnetisation lifetime.

Well-ordered ultrathin ZnO(0001) films have been grown on several metal substrates (*i.e.*, Ag(111) [160, 161], Au(111) [162, 163], Pd(111) [164], Pt(111) [165] and Cu(111) [166]). Zinc oxide grows in a layer-by-layer fashion and for the thicknesses larger than 4–5 ML the film relaxes to the bulk wurtzite crystal structure. Particularly interesting is the case of ZnO grown on Au(111), where the electric dipole developed in the ZnO film is compensated by the formation of a (2×2) surface reconstruction and the concomitant creation of a dipole at the metal-oxide interface [162]. These polarity compensation mechanisms avoid the formation of surface hydroxyls as frequently observed for ZnO grown on the more reactive Pt(111) surface [167] and on the O-terminated ZnO(0001) bulk surface [168]. The result is a film consisting of Zn atoms at the oxide-metal interface, while O atoms, H free, are located at the oxide-vacuum interface. The topmost layer of the (2×2) -reconstructed surface consists of O atoms arranged in a honeycomb structure, similar to the one observed at the bulk surface [168]. Two adsorption sites can be envisaged for the RE atoms: (a) O-top, generating a strongly uniaxial CF similar to the MgO/Ag(100) substrate [83]; (b) hollow, resulting in a highly symmetric (C_{6v}) CF resembling the graphene/Ir(111) case [81]. Both configurations lead to a highly symmetric uniaxial CF required for the long spin lifetime of surface adsorbed single atoms.

To conclude, ZnO exhibit two independent mechanisms for an electric field control of magnetic properties of surface-adsorbed single atoms (field effect and converse piezoelectric effect), which makes it a perfect candidate for this task. At the same time, ZnO/Au(111) thin films should exhibit a CF that can lead to exceptionally stable single-atom magnets. Current chapter is divided into two parts: first of all we demonstrate the long magnetic lifetime of Dy adatoms on ZnO/Au(111); the second part is devoted to the study of the electric field control of the magnetisation lifetime of Dy single atoms deposited on ZnO/SrTiO₃(110) substrate.

4.1 ZnO thin films on Au(111) single crystals

Thin films of ZnO were grown by Zn (99.99%, Goodfellow) evaporation from an effusion cell onto a Au(111) single crystals, kept at 300 K, in a partial oxygen pressure of 2×10^{-6} mbar. To ensure complete film crystallisation and oxidation, annealing in oxygen atmosphere ($p \approx 2 \times 10^{-6}$ mbar) has been performed after the deposition. The annealing procedure was limited to 20 minutes at 650 K with approximately 12 K/min temperature ramp rate, as longer annealing times, higher temperatures and higher ramp rates produce Zn desorption. This growth method resulted in ZnO thin films of good crystallinity as highlighted by the LEED images (fig. 4.2). A comparison of the experimentally obtained XLD spectra (fig. 4.3) with the ones reported in refs. [169–171] corroborated the high quality of the grown films. XAS measurements were also used to estimate the ZnO thickness. To this end, a roughly $d = 4.5$ ML thick (as identified by combining Auger spectroscopy and scanning tunneling microscopy [A. Fetida, EPFL master thesis]) calibration sample was produced in Lausanne. It was then utilised to calibrate the intensity of Zn L_{2,3} XAS edge as a function of the film thickness.

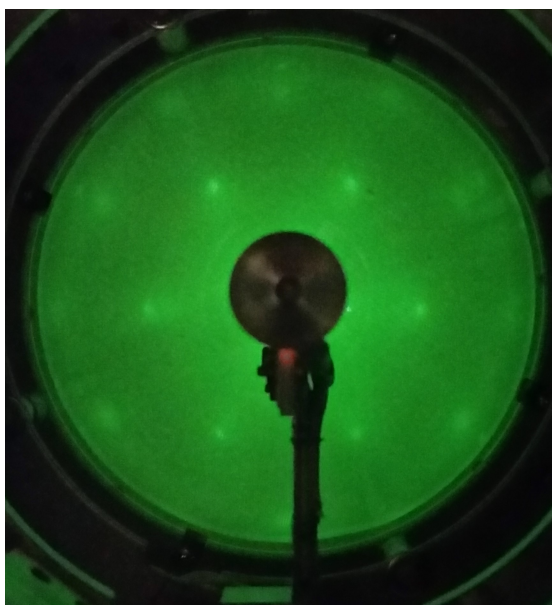


Figure 4.2 – LEED image of a 9.6 ML thick ZnO film grown on a Au(111) single crystal.

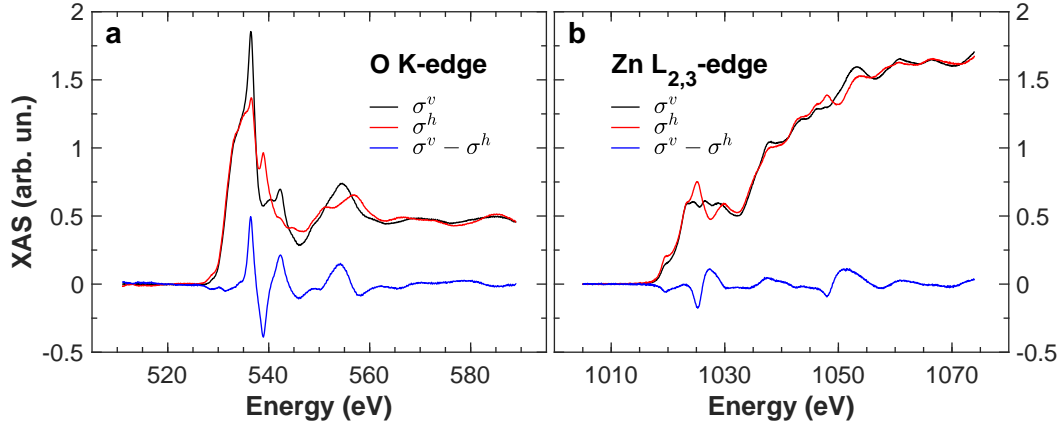


Figure 4.3 – Vertically (σ^v , black lines) and horizontally (σ^h , red lines) polarised (a) O K-edge and (b) Zn $L_{2,3}$ -edges XAS spectra together with the corresponding XLD spectra ($\sigma^v - \sigma^h$, blue lines) for a 9.6 ML thick ZnO film grown on a Au(111) single crystal.

4.2 Dy single atoms on ZnO/Au(111)

The XAS, XMCD and XMLD spectra of Dy single atoms deposited on ZnO/Au(111) are depicted in figs. 4.4a to 4.4c, respectively. From the multiplet structure of the XAS we deduced the Dy $4f^9$ electronic configuration. XMCD signal exhibits only a slight anisotropy with grazing intensity being higher than the normal one by approximately 15%. A tiny XMLD spectra with up-down shape corroborates the magnetic anisotropy revealed by XMCD measurements. The Dy magnetisation curves, measured at normal and grazing incidences, are shown in figs. 4.4d and 4.4e. The loops exhibit similar openings, indicating comparable long spin lifetimes at both magnetic field orientations. However, no anisotropy of Dy magnetic moment is found from the magnetisation curve measurements. Moreover, no steps in the magnetisation loops that would hint at a QTM have been observed.

From the sum rules we inferred an averaged magnetic moment of the ensemble of Dy spins to be about $5.3 \mu_B$ at both normal and grazing incidences. Furthermore, the shape of the Dy XAS spectra for Dy/ZnO/Au(111) (fig. 4.4a) resembles that of Dy/BaO/Pt(100) (fig. 3.1): both normal and grazing adsorption spectra basically coincide with only minor differences found in the intensities of the second (1287.4 eV) and the third (1289.3 eV) peaks. The multiplet simulations performed for Dy/BaO/Pt(100) system showed that such spectra cannot be reproduced only with the help of a single Dy species with ground doublet $J_z = \pm 4$ (which correspond to a magnetic moment of $5.3 \mu_B$). Instead, a combination of different Dy species located at multiple adsorption sites and exhibiting various magnetisation anisotropies should be used. This suggests that our ZnO thin films don't exhibit a single O termination, but rather a combination of two possible surface terminations: a hexagonal lattice of either Zn or O atoms (fig. 4.1). This fact further complicates the situation by increasing the total number of potential adsorption sites. Some Dy species must exhibit an out-of-plane magnetic anisotropy, others an in-plane one. As a consequence, the averaged magnetic moment measured with XMCD is isotropic.

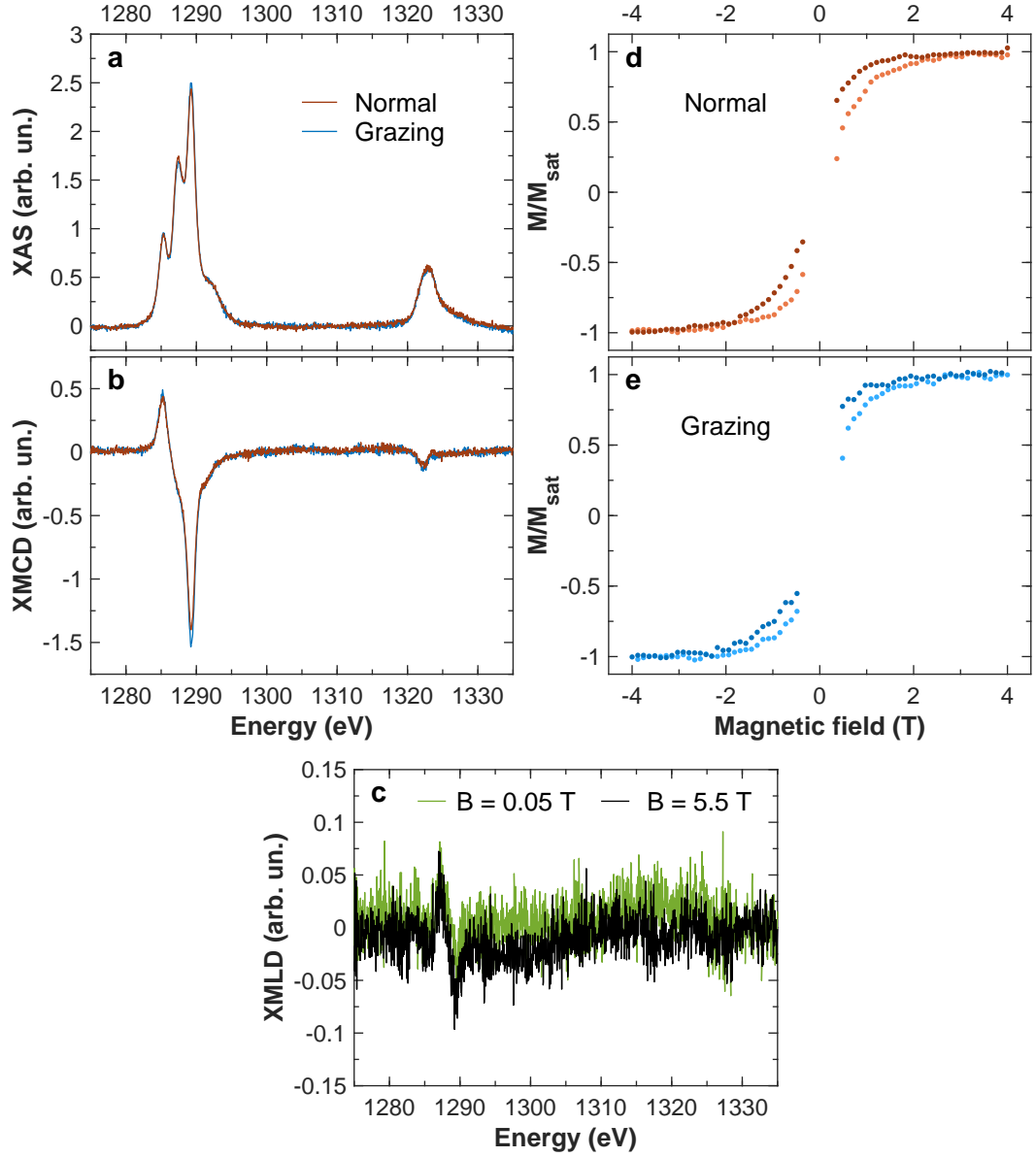


Figure 4.4 – (a) XAS, (b) XMCD, (c) XMLD spectra and (d, e) magnetisation curves of Dy adatoms on ZnO/Au(111) ($\Theta = 0.016\text{ML}$, $d = 7.7\text{ML}$, $T = 2.5\text{K}$). XMCD spectra were recorded at $B = 5.5\text{T}$ at normal and grazing incidences. XMLD spectra were measured at grazing incidence at $B = 5.5\text{T}$ and $B = 0.05\text{T}$. Magnetisation curves were obtained at (d) normal and (e) grazing incidences at $\phi = 2.8 \times 10^{-3}\text{ photon}/(\text{nm}^2\text{s})$.

Nonetheless, some of the individual adsorption sites induce a spin anisotropy strong enough to magnetically stabilise a Dy adatom, as highlighted by the openings in both normal and grazing magnetisation curves.

Moreover, Dy atoms on ZnO/Au(111) showed no change of spectra or magnetisation curves,

or any other sign of degradation with time or after heating up to 50 K and consecutive cool down. The robustness of this adatom/substrate combination against contaminations and clusters formation is atypical in comparison to the other RE based systems, especially $4f^{10}$ Dy surface supported single atoms [122]. Consequently, we were able to thoroughly study the magnetic properties of Dy adatoms on this substrate, including Dy coverage dependence, ZnO thickness dependence, magnetic relaxation measurements and temperature dependence.

4.2.1 Dy coverage dependence

The dependence of Dy magnetic properties on adatom surface coverage has been measured on an 11.6 ML thick ZnO film at $T = 2.5$ K. To this end we performed a series of Dy depositions on the same substrate while measuring the adatom magnetic properties after each deposition. Experimentally obtained XAS and XMCD spectra are shown in fig. 4.5. The XMCD signal intensities show a prominent coverage dependence (figs. 4.5c and 4.5d insets), indicating an overall decrease of ensemble-averaged Dy magnetic moments at higher adatom concentrations at both normal and grazing incidencies. The results of the sum rules analysis are given in

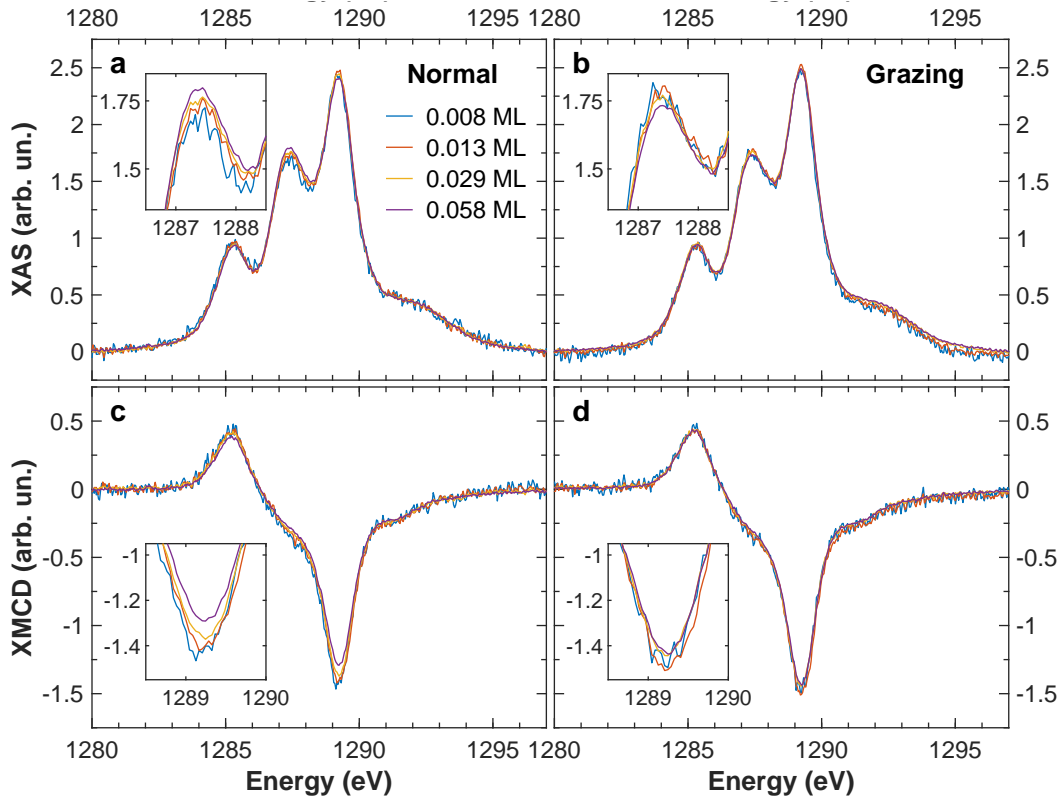


Figure 4.5 – Coverage dependence of Dy (a, b) XAS and (c, d) XMCD spectra measured at (a, c) normal and (b, d) grazing incidences ($d = 11.6$ ML, $T = 2.5$ K). Only M_5 edge is shown; the enlargements of (a, b) the XAS second peak and (c, d) the XMCD main peak are depicted in the insets.

Table 4.1 – Coverage dependence of Dy magnetic moments (μ) at normal and grazing orientations of the external magnetic field together with their grazing to normal ratios ($d = 11.6$ ML, $T = 2.5$ K).

Dy coverage (ML)	μ_{normal} (μ_B)	$\mu_{grazing}$ (μ_B)	$\frac{\mu_{grazing}}{\mu_{normal}}$
0.008	5.3 ± 0.3	4.6 ± 0.3	0.87 ± 0.07
0.013	4.8 ± 0.1	4.7 ± 0.1	0.98 ± 0.03
0.029	4.35 ± 0.05	4.64 ± 0.02	1.07 ± 0.01
0.058	3.97 ± 0.03	4.39 ± 0.04	1.11 ± 0.01

table 4.1. Even though both normal and grazing magnetic moments decrease with the adatom coverage, a stronger dependence at the normal orientation of the magnetic field leads to a change of the sample anisotropy from out-of-plane to in-plane at higher Dy concentrations. The ratios of grazing to normal magnetic moments are also shown in table 4.1. Moreover, with the help of the multiplet simulations one can demonstrate that the intensity of the second peak of the $4f^9$ Dy XAS multiplet structure depends strongly on the projection of the Dy spin onto the beam direction: the higher is the projection, the lower is the second peak. Experimentally we observe an increase of this XAS peak at normal incidence together with a reduction of the same peak at grazing incidence (figs. 4.5a and 4.5b insets) in agreement with the observed change of the magnetic anisotropy. Furthermore, the characteristic up-down shape of the XMLD spectra corroborates the in-plane spin anisotropy of Dy ensemble at higher adatom coverages (fig. 4.6). No such shape has been observed at lower Dy concentrations.

Dependence of the magnetisation curves on Dy coverage is depicted in fig. 4.7. As can be seen from the figure, the magnetisation curves at the highest Dy coverage are more closed than the other hysteresis loops. In this case, two phenomena can cause the reduction of the spin lifetime: Dy-Dy interaction or Dy dimers formation. The latter is expected to take place at coverages of about 0.06 ML [172]. Both of these effects may also be responsible for the detected change of the magnetic anisotropy. Taking into account the overall decrease of the averaged Dy spin we can speculate that both of these phenomena lead to an antiferromagnetic coupling between the adatoms at higher coverages. One possibility is that the Dy species with the out-of-plane magnetic anisotropy are more readily involved in such adatom interaction or

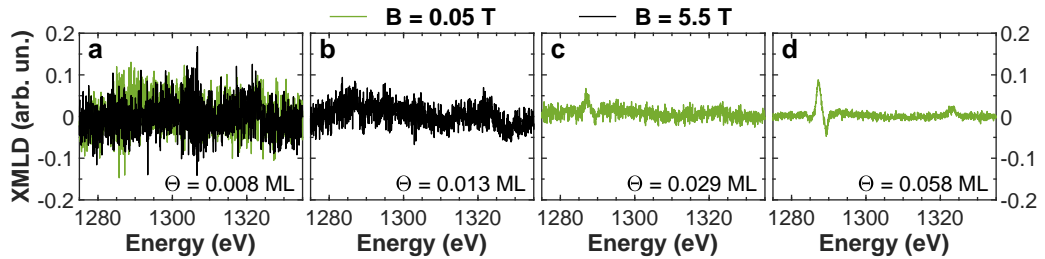


Figure 4.6 – Coverage dependence of Dy XMLD spectrum ($d = 11.6$ ML, $T = 2.5$ K).

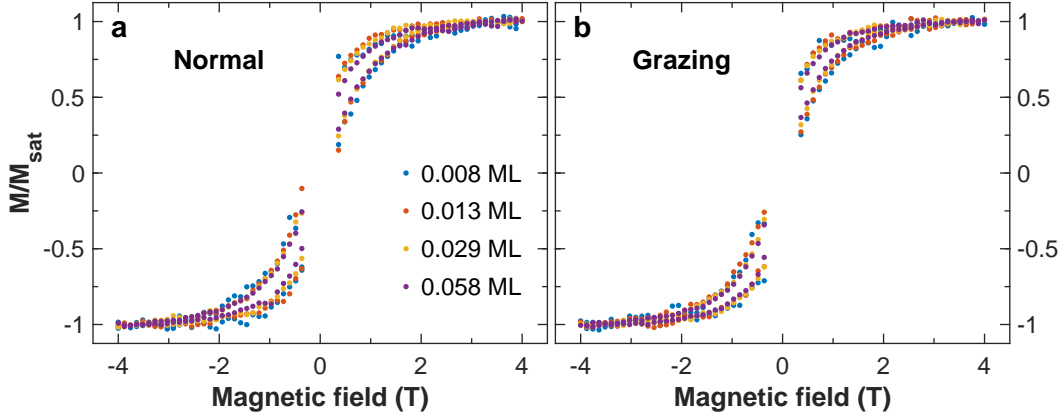


Figure 4.7 – Coverage dependence of magnetisation curves for Dy/ZnO/Au(111) measured at (a) normal and (b) grazing incidences ($\phi = 2.9 \times 10^{-3}$ photon/(nm² s), $d = 11.6$ ML, $T = 2.5$ K).

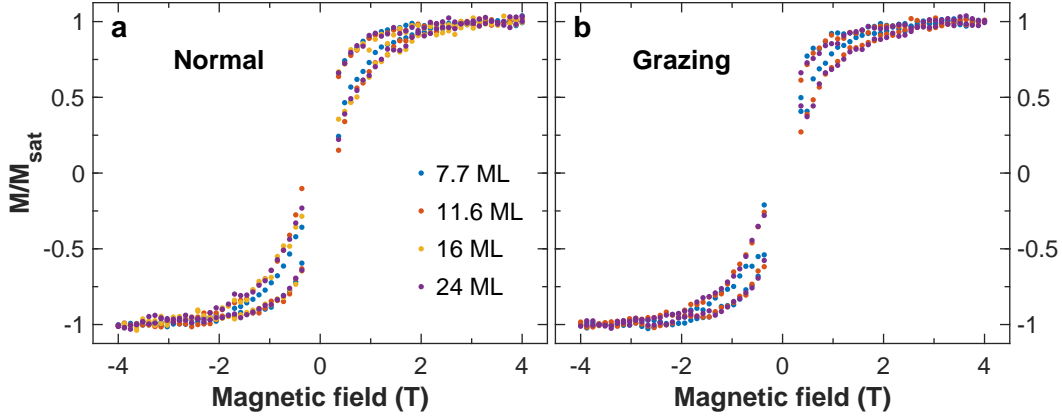


Figure 4.8 – ZnO-thickness dependence of the magnetisation curves for Dy/ZnO/Au(111) measured at (a) normal and (b) grazing incidences ($\Theta = 0.013$ ML, $T = 2.5$ K, $\phi = 2.8 \times 10^{-3}$ photon/(nm² s)). The saturation magnetisations of the loops are normalised to 1.

dimers formation, thus, leading to a faster decrease of the normal magnetisation component and a consequent change in the magnetic anisotropy of the Dy ensemble.

4.2.2 ZnO-thickness dependence

Furthermore, we studied the influence of the decoupling layer thickness on the magnetic stability of Dy adatoms. The magnetisation loops measured on the samples with different ZnO film thicknesses are depicted in fig. 4.8. The saturation levels of the curves were normalised to 1 for an easier comparison of the loop openings. As can be seen from the figure, the loop measured on the thinnest film is more closed than the other loops. Apparently, ZnO films thinner than 10 ML are less efficient in prevention of the gold hot electrons and phonons scattering with the surface-adsorbed Dy atoms [66, 82, 83] (ZnO speed of sound is 2730 m/s

[173], while for Au it is 2110 m/s [174]). No other changes in the Dy magnetic properties have been detected.

4.2.3 Dy magnetic relaxation times

A typical Dy spin relaxation curve is shown in fig. 4.9a. Figure 4.9b displays the magnetic field dependence of the relaxation time. Time constants τ of about 400 s are found for $B \leq 0.5$ T. At $B = 0.8$ T the relaxation time increases to approximately 600 s. No signs of the ‘butterfly’ shape of the magnetisation loop, *i.e.* a significant reduction of the relaxation time around $B = 0$ T, is observed. In any case, the $4f^9$ Dy electronic configuration leads to a half-integer $J = \frac{15}{2}$ ground multiplet, which is protected from QTM exactly at zero field by time-reversal symmetry [111].

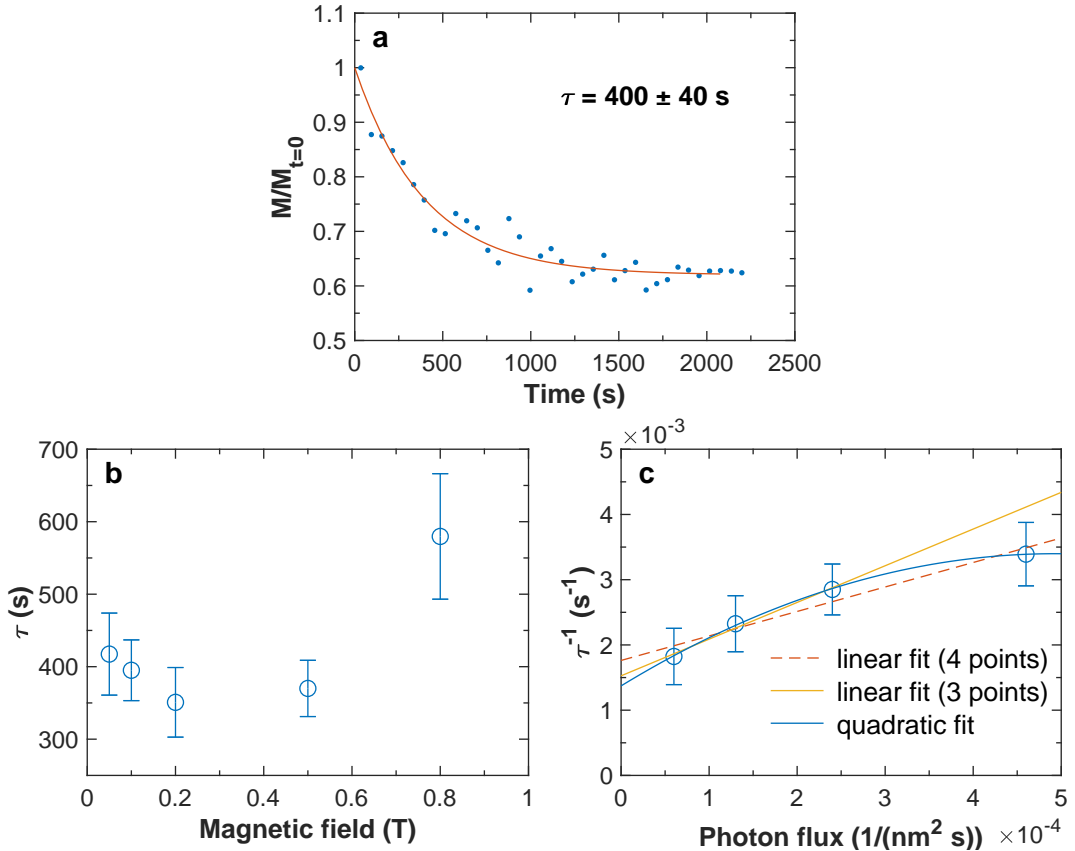


Figure 4.9 – Spin relaxation dynamics of Dy/ZnO/Au(111) ($\Theta = 0.012$ ML, $d = 16$ ML, $T = 2.5$ K, normal incidence). (a) Spin relaxation curve at $B = 0.1$ T and $\phi = 2.4 \times 10^{-4}$ photon/(nm² s). (b) Magnetic field dependence for $\phi = 2.4 \times 10^{-4}$ photon/(nm² s). (c) Photon flux dependence at $B = 0.2$ T. Red dashed line is a linear fit through all four points; yellow solid line is a linear fit through first three data points, while blue solid line denotes a quadratic fit through all four data points.

The photon flux dependence of the Dy relaxation time shown in fig. 4.9c indicates an increase of the relaxation rate τ^{-1} at higher flux, in agreement with the flux dependences observed for other surface-adsorbed magnetic atoms or molecules [66, 77, 81, 83]. This dependence was previously explained by secondary electron induced sample demagnetisation. The total relaxation rate is a sum of the intrinsic relaxation rate and secondary electron induced relaxation rate: $\tau^{-1} = \tau_{int}^{-1} + \tau_{el}^{-1}$. In references [83] and [77] a linear flux dependence $\tau_{el}^{-1} = \sigma\phi$ was observed, which allowed to retrieve the intrinsic relaxation rates. If we also assume such a linear dependence for Dy/ZnO/Au(111), then the linear fit extrapolation to zero photon flux gives an intrinsic relaxation time of (570 ± 70) s (see red dashed line in fig. 4.9c). However, in our case the Dy relaxation rate shows tendency to saturation at higher photon fluxes, as demonstrated by the quadratic fit (see blue solid line in fig. 4.9c). Hence, we also performed the linear fit using only the first three experimental data points. The result is shown in fig. 4.9c with yellow solid line. From the three-point fit we obtained the intrinsic Dy relaxation time of (650 ± 80) s.

The slopes of the linear fits provide us with the cross section σ of the secondary photon induced demagnetisation process. In our case we deduced $\sigma = (38 \pm 8)$ Gb from the four-point fit and $\sigma = (56 \pm 12)$ Gb from the three-point fit. These values are one order of magnitude higher than those reported in [77, 83], which points to a much higher efficiency of the secondary photon induced demagnetisation in our experiment. In these former works MgO was used as a substrate for Ho single atoms and Tb based single molecules. Since ZnO absorption coefficient at Dy M_5 edge ($3.6 \mu\text{m}^{-1}$) is 2.5 times higher than adsorption coefficient of MgO at Ho M_5 edge ($1.5 \mu\text{m}^{-1}$) and 8 times higher than adsorption coefficient of MgO at Tb M_5 edge ($0.44 \mu\text{m}^{-1}$), we ascribe the observed difference in the sample demagnetisation efficiency to the increased number of secondary electrons generated close to the surface in ZnO. This suggests that narrower openings in Dy/ZnO/Au(111) magnetisation curves in comparison to the other single-atom magnets [81, 83] is only partially due to a faster intrinsic relaxation of Dy adatoms and partially caused by the experimental technique. As the magnetic field dependence of the relaxation rate has been measured at the close-to-saturation photon flux, the observed relaxation times are strongly limited by the secondary electron demagnetisation process, which explains an only weak magnetic field dependence observed in fig. 4.9b.

4.2.4 Temperature dependence

The temperature dependence of the Dy magnetisation curve is given in fig. 4.10. Two typical phenomena are observed. The first one is a reduction of the magnetic susceptibility, which is revealed by an overall flattening of the hysteresis loop. The second is a decrease of the Dy spin lifetime, as highlighted by the diminution of the magnetisation curve opening. We find an open hysteresis loop for the temperatures up to 8 K. For comparison, Ho/MgO/Ag(100) exhibits an open magnetisation curve up to 30 K [83], while Dy/graphene/Ir(111) hysteresis loop is closed at 12 K. No studies of temperature dependence between 3 K and 12 K have been performed for Dy/graphene/Ir(111) system [81].

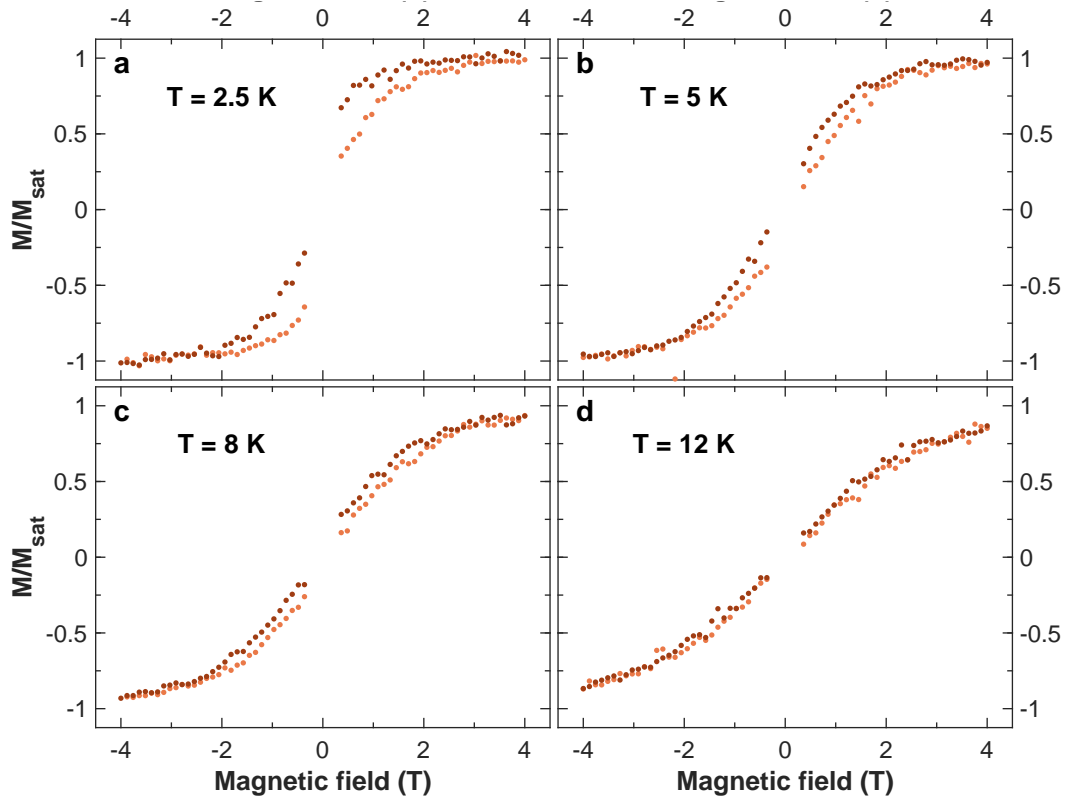


Figure 4.10 – Temperature dependence of the magnetisation curve of Dy on ZnO/Au(111) ($\Theta = 0.012$ ML, $d = 16$ ML, $\phi = 5.6 \times 10^{-3}$ photon/(nm² s), normal incidence).

4.3 Ho single atoms on ZnO/Au(111)

We also studied magnetic properties of Ho single atoms deposited on ZnO/Au(111) thin film. Here, the observed spectra are once again very similar to those of Ho adatoms on BaO/Pt(100) (fig. 4.11). Holmium is found in $4f^{10}$ electronic configuration. The XAS spectra at normal and grazing incidence coincide; there is no anisotropy of XMCD signal, as also corroborated by the XMLD spectra. All this suggests that Ho adatoms are adsorbed at multiple sites with different magnetic anisotropies, similarly to Dy single atoms. Both normal and grazing hysteresis loops show no evidence of an opening, indicating that in this case the Ho spin relaxation time is of the order of a few seconds.

4.4 ZnO thin films on SrTiO₃(110) single crystals

Since metallic conductivity of gold would not allow us to apply an external electric field to the sample, we grew ZnO thin films on strontium titanate (SrTiO₃, STO) single crystals. The latter is an insulating oxide with a very large dielectric constant ($\approx 10^4$ below 10 K [175]). If we place a ZnO/STO sandwich into a parallel-plate capacitor, then the distribution of the electric

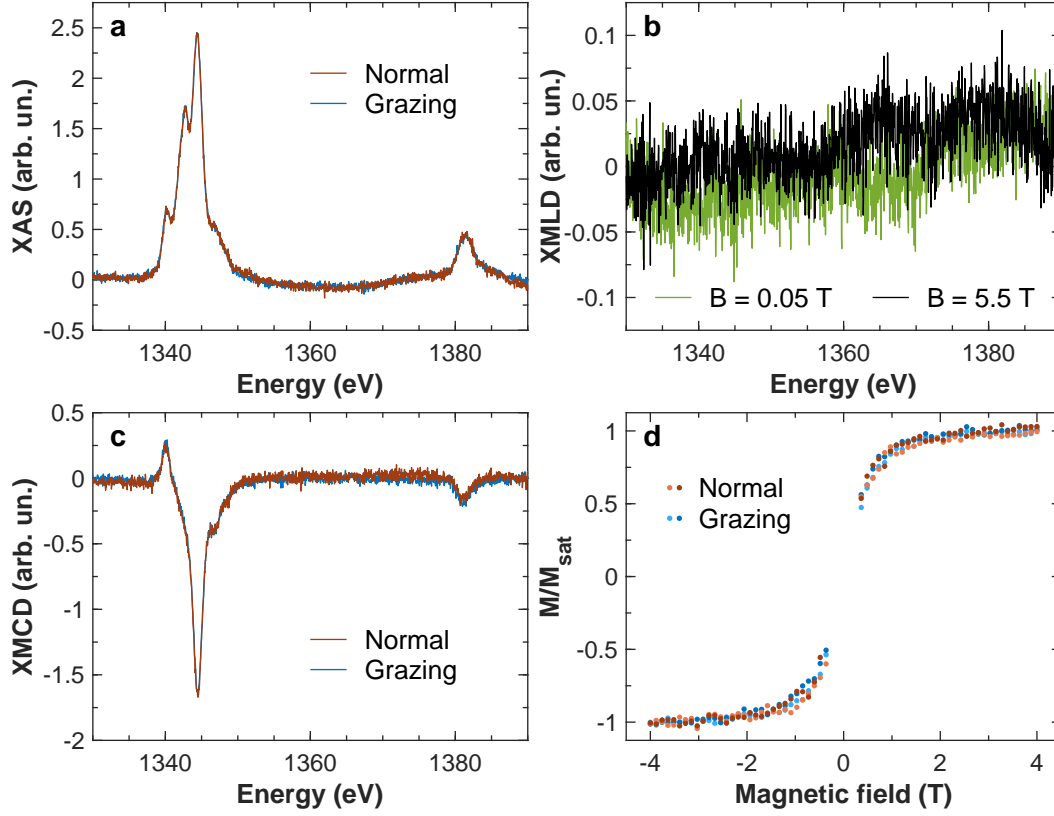


Figure 4.11 – (a) XAS, (b) XMLD, (c) XMCD spectra and (d) magnetisation curves of Ho adatoms on ZnO/Au(111) ($\Theta = 0.012\text{ ML}$, $d = 24\text{ ML}$, $T = 2.5\text{ K}$). XMCD spectra were recorded at $B = 5.5\text{ T}$ at normal and grazing incidences. XMLD spectra were measured at grazing incidence at $B = 5.5\text{ T}$ and $B = 0.05\text{ T}$. Magnetisation curves were obtained at normal and grazing incidences at $\phi = 4.6 \times 10^{-3}\text{ photon}/(\text{nm}^2\text{ s})$.

field between the two layers is inversly proportional to their dielectric constants. Taking into account the giant dielectric constant of STO, we get that the electric field applied to the sandwich is ‘pushed’ out of STO into the ZnO film, which is exactly what we need to maximise the efficiency of the field effect.

Zinc oxide thin films were grown on STO(110) substrates using pulsed laser deposition technique by Dr. Emilio Bellingeri (Consiglio Nazionale delle Ricerche/CNR-SPIN u.o.s. Genova) and Prof. Dr. Daniele Marre (Dipt. di Fisica, Univ. di Genova) in Italy. Prior to Dy deposition the samples were annealed in oxygen atmosphere ($p \approx 2 \times 10^{-6}\text{ mbar}$) for approximately 10 min. We had to limit the annealing temperature to 470 K as a loss of oxygen by STO substrate took place at higher temperatures. Since oxygen deficient STO is conductive, this would render impossible the field effect experiments. LEED and XLD measurements were used to characterise ZnO/STO(110) films, similarly to ZnO/Au(111). No significant differences were found between the films grown on the two different substrates.

4.4.1 Characterisation of ZnO/STO(110) films for field effect measurements

A sample holder with a typical ZnO/STO sample is depicted in fig. 4.12. A sample was mounted with a conductive cohesive paint ('silver paint') on an omicron-type plate, which served as a gate contact. The plate was made of tantalum and was in direct electrical contact with the copper sample holder. It was fixed with the screw at the back of the sample holder, which is not shown in the figure. Copper-berillium spring plates were used to produce source and drain contacts. The latter were isolated from the sample holder (kept at the potential of the gate contact) by insulating sapphire spacers. The TEY signal was measured on the source-drain contacts. This sample holder design allowed us: (a) to deposit Dy atoms on the ZnO and perform required X-ray measurements since a substantial part of the surface is not covered by any contacts; (b) to remove the omicron-type plate with the sample from the sample holder inside the UHV chamber and carry out the necessary surface preparation.

The results of the direct field effect measurements on a ZnO thin film at $T = 2.5\text{ K}$ are shown in fig. 4.13. The same $R(V_g)$ dependencies (V_g - gate voltage, R - source-drain resistance) were found for the samples under the X-ray radiation and without it. As a voltage source we used a set of batteries connected in series. This helped us to avoid the noise, associated with the voltage rectification in conventional DC voltage sources, and perform the X-ray measurements in TEY mode even with the external electric field applied on the sample. A special switch was used to control the output voltage between 0 V and 200 V with step of 20 V.

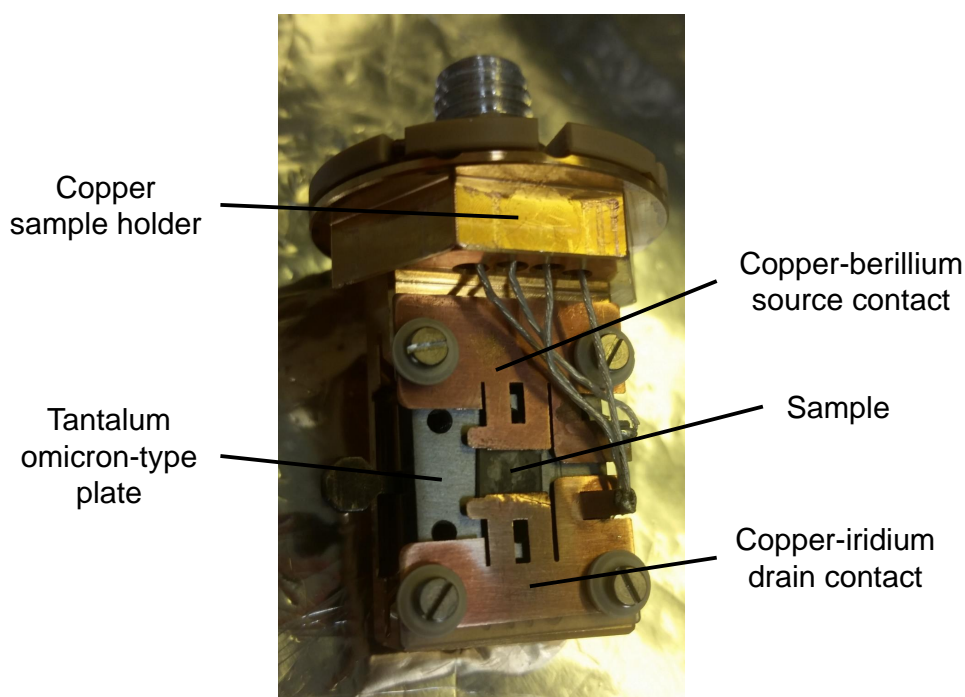


Figure 4.12 – ZnO/STO(110) sample in a sample holder.

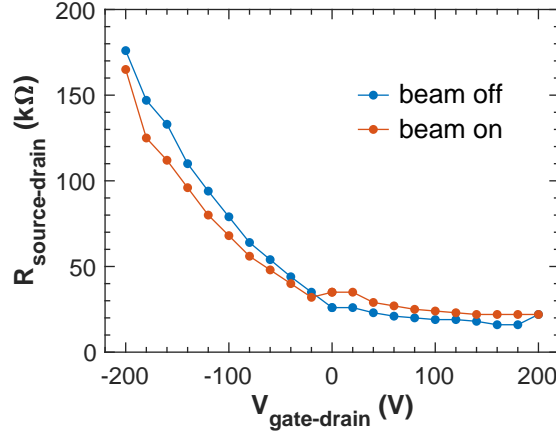


Figure 4.13 – Field effect measurements on a 54 nm thick ZnO/STO(110) film at 2.5 K. Blue dots correspond to the measurements without X-ray beam, while red dots denote the measurements with X-ray beam hitting the sample. The sign of the voltage correspond to the polarity of the gate contact.

4.5 Dy single atoms on ZnO/STO(110)

XAS and XMCD measurements of Dy single atoms adsorbed on top of the ZnO/STO(110) thin films are shown in figs. 4.14a and 4.14b. No changes in the spectra are found in comparison to Dy/ZnO/Au(111) samples. Magnetisation curves of Dy single atoms on ZnO/STO(110) substrate are depicted in figs. 4.14c and 4.14d. The openings of the hysteresis loops, indicating a long Dy magnetic lifetime, can still be observed for both normal and grazing incidencies, even though they are much narrower than the openings of the Dy/ZnO/Au(111) magnetisation curves. In general, one should expect a higher sample temperature in the currently presented measurements as extra parts (source and drain contacts together with the insulating spacers and wires) were added to the sample holder. Indeed, from the comparison of the magnetisation loop curvatures and openings in fig. 4.14(c,d) and fig. 4.10 we estimated the sample temperature to be around 4.5 K. The similarity of the Dy magnetic properties on ZnO/Au(111) and ZnO/STO(110) corroborates the fact that two possible surface terminations coexist in thin films grown on both substrates.

4.5.1 Electric field control of the Dy magnetic lifetime

We studied the effect of the external electric field on the magnetic properties of the Dy single atoms deposited on ZnO/STO(110) substrates by applying gate voltages ranging from -200 V to 200 V. Under depletion conditions (negative V_g), we observed an increase of the XMCD signal of Dy acquired at saturation ($B = 4$ T), which corresponds to an increase of the spin and orbital moments by about 10% (fig. 4.15). Magnetic hysteresis was observed for $V_g = 0$ V and under accumulation conditions (positive V_g), while Dy atoms became paramagnetic under depletion conditions (fig. 4.16). These observations show that we can switch on and off the Dy

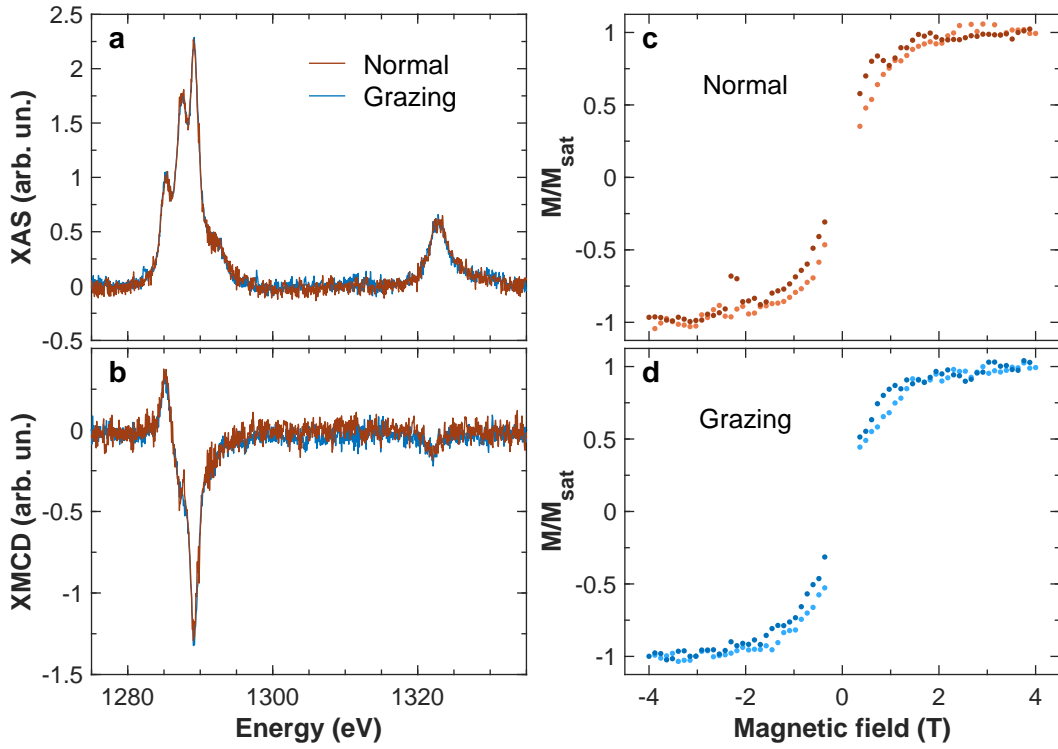


Figure 4.14 – (a) XAS and (b) XMCD spectra and (c,d) magnetisation curves of Dy adatoms on ZnO/STO(110) ($T = 4.5$ K). XMCD spectra were recorded at $B = 5.5$ T at normal and grazing incidences ($\Theta = 0.015$ ML, $d = 39$ ML). Magnetisation curves were obtained at (c) normal and (d) grazing incidences ($\Theta = 0.017$ ML, $d = 19$ ML, $\phi = 3.3 \times 10^{-3}$ photon/(nm² s)).

hysteretic behavior and modify the Dy magnetic moment with external electric field.

On the one hand, no significant variation as a function of the gate voltage is observed in the linear spectra of O, Zn, and Dy. This suggests that the CF is not significantly modified by the electric field and the density of the charge carriers have a strong effect on the Dy magnetism. On the other hand, one would expect a longer Dy magnetisation lifetime under depletion conditions due to reduced spin-electron scattering, while experimentally we observe the opposite result. In addition, Dy saturation magnetic moment does not depend on the charge carrier density, whereas CF can modify it significantly. Taking into consideration these facts we hypothesise that the converse piezoelectric effect plays a crucial role in electric-field control of Dy magnetic properties. To corroborate our theory we measured a ferroelectric hysteresis loop on a ZnO/STO(110) sandwich (fig. 4.17). The saturation values at ± 15 arbitrary units in fig. 4.17 correspond to a saturation limits of an operational amplifier used in an experimental circuit and they don't represent the real ferroelectric saturation of the sample. Thus, the minor loop is depicted in fig. 4.17, which, nevertheless, still shows the signs of ferroelectric switching. Since bulk STO is a quantum paraelectric [176], we attribute the observed ferroelectric hysteresis to the ZnO thin film. Previously, ferroelectric behaviour has been detected in Li-doped ZnO thin films [177] and undoped ZnO nanorods [178]. Even though this is not a direct measurement

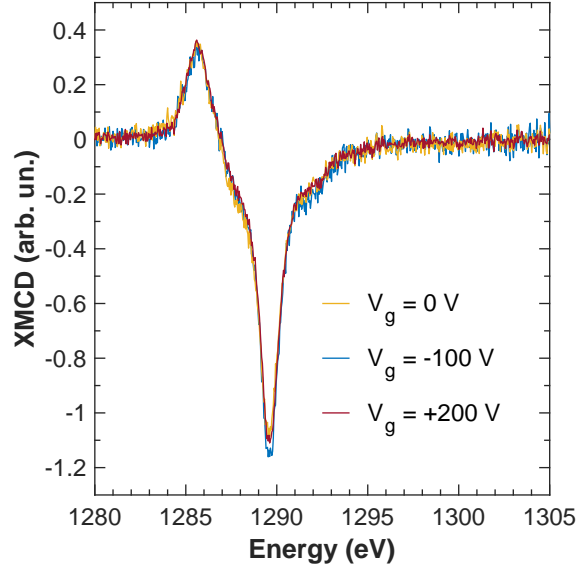


Figure 4.15 – Zoom on the XMCD signal at the M_5 edge for gate voltages $V_g = 0\text{ V}$, -100 V and $+200\text{ V}$ (in the temporal order of the measurements, $B = 4\text{ T}$).

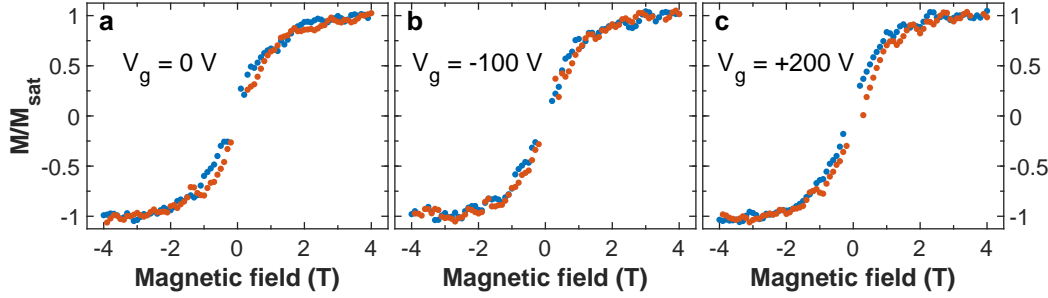


Figure 4.16 – Dy magnetisation curves acquired at $V_g = 0\text{ V}$, -100 V and $+200\text{ V}$ (in the temporal order of the measurements, $d = 54\text{ ML}$, $\phi = 1 \times 10^{-2}\text{ photon}/(\text{nm}^2\text{ s})$).

of the piezoelectric effect, the two phenomena are closely related. Both ferroelectricity and piezoelectricity are caused by a distortion of a crystal unit cell. Therefore, the ferroelectric loop in fig. 4.17 supports the fact that we are able to control the CF of the ZnO film as well as the magnetic properties of the Dy adatoms.

4.6 Conclusion and outlook

To summarise, the magnetic properties of Dy single atoms deposited on ZnO/Au(111) and ZnO/STO(110) substrates have been studied. Dysprosium on ZnO/Au(111) exhibits a long spin lifetime up to 600 s, which is shorter than magnetisation lifetime of Ho/MgO/Ag(100) [83] and Dy/graphene/Ir(111) [81] but longer than that of Dy/BaO/Pt(100) (see section 3.2). Our study of Dy/ZnO/STO(110) suggests field effect control of the adatom magnetic properties;

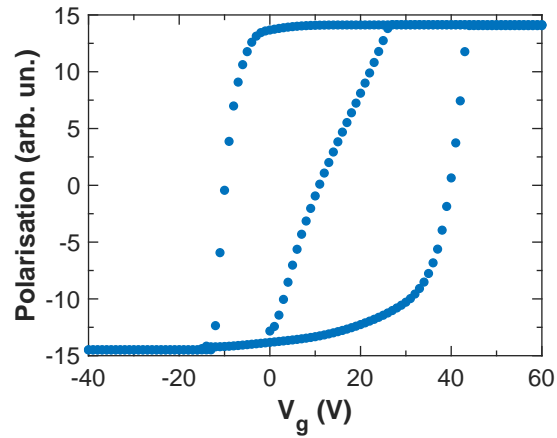


Figure 4.17 – Ferroelectric hysteresis loop of a ZnO/STO(110) thin film ($d = 46$ ML).

however, extra measurements are necessary to better understand the observed experimental phenomena. The main advantage of electric field over magnetic field is that one can control it at a much shorter time scale. Hence, the electric field control is an important step towards future applications of surface supported single atoms as bits of information in prospective computing devices.

5 Electron and Phonon Induced Demagnetisation of Single-Atom Magnets

Two key factors limit the magnetic lifetime of single-atom magnets: the CF symmetry and the coupling to both substrate electronic and vibrational degrees of freedom. The former can induce QTM, while the latter facilitate the thermally activated spin reversal via excited states. Usually, one should take both factors into account when describing the magnetic stability of the surface atoms. For example, in chapter 3 we compared the Dy/BaO/Pt(100) (Ho/BaO/Pt(100)) with Dy/MgO/Ag(100) (Ho/MgO/Ag(100)) SAMs, and we found that both CF and spin-phonon scattering favour a stronger magnetic stability of the adatoms on MgO. Often, it is almost impossible to disentangle the contributions of the different spin reversal mechanisms to the observed magnetisation relaxation.

In this chapter, we address this issue by comparing the magnetic properties of Dy adatoms deposited on graphene layers supported by various metallic substrates. Graphene (gr) is a single layer of carbon atoms arranged into a honeycomb structure [179]. Its ability to stabilise the adatom magnetic moment was demonstrated for the Dy/gr/Ir(111) system [81]. Graphene naturally provides a single adsorption site for the RE adatoms, which is the C_{6v} symmetric hollow site in the centre of the graphene ring. Moreover, its weak Van der Waals interaction with the underlying metal minimises the influence of the latter on the CF at the adatom position. Thus, one can expect that a very similar CF acts on the RE adatoms deposited on graphene grown on different substrates, showing the same van der Waals interaction with graphene. On the contrary, the graphene Fermi level can be shifted by the interaction with the substrate [180–187]. Thereby, adatom/gr/metal samples are ideal systems for the investigation of the effect of the substrate electron DOS on the adatom magnetic stability. Furthermore, the stiffness of the graphene layer helps to decouple the magnetic adatoms from the vibrational modes of the metallic substrate. Thus, the addition of a second graphene sheet should improve the decoupling from the metal substrate phonons without degrading the CF properties.

In the following, the magnetic properties of Dy single atoms deposited on a single layer of graphene grown on Pt(111) (gr/Pt(111)) or on polycrystalline Cu (gr/Cu), and on a bilayer of graphene on polycrystalline Cu (gr_{BL}/Cu) are presented. We compare our results with Dy/gr/Ir(111) to identify the impact of the metallic substrate on the Dy magnetic stability.

In addition, the comparison between gr/Cu and gr_{BL}/Cu samples is performed in order to determine the influence of the decoupling layer thickness.

5.1 Substrates preparation and characterisation

The Pt(111) (Ir(111)) substrate was prepared in situ by repeated cycles of Ar⁺ ion sputtering and successive annealing at 1300 K. A single layer of graphene was grown on Pt(111) (Ir(111)) single crystal by chemical vapour deposition (CVD) through exposure of the substrate to 100 L of ethylene at 1070 K (1300 K) with subsequent annealing for 1 minute at the same temperature [185, 188]. The CVD technique was also used to grow graphene on commercial Cu foils at the crystal growth facility at EPFL following standard recipe [189, 190]. An STM image of gr/Cu (fig. 5.1a) shows a stripe pattern, which we ascribe to the Moiré structure resulting from the mismatch between graphene and Cu(100) lattice constants [191]. A study of a 600 × 600 nm² area suggested that our polycrystalline Cu consists predominantly of Cu(100) termination (the same conclusion was made in ref. [192]). A high-resolution STM image clearly reveals the graphene honeycomb lattice (fig. 5.1b). The second layer of graphene was piled onto the gr/Cu substrate by means of a mechanical transfer method [189, 193]. Both gr/Cu and gr_{BL}/Cu samples were annealed in UHV at about 700 K for approximately 15 minutes in order to degas adsorbates due to air exposure. The quality of our graphene was verified with X-ray linear dichroism (XLD) at the carbon K edge (fig. 5.2). The π^* and σ^* peaks are clearly visible on the spectra, corroborating the high degree of crystallinity of our samples. Moreover, the XAS intensity scales as expected with the number of the graphene layers.

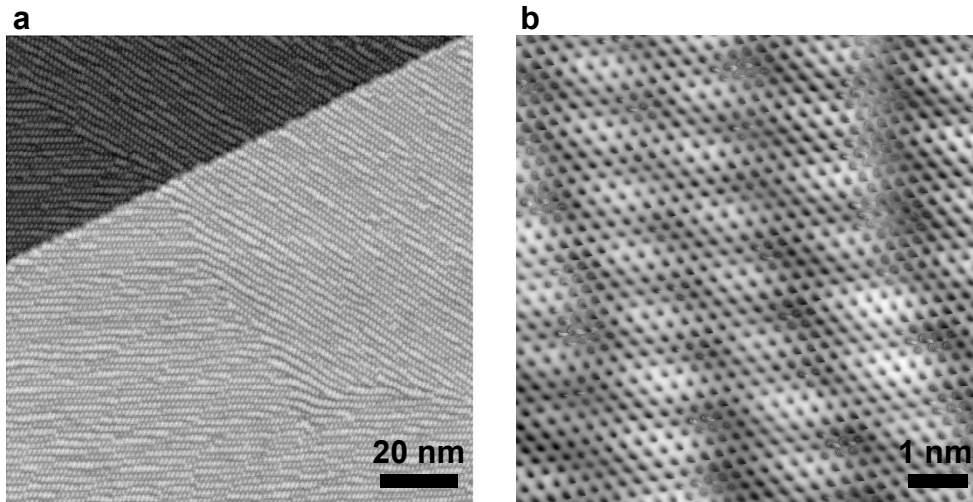


Figure 5.1 – Low temperature STM images of gr/Cu showing (a) the Moiré pattern on different domains (20 mV, 100 pA) and (b) high-resolution STM image of panel (a) showing the Moiré pattern superposed on the honeycomb graphene lattice (20 mV, 1 nA).

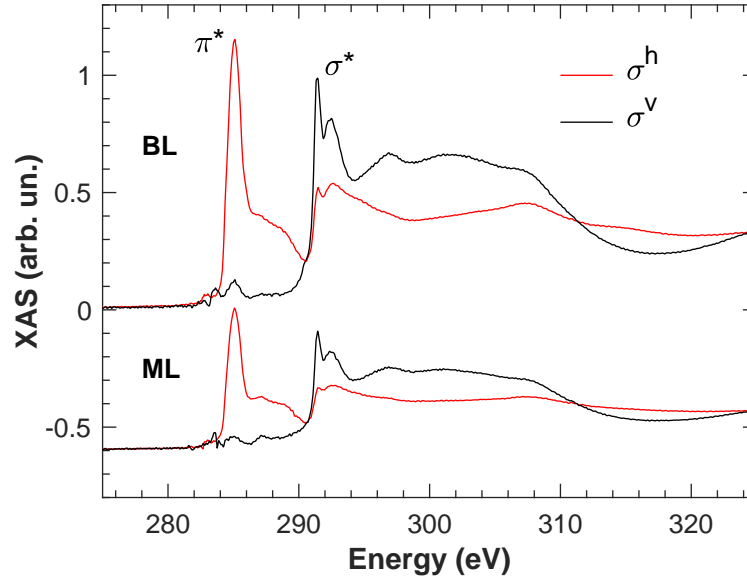


Figure 5.2 – XLD measurement at the C K-edge of a graphene monolayer (ML) and a bilayer (BL) on Cu substrate at grazing incidence.

5.2 X-ray absorption spectra

Identical X-ray adsorbption spectra were found for Dy single atoms deposited on all four investigated substrates. The XAS (top panels), XMCD (middle panels) and XMLD (bottom panels) experimental spectra of Dy/gr/Pt(111) and Dy/gr/Cu_BL are depicted in fig. 5.3a and fig. 5.3b, respectively (the spectra for Dy/gr/Ir(111) can be found in ref. [81]). From the XAS spectra we deduced that the adatoms are predominantly in the $4f^{10}$ electronic configuration with a small fraction of them being in the $4f^9$ configuration. The proportion of the trivalent atoms can be estimated from the height of the fourth XAS peak at 1290 eV which is specific to Dy atoms in the $4f^9$ configuration [136]. On all substrates Dy shows tendency to change its electronic configuration from $4f^{10}$ to $4f^9$ with time [122]. We ascribe this fact to the contamination of the adatoms with molecules of the residual gas in the cryostat [122, 194]. The observation of the peak at 1290 eV also immediately after deposition is ascribed to Dy adsorption at defect sites, as, for example, the domain edges or some residual impurities not removed by the annealing procedure. The similarity of Dy XMCD spectra suggests that Dy magnetic moment is equal for all four samples. Furthermore, the Dy monomers exhibit out-of-plane magnetic anisotropy, as can be seen by the higher XMCD signal at normal compared to grazing incidence. This fact is also corroborated by the down-up shape of the XMLD signals, which is typical for Dy adatoms with out-of-plane spin anisotropy. The multiplet simulations from ref. [81] reproduce well our experimental spectra (fig. 5.3c). This calculations were performed for the divalent electronic configuration of Dy and, thus, show no rightmost peak around 1290 eV.

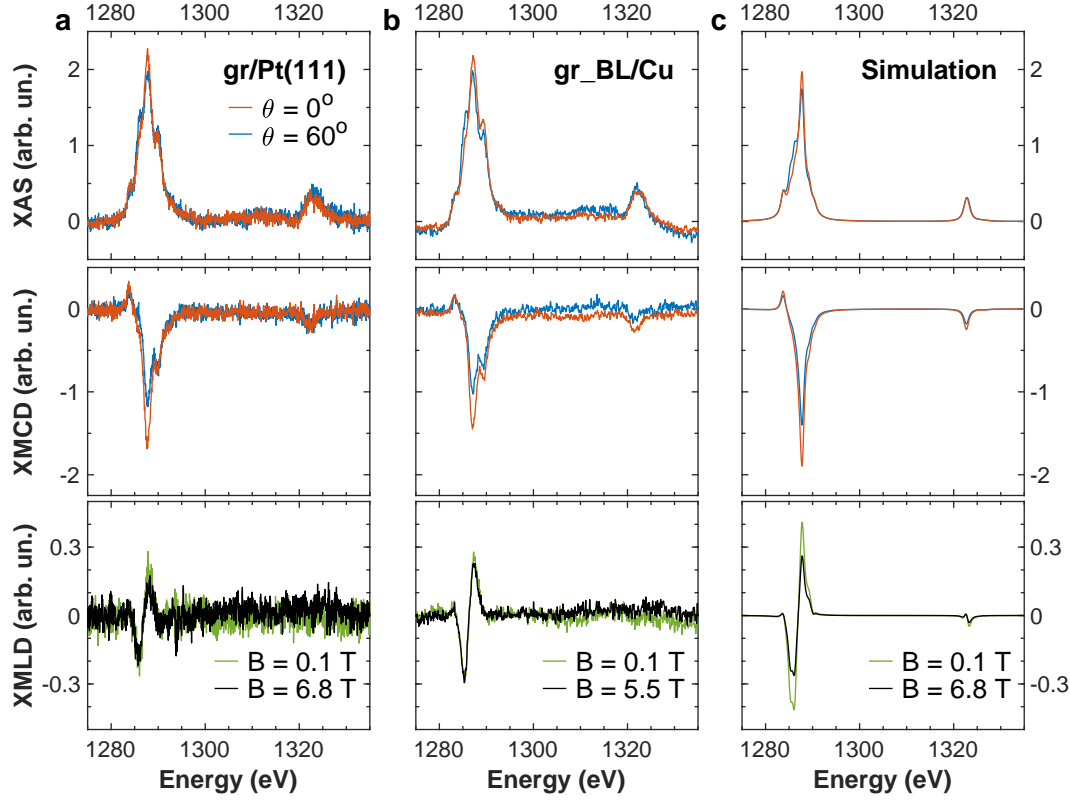


Figure 5.3 – XAS (top panels), XMCD (middle panels) and XMLD (bottom panels) spectra of (a) 0.009 ML of Dy on gr/Pt(111) and (b) 0.01 ML of Dy on gr/Cu_{BL}. XAS and XMCD spectra were measured at normal and grazing incidences at $B = 6.8$ T (gr/Pt(111)) and $B = 5.5$ T (gr/Cu_{BL}). XMLD spectra were recorded at grazing incidence in low magnetic field (0.1 T) and saturation magnetic field (6.8 T for gr/Pt(111) and 5.5 T for gr/Cu_{BL}). (c) Multiplet simulations performed for the experimental conditions of sample gr/Pt(111).

5.3 Magnetisation curves

The main effect of the metallic support is observed in the shape of the magnetisation curves (fig. 5.4). Here we add the magnetisation loop of Dy on gr/Ir(111) for the sake of comparison. Dy on all three substrates shows hysteresis and remanence of the magnetic moment. Since we measure in TEY mode, the data points are highly scattered for small fields. Assuming a linear dependence of the magnetisation on the magnetic field in that region, we get the highest remanence for Dy/gr/Ir(111), which amounts to about 28 % of the saturation magnetisation. For Dy/gr/Cu and Dy/gr/Pt(111) the remanence is approximately 22 %. Several steps, which are signatures of QTM, are found in the hysteresis loops. Dy/gr/Ir(111) and Dy/gr/Cu samples exhibit two pairs of such steps at $B = \pm 2.7$ T and $B = \pm 5.6$ T. Their hysteresis loops are open up to $B = 5.6$ T, *i.e.*, until the second QTM step. On the other hand, Dy/gr/Pt(111) displays only one pair of steps at $B = \pm 2.7$ T, since its magnetisation saturates already after the first step. Moreover, both Dy/gr/Ir(111) and Dy/gr/Cu show identical hysteresis curve openings between

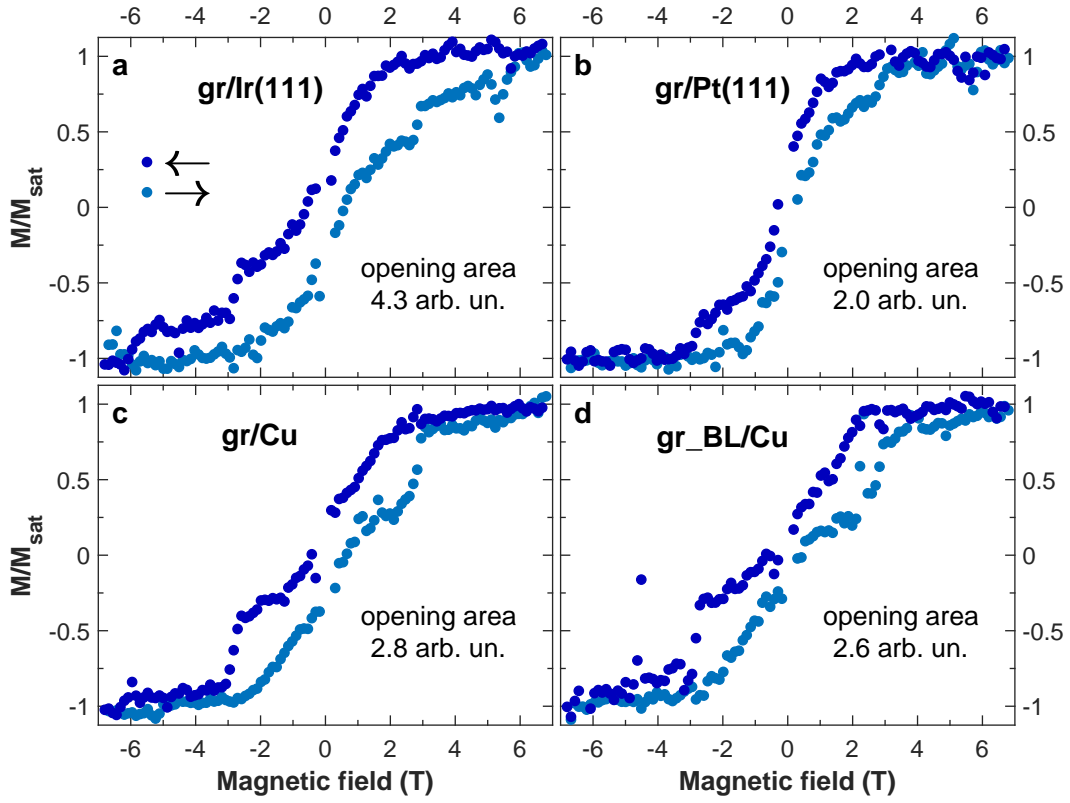


Figure 5.4 – Magnetisation curves of (a) 0.012 ML of Dy on gr/Ir(111), (b) 0.01 ML of Dy on gr/Pt(111), (c) 0.014 ML of Dy on gr/Cu and (d) 0.011 ML of Dy on gr/Cu_{BL}. All the curves are measured at normal incidence and at $T = 2.5$ K. The photon fluxes were 5.4×10^{-3} photon/(nm² s) (Dy/gr/Ir(111) and Dy/gr/Pt(111)) and 5.9×10^{-3} photon/(nm² s) (Dy/gr/Cu and Dy/gr_{BL}/Cu).

$B = \pm 2.7$ T. On the contrary, between $B = 2.7$ T and $B = 5.6$ T the former demonstrates a much broader opening than the latter, which is the result of a more efficient QTM for Dy/gr/Cu at $B = 2.7$ T. The opening of the Dy/gr/Pt(111) magnetisation loop is narrower than those of Dy/gr/Ir(111) and Dy/gr/Cu samples, even though Dy/gr/Pt(111) displays the same remanence as Dy/gr/Cu, as the consequence of a steeper slope of the Dy/gr/Pt(111) magnetisation curve around $B = 0$ T. The quantitative estimation of the hysteresis loop opening area is also provided in fig. 5.4.

The Dy/gr_{BL}/Cu hysteresis loop is very similar to that of Dy/gr/Cu: both magnetisation curves exhibit two pairs of steps with identical positions and heights. Nonetheless, we remark two peculiar deviations. The first difference is found at low magnetic fields, in the region of ± 1 T, where the Dy/gr_{BL}/Cu opening gets narrower. Thus, addition of the graphene second layer prompts the butterfly shape of the Dy hysteresis loop. The second difference can be observed in the region between the two QTM steps (from 2.7 T to 5.6 T), where bilayer sample exhibits a slightly wider opening of the magnetisation curve.

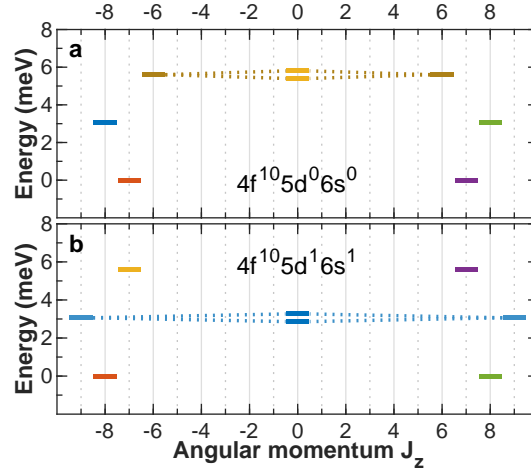


Figure 5.5 – The zero field splitting of the lowest states of Dy atoms with (a) empty [81] and (b) partially filled external subshells. The splitting of the mixed doublets is emphasized for better clarity. Each colour identifies magnetic quantum states belonging to one of the six classes defined by the C_{6v} group symmetry; dashed lines connect doublets with quenched J_z .

5.4 CF level splitting and external subshell occupation

The properties of Dy adatoms, namely X-ray absorption multiplet structure, magnetic anisotropy and positions of the QTM steps in the magnetisation loops, are defined by the zero-field splitting of the lowest J -multiplet, which, in turn, depends on the CF imposed by the supporting substrate. Since these properties are very similar for the Dy atoms adsorbed on all four studied substrates, we conclude that the adatoms are subject to the same CF, meaning that the CF is mainly defined by the graphene layer. First-principle calculations performed for Dy atoms adsorbed on gr/Ir(111) [90] and gr/Cu(111) [89] predict a Dy $4f^{10}$ electronic configuration and very similar adsorption height of the adatoms above the graphene layers for both substrates, confirming our conclusions. The CF and the corresponding energy level diagram (fig. 5.5a) suggested in ref. [81] not only reproduce the X-ray spectra via multiplet calculations, but also allow to explain the level crossings responsible for the steps in the magnetisation curves. The first pair of steps at $B = \pm 2.7$ T in the magnetisation curves correspond to the $J_z = \pm 7 \leftrightarrow J_z = \mp 8$ level crossings. These states are not coupled in C_{6v} symmetry, however, avoided level crossings can be explained by a small C_{3v} term in the CF caused by the inequivalence of the A-B carbon sublattices [195]. The second pair of steps ($B = \pm 5.6$ T) occurs at the crossing of the ground doublet with the second excited doublet ($J_z = \pm 7 \leftrightarrow J_z = \mp 6$), where QTM is mediated by first order electron or phonon scattering. Thus, the positions of the steps unambiguously define the energies of the first two excited doublets for all samples. Only Dy/gr/Pt(111) exhibits no second pair of steps, thereby, the position of its second excited doublet cannot be determined from our experiment.

Based on the energy scheme shown in fig. 5.5a, spin relaxation at $B = 0$ T takes place via electron or phonon assisted QTM through mixed $J_z = \pm 6$ states. However, a partial spin polari-

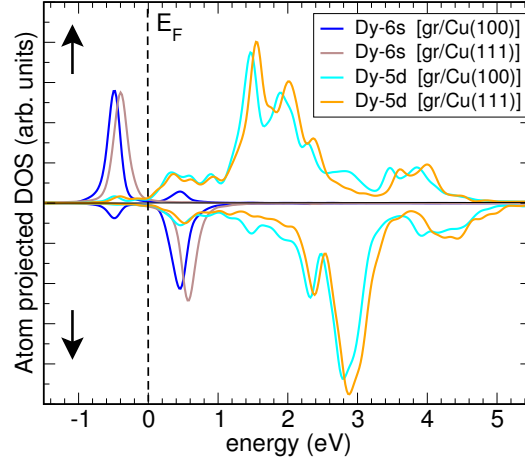


Figure 5.6 – Spin resolved DOS of 5d and 6s electrons of Dy adatoms on gr/Cu(100) and gr/Cu(111).

sation of the 5d subshell was found in ref. [89, 90], while ref. [196] and our DFT calculations demonstrate a spin polarisation for both 5d and 6s orbitals for Dy/gr/Ir(111), Dy/gr/Cu(111) and Dy/gr/Cu(100) (fig. 5.6). In this case the magnetic moment of the external subshells must be taken into account in the determination of the quantum states affected by QTM [196]. The DFT calculations predict a fractional occupation of the external subshells. Nevertheless, for simplicity and to properly construct the Hilbert space, we assume a spin $\frac{1}{2}$ magnetic moment for each external subshell. The spins of the external subshells are ferromagnetically coupled to the 4f spin, forming a single total atomic spin. For the $4f^{10}5d^16s^1$ configuration we obtain that the magnetic state of the Dy atom is described by the total atomic angular momentum $J^{tot} = J^{4f} + S^{6s5d}$ where we have approximated the total angular momentum of the 5d and 6s subshells by the spin momentum only, since the orbital momentum of these subshells is either zero (6s) or strongly quenched (5d) due to the hybridization with the surrounding atoms. Each state is then represented by a new basis $|J_z^{4f}, S_z^{5d}, S_z^{6s}\rangle$ with the C_{6v} symmetric CF coupling states, whose ΔJ_z is a multiple of 6 (fig. 5.5b). Within this picture the Dy spin relaxation at zero field is going through the first excited doublet, while the magnetic fields at which the level crossings take place and, consequently, the positions of the steps in the magnetisation curves are not affected. On the other hand, an addition of only one electron to the external subshells (5d or 6s) results in absence of mixing between the states of the 3 lowest doublets by the C_{6v} CF. Unfortunately, Dy $M_{4,5}$ X-ray absorption spectra are not sensitive to the external subshell occupation. For example, the multiplet calculations performed with the additional $6s^1$ open subshell differ from the $6s^2$ or $6s^0$ simulations by less than 5%. Moreover, while the majority (56.2% of natural abundance) of the Dy atoms show no nuclear spin ($I = 0$), the rest of the isotopes have a nuclear spin $I = \frac{5}{2}$, which should be added to the total atomic angular momentum. This further increases the number of feasible QTMs between the lowest energy states. Nonetheless, most of these QTMs require an assistance from the substrate electrons or phonons. Therefore, in the next section we describe the influence of the substrate electron and phonon density of states (DOS) on the Dy magnetic relaxation.

5.5 Substrate electron- and phonon-assisted spin relaxation

Free-standing graphene is known for its linear band dispersion with a vanishing electron DOS at the Fermi level. Nonetheless, the interaction with the supporting metal substrate shifts the graphene Dirac point with respect to the Fermi energy [182, 183]. The further the Dirac point is from the Fermi energy, the higher the graphene electron DOS is at the Fermi level. For gr/Ir(111) and gr/Pt(111) substrates the Dirac points were found to be 0.1 eV [184, 185] and 0.3 eV [186] above the Fermi energy respectively, while gr/Cu exhibits the Dirac point 0.3 eV below the Fermi level [180, 187, 192]. Hence, one can expect a higher DOS at the Fermi level and, consequently, a higher probability of spin-electron scattering for Dy/gr/Pt(111) and Dy/gr/Cu in comparison to Dy/gr/Ir(111). We also note that Dy adatoms transfer part of their electron charge to the graphene, which leads to a shift of the Fermi level [197]. Nevertheless, this shift is small (< -50 meV for 0.01 ML of Dy) and, thereby, we neglect it. The spin-electron scattering cannot explain the difference between the Dy/gr/Pt(111) and Dy/gr/Cu magnetisation loops. Theoretically, graphene vibrational modes can also induce the Dy demagnetisation. However, there exists no significant distinction between the phonon DOS of a graphene layer on Ir(111) and Cu substrates [198–200]. Moreover, all three metals exhibit identical absorption coefficient (Ir and Pt $6.2 \mu\text{m}^{-1}$, Cu $5.9 \mu\text{m}^{-1}$ [147]), therefore, the X-ray induced demagnetisation cannot rationalise the observed difference in the magnetisation loop openings. The speed of sound is lower in Pt (2680 m/s) than in Cu (3570 m/s), while Ir is the stiffest among the studied metallic substrates (4800 m/s) [174]. The sound velocity of the material is inversely proportional to the acoustic phonon DOS in the low energy region (0-5 meV). Thus, the experimentally observed openings of the hysteresis loops correlate well with the phonon DOS of the metallic substrates. The graphene electrons may also participate in the Dy spin relaxation, but their contribution seems to be much less than that of metallic substrate phonons.

Addition of the second graphene layer enhances the decoupling of Dy adatoms from the electrons and phonons of the underlying metal, since graphene is known to be an exceptionally

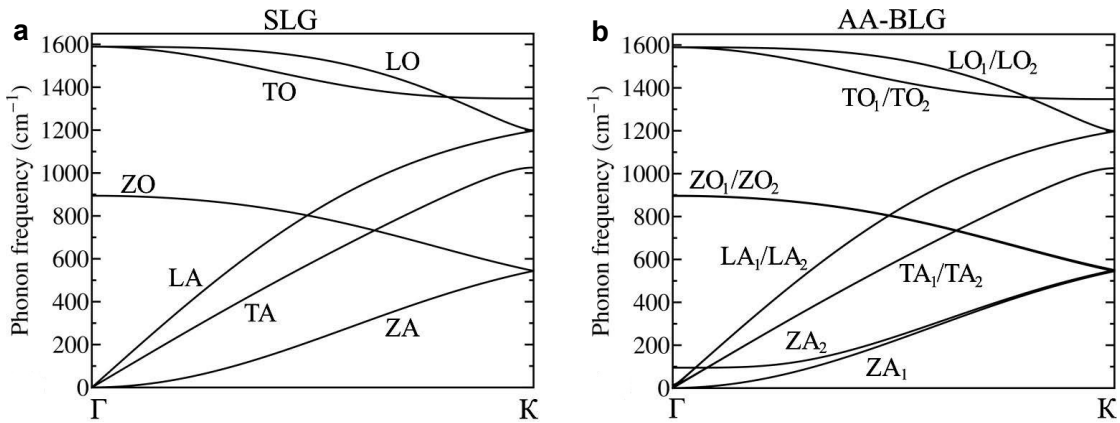


Figure 5.7 – Phonon energy dispersions in (a) single layer graphene (SLG) and (b) AA-stacked bilayer graphene (AA-BLG) reproduced from the ref. [201].

stiff semimetal [202]. This explains the slightly bigger opening of the Dy/gr_BL/Cu hysteresis loop between 2.7 T and 5.6 T. On the other hand, the interaction between graphene layers leads to the out-of-plane ZA phononic mode splitting (fig. 5.7), which depends on the relative orientation of the graphene sheets [201, 203–205]. Since our transferred second graphene layer had a size of several squared millimetres, domains with different orientations of the stacked graphene are unavoidable. Hence, our gr_BL/Cu substrate should show a broad increase in phonon DOS below 10 meV, which, in turn, leads to a reduction of the Dy spin lifetime at low magnetic fields.

5.6 Conclusion and outlook

The single-atom magnet behaviour of Dy adatoms on gr/Pt(111), gr/Cu and gr_BL/Cu substrates has been investigated and compared to Dy/gr/Ir(111). XAS spectra together with the positions of QTM steps in the magnetisation curves revealed an identical CF splitting of the lowest magnetic ground states for all of the substrates. We attributed the observed dissimilarities in the hysteresis loops to the differences in the metallic substrate phonon DOS. In addition, the correlation between the graphene Fermi level position and the Dy magnetisation curve opening cannot be excluded. Such correlation would open a viable path for the external electric field control of the Dy adatoms magnetic lifetime, since graphene is known to exhibit prominent field effect [179]. Furthermore, we showed that the approach consisting in the increase of the decoupling layer thickness does not always work well. The bilayer graphene substrate demonstrated that the insulating buffer layer vibrational modes can be as detrimental to the single-atom magnet stability as the metal conduction electrons.

Conclusions and Outlook

Five new SAMs are demonstrated in this thesis: Dy/BaO/Pt(100), Dy/ZnO/Au(111), Dy/ZnO/STO(110), Dy/gr/Pt(111) and Dy/gr_{BL}/Cu. While Dy/gr/Cu was studied previously [122], the quality of the data did not allow to unambiguously judge about the presence or absence of the magnetic remanence in that sample. Our data unequivocally corroborate the existence of such magnetic remanence.

Together with the previously reported SAMs (Ho/MgO/Ag(100) [49, 83, 87], Dy/gr/Ir(111) [81], Dy/MgO/Ag(100) [46, 82]), the systems presented in this work can be divided into two groups based on the CF at the adatom position. In the first group the CF is mainly defined by one or two closest-neighbour atoms, which should result in a perfectly axial symmetry. All the other RE neighbours only reduce the symmetry of the CF, and, thus, the interaction with them should be minimised. Such SAMs as Ho and Dy adsorbed at top-O site of MgO, and Dy adsorbed at top-O site of BaO constitute this group. All of them exhibit an out-of-plane magnetic anisotropy. Moreover, our multiplet calculations showed that Dy single atoms adsorbed at BaO bridge site should exhibit a prominent magnetic stability. They also can be added to the first type of SAMs. This demonstrates that atomic magnetic moment can be stabilised not only out of plane but also in plane. Furthermore, as we have shown, such approach works well for the ionic systems, whereas the covalency of the RE-substrate atom bond can reduce the symmetry of the CF. Dy/ZnO SAMs most likely belong to the first group.

The second type of SAMs rely on the CF created by a set of n substrate atoms located at the same distance from the RE adatom, so as to form a C_{nv} symmetric CF. If n is large enough, such approach does not completely eliminates the level mixing, but significantly reduces the number of states affected by QTM. All SAMs supported by graphene belong to this group. In ideal case, the CF order of symmetry n should be larger than the number of states $2J + 1$ in the lowest J-multiplet, since this would eliminate the QTM completely. Unfortunately, it is very hard to find a physical object that would create a CF with $n > 6$, while the reduction of the atomic angular momentum J can lower the MAB and, consequently, facilitate the thermally activated spin relaxation. This approach has been successfully used to construct SIMs [67, 69, 70].

We have demonstrated the correlation between the RE adatom magnetic stability and substrate phonon DOS for both types of SAMs. Regardless of the CF symmetry and the height of the

Conclusions and Outlook

MAB, the phonons remain one of the main channels for the adatom spin relaxation. The study of the impact of the substrate conduction electrons on the SAM stability is more complicated. We corroborated the influence of the X-ray photon induced secondary electrons on the RE magnetic lifetime. This effect can significantly reduce the spin lifetime measured in the XMCD experiment and, thereby, obscure all other spin relaxation mechanisms, including the scattering of the substrate conduction electrons with the RE spins.

All the currently known SAMs are based on Dy or Ho, even though other lanthanides were used in SIMs (for example, Tb [71, 77]). In this work we did not managed to add new chemical elements to this list. Only Dy exhibit the SAM behaviour with both types of CF, while Ho single atoms are only magnetically stable at the top-O adsorption site of MgO [83, 206].

The electric field control of adatom magnetic stability should be a next notable step towards SAMs based information storage. These experiments were shown to be rather difficult, especially with the TEY detection scheme. In an ideal experimental setup one should apply the homogeneous external electric field to the substrate without perturbing the surface adsorbed single atoms and blocking the X-ray radiation. Moreover, the TEY current is very sensitive to the substrate potential. Therefore, the artifacts due to the electric field perturbations of the TEY detection mode must be separated from the genuine XAS signal. In spite of these difficulties, we managed to perform XMCD measurements with the applied external electric field. The first promising results have been achieved, which should be corroborated by further investigations.

A Bader charges and atom coordinates for RE/BaO and RE/MgO

A.1 DFT calculations

In the following, the information of the first three coordination shell atoms around the RE adatoms necessary for the multiplet calculations is given for Dy/BaO top-O (table A.1), Dy/BaO bridge (table A.2), Ho/BaO top-O (table A.3) and Ho/BaO bridge (table A.4) sites, and for Dy/MgO top-O (table A.5), Dy/MgO bridge (table A.6), Ho/MgO top-O (table A.7) and Ho/MgO bridge (table A.8). We list for each atom the distance to the RE adatom, the Bader charge [207] and the atomic coordinates (the RE atom is the origin of the Cartesian system).

Table A.1 – Distance from the RE adatom, Bader charges and atomic coordinates for the atoms composing the first three coordination shells around the RE, for Dy adatom on top-O adsorption site on BaO.

Atom	Shell	Distance (in Å)	Bader Charge (in e^-)	Cartesian Coordinates		
				x (Å)	y (Å)	z (Å)
Dy	-	-	+0.20	0.000	0.000	0.000
O	1st	2.077	-1.36	0.000	0.000	-2.077
Ba	2nd	3.900	+1.36	0.000	2.907	-2.601
				2.907	0.000	-2.601
				0.000	-2.907	-2.601
				-2.907	0.000	-2.601
O	3rd	4.832	-1.38	2.783	2.783	-2.804
				2.783	-2.783	-2.804
				-2.783	2.783	-2.804
				-2.783	-2.783	-2.804

Appendix A. Bader charges and atom coordinates for RE/BaO and RE/MgO

Table A.2 – Distance from the RE adatom, Bader charges and atomic coordinates for the atoms composing the first three coordination shells around the RE, for Dy adatom on bridge adsorption site on BaO.

Atom	Shell	Distance (in Å)	Bader Charge (in e^-)	Cartesian Coordinates		
				x (Å)	y (Å)	z (Å)
Dy	-	-	+0.57	0.000	0.000	0.000
O	1st	2.148	-1.39	-1.100	-1.100	-1.481
				1.100	1.100	-1.481
Ba	2nd	3.209	+1.30	-1.675	1.675	-2.165
				1.675	-1.675	-2.165
Ba	3rd	4.798	+1.40	-1.369	-4.193	-1.888
				-4.193	-1.369	-1.888
				4.193	1.369	-1.888
				1.369	4.193	-1.888

Table A.3 – Distance from the RE adatom, Bader charges and atomic coordinates for the atoms composing the first three coordination shells around the RE, for Ho adatom on top-O adsorption site on BaO.

Atom	Shell	Distance (in Å)	Bader Charge (in e^-)	Cartesian Coordinates		
				x (Å)	y (Å)	z (Å)
Ho	-	-	+0.14	0.000	0.000	0.000
O	1st	2.085	-1.34	0.000	0.000	-2.085
Ba	2nd	3.884	+1.36	0.000	2.899	-2.585
				2.899	0.000	-2.585
				0.000	-2.899	-2.585
				-2.899	0.000	-2.585
O	3rd	4.822	-1.38	2.782	2.782	-2.787
				2.782	-2.782	-2.787
				-2.782	2.782	-2.787
				-2.782	-2.782	-2.787

Table A.4 – Distance from the RE adatom, Bader charges and atomic coordinates for the atoms composing the first three coordination shells around the RE, for Ho adatom on bridge adsorption site on BaO.

Atom	Shell	Distance (in Å)	Bader Charge (in e^-)	Cartesian Coordinates		
				x (Å)	y (Å)	z (Å)
Ho	-	-	+0.62	0.000	0.000	0.000
O	1st	2.168	-1.38	-1.099	-1.099	-1.511
				1.099	1.099	-1.511
Ba	2nd	3.191	+1.30	-1.672	1.672	-2.142
				1.672	-1.672	-2.142
Ba	3rd	4.781	1.39	-1.363	-4.184	-1.868
				-4.184	-1.363	-1.868
				4.184	1.363	-1.868
				1.363	4.184	-1.868

Table A.5 – Distance from the RE adatom, Bader charges and atomic coordinates for the atoms composing the first three coordination shells around the RE, for Dy adatom on top-O adsorption site on MgO.

Atom	Shell	Distance (in Å)	Bader Charge (in e^-)	Cartesian Coordinates		
				x (Å)	y (Å)	z (Å)
Dy	-	-	+0.20	0.000	0.000	0.000
O	1st	2.274	-1.69	0.000	0.000	-2.274
Mg	2nd	3.407	+1.68	0.000	2.172	-2.625
				2.172	0.000	-2.625
				0.000	-2.172	-2.625
				-2.172	0.000	-2.625
O	3rd	3.964	-1.72	2.106	2.106	-2.616
				2.106	-2.106	-2.616
				-2.106	2.106	-2.616
				-2.106	-2.106	-2.616

Appendix A. Bader charges and atom coordinates for RE/BaO and RE/MgO

Table A.6 – Distance from the RE adatom, Bader charges and atomic coordinates for the atoms composing the first three coordination shells around the RE, for Dy adatom on bridge adsorption site on MgO.

Atom	Shell	Distance (in Å)	Bader Charge (in e^-)	Cartesian Coordinates		
				x (Å)	y (Å)	z (Å)
Dy	-	-	+0.24	0.000	0.000	0.000
O	1st	2.603	-1.72	-1.004	-1.004	-2.182
				1.004	1.004	-2.182
Mg	2nd	2.985	+1.66	-1.133	1.133	-2.518
				1.133	-1.133	-2.518
Mg	3rd	4.105	+1.70	-1.042	-3.159	-2.406
				-3.159	-1.042	-2.406
				3.159	1.042	-2.406
				1.042	3.159	-2.406

Table A.7 – Distance from the RE adatom, Bader charges and atomic coordinates for the atoms composing the first three coordination shells around the RE, for Ho adatom on top-O adsorption site on MgO.

Atom	Shell	Distance (in Å)	Bader Charge (in e^-)	Cartesian Coordinates		
				x (Å)	y (Å)	z (Å)
Ho	-	-	+0.11	0.000	0.000	0.000
O	1st	2.258	-1.66	0.000	0.000	-2.258
Mg	2nd	3.380	1.68	0.000	2.174	-2.588
				2.174	0.000	-2.588
				0.000	-2.174	-2.588
				-2.174	0.000	-2.588
O	3rd	3.931	-1.71	2.105	2.105	-2.568
				2.105	-2.105	-2.568
				-2.105	2.105	-2.568
				-2.105	-2.105	-2.568

A.2. CF point charges used in the multiplet calculations

Table A.8 – Distance from the RE adatom, Bader charges and atomic coordinates for the atoms composing the first three coordination shells around the RE, for Ho adatom on bridge adsorption site on MgO.

Atom	Shell	Distance (in Å)	Bader Charge (in e^-)	Cartesian Coordinates		
				x (Å)	y (Å)	z (Å)
Ho	-	-	+0.15	0.000	0.000	0.000
O	1st	2.666	-1.71	-1.012	-1.012	-2.249
				1.012	1.012	-2.249
Mg	2nd	3.006	1.67	-1.122	1.122	-2.553
				1.122	-1.122	-2.553
Mg	3rd	4.138	1.70	-1.048	-3.164	-2.453
				-3.164	-1.048	-2.453
				3.164	1.048	-2.453
				1.048	3.164	-2.453

A.2 CF point charges used in the multiplet calculations

The point charges used in the multiplet simulations of Dy and Ho adatoms on BaO/Pt(100) are given in table A.9. They were deduced from table A.1 and table A.2 as described in section 3.2.

Table A.9 – Point charges used to simulate the CF for RE adatoms (Ln is Dy or Ho) at different absorption sites (top-O, br-xz and br-yz) on BaO in multiplet simulations.

Ln^{top}			
$x, \text{Å}$	$y, \text{Å}$	$z, \text{Å}$	q, e^-
0.000	0.000	-1.540	-0.0626
0.000	2.907	-2.600	1.360
0.000	-2.907	-2.600	1.360
2.907	0.000	-2.600	1.360
-2.907	0.000	-2.600	1.360

Ln^{br-xz}				Ln^{br-yz}			
$x, \text{Å}$	$y, \text{Å}$	$z, \text{Å}$	q, e	$x, \text{Å}$	$y, \text{Å}$	$z, \text{Å}$	q, e
1.150	0.000	-1.100	-0.0626	0.000	1.150	-1.100	-0.0626
-1.150	0.000	-1.100	-0.0626	0.000	-1.150	-1.100	-0.0626
0.000	2.370	-2.170	1.300	2.370	0.000	-2.170	1.300
0.000	-2.370	-2.170	1.300	-2.370	0.000	-2.170	1.300

Bibliography

- [1] Rutherford, E. LVII. The structure of the atom. *Lond. Edinb. Dublin philos. mag. j. sci.* **27**, 488–498 (1914).
- [2] Van Noorden, R. Four chemical elements added to periodic table. *Nature* (2016).
- [3] Gerlach, W. & Stern, O. Der experimentelle Nachweis der Richtungsquantelung im Magnetfeld. *Z. Phys.* **9**, 349–352 (1922).
- [4] Rabi, I. I., Zacharias, J. R., Millman, S. & Kusch, P. A New Method of Measuring Nuclear Magnetic Moment. *Phys. Rev.* **53**, 318–318 (1938).
- [5] Paul, W. & Steinwedel, H. Ein neues Massenspektrometer ohne Magnetfeld. *Z. Naturforsch. A* **8**, 448–450 (1953).
- [6] Blaum, K. High-accuracy mass spectrometry with stored ions. *Phys. Rep.* **425**, 1–78 (2006).
- [7] Raab, E. L., Prentiss, M., Cable, A., Chu, S. & Pritchard, D. E. Trapping of Neutral Sodium Atoms with Radiation Pressure. *Phys. Rev. Lett.* **59**, 2631–2634 (1987).
- [8] Cirac, J. I. & Zoller, P. Quantum Computations with Cold Trapped Ions. *Phys. Rev. Lett.* **74**, 4091–4094 (1995).
- [9] Endres, M. *et al.* Atom-by-atom assembly of defect-free one-dimensional cold atom arrays. *Science* **354**, 1024–1027 (2016).
- [10] Nelson, K. D., Li, X. & Weiss, D. S. Imaging single atoms in a three-dimensional array. *Nat. Phys.* **3**, 556–560 (2007).
- [11] Pogorelov, I. *et al.* Compact Ion-Trap Quantum Computing Demonstrator. *PRX Quantum* **2**, 020343 (2021).
- [12] Binnig, G., Rohrer, H., Gerber, C. & Weibel, E. Surface Studies by Scanning Tunneling Microscopy. *Phys. Rev. Lett.* **49**, 57–61 (1982).
- [13] Binnig, G., Quate, C. F. & Gerber, C. Atomic Force Microscope. *Phys. Rev. Lett.* **56**, 930–933 (1986).

Bibliography

- [14] Haider, M. *et al.* Electron microscopy image enhanced. *Nature* **392**, 768–769 (1998).
- [15] Eigler, D. M. & Schweizer, E. K. Positioning single atoms with a scanning tunnelling microscope. *Nature* **344**, 524–526 (1990).
- [16] Kawai, S. *et al.* Atom manipulation on an insulating surface at room temperature. *Nat. Commun.* **5**, 4403 (2014).
- [17] Su, C. *et al.* Engineering single-atom dynamics with electron irradiation. *Sci. Adv.* **5**, eaav2252 (2019).
- [18] Carra, P., Thole, B. T., Altarelli, M. & Wang, X. X-ray circular dichroism and local magnetic fields. *Phys. Rev. Lett.* **70**, 694–697 (1993).
- [19] Thole, B. T., Carra, P., Sette, F. & van der Laan, G. X-ray circular dichroism as a probe of orbital magnetization. *Phys. Rev. Lett.* **68**, 1943–1946 (1992).
- [20] Brune, H. & Gambardella, P. Magnetism of individual atoms adsorbed on surfaces. *Surf. Sci.* **603**, 1812–1830 (2009).
- [21] Choi, T. Studies of single atom magnets via scanning tunneling microscopy. *J. Magn. Magn. Mater.* **481**, 150–155 (2019).
- [22] Donati, F. & Heinrich, A. J. A perspective on surface-adsorbed single atom magnets as atomic-scale magnetic memory. *Appl. Phys. Lett.* **119**, 160503 (2021).
- [23] Kaiser, S. K., Chen, Z., Faust Akl, D., Mitchell, S. & Pérez-Ramírez, J. Single-Atom Catalysts across the Periodic Table. *Chem. Rev.* **120**, 11703–11809 (2020).
- [24] Wang, A., Li, J. & Zhang, T. Heterogeneous single-atom catalysis. *Nat. Rev. Chem.* **2**, 65–81 (2018).
- [25] Jamneala, T., Madhavan, V. & Crommie, M. Kondo Response of a Single Antiferromagnetic Chromium Trimer. *Phys. Rev. Lett.* **87**, 256804 (2001).
- [26] Khajetoorians, A. A. *et al.* Current-Driven Spin Dynamics of Artificially Constructed Quantum Magnets. *Science* **339**, 55–59 (2013).
- [27] Loth, S., Etzkorn, M., Lutz, C. P., Eigler, D. M. & Heinrich, A. J. Measurement of Fast Electron Spin Relaxation Times with Atomic Resolution. *Science* **329**, 1628–1630 (2010).
- [28] Singha, A. *et al.* Spin Excitations in a $4f$ - $3d$ Heterodimer on MgO. *Phys. Rev. Lett.* **121**, 257202 (2018).
- [29] Zhou, L. *et al.* Strength and directionality of surface Ruderman–Kittel–Kasuya–Yosida interaction mapped on the atomic scale. *Nat. Phys.* **6**, 187–191 (2010).
- [30] Singha, A. *et al.* Magnetic Hysteresis in Er Trimers on Cu(111). *Nano Lett.* **16**, 3475–3481 (2016).

-
- [31] Gambardella, P. *et al.* Ferromagnetism in one-dimensional monatomic metal chains. *Nature* **416**, 301–304 (2002).
- [32] Hirjibehedin, C. F., Lutz, C. P. & Heinrich, A. J. Spin Coupling in Engineered Atomic Structures. *Science* **312**, 1021–1024 (2006).
- [33] Loth, S., Baumann, S., Lutz, C. P., Eigler, D. M. & Heinrich, A. J. Bistability in Atomic-Scale Antiferromagnets. *Science* **335**, 196–199 (2012).
- [34] Spinelli, A., Bryant, B., Delgado, F., Fernández-Rossier, J. & Otte, A. F. Imaging of spin waves in atomically designed nanomagnets. *Nat. Mater.* **13**, 782–785 (2014).
- [35] Toskovic, R. *et al.* Atomic spin-chain realization of a model for quantum criticality. *Nat. Phys.* **12**, 656–660 (2016).
- [36] Yan, S., Choi, D.-J., Burgess, J. A. J., Rolf-Pissarczyk, S. & Loth, S. Control of quantum magnets by atomic exchange bias. *Nat. Nanotechnol.* **10**, 40–45 (2015).
- [37] Khajetoorians, A. A. *et al.* Atom-by-atom engineering and magnetometry of tailored nanomagnets. *Nat. Phys.* **8**, 497–503 (2012).
- [38] Meier, F., Zhou, L., Wiebe, J. & Wiesendanger, R. Revealing Magnetic Interactions from Single-Atom Magnetization Curves. *Science* **320**, 82–86 (2008).
- [39] Wahl, P. *et al.* Exchange Interaction between Single Magnetic Adatoms. *Phys. Rev. Lett.* **98**, 056601 (2007).
- [40] Loth, S. *et al.* Controlling the state of quantum spins with electric currents. *Nat. Phys.* **6**, 340–344 (2010).
- [41] Khajetoorians, A. A., Wiebe, J., Chilian, B. & Wiesendanger, R. Realizing All-Spin-Based Logic Operations Atom by Atom. *Science* **332**, 1062–1064 (2011).
- [42] Baumann, S. *et al.* Electron paramagnetic resonance of individual atoms on a surface. *Science* **350**, 417–420 (2015).
- [43] Seifert, T. S. *et al.* Single-atom electron paramagnetic resonance in a scanning tunneling microscope driven by a radio-frequency antenna at 4 K. *Phys. Rev. Res.* **2**, 013032 (2020).
- [44] Choi, T. *et al.* Atomic-scale sensing of the magnetic dipolar field from single atoms. *Nat. Nanotechnol.* **12**, 420–424 (2017).
- [45] Choi, T., Lutz, C. P. & Heinrich, A. J. Studies of magnetic dipolar interaction between individual atoms using ESR-STM. *Curr. Appl. Phys.* **17**, 1513–1517 (2017).
- [46] Singha, A. *et al.* Engineering atomic-scale magnetic fields by dysprosium single atom magnets. *Nat. Commun.* **12**, 4179 (2021).

Bibliography

- [47] Yang, K. *et al.* Engineering the Eigenstates of Coupled Spin- 1/2 Atoms on a Surface. *Phys. Rev. Lett.* **119**, 227206 (2017).
- [48] Yang, K. *et al.* Tuning the Exchange Bias on a Single Atom from 1 mT to 10 T. *Phys. Rev. Lett.* **122**, 227203 (2019).
- [49] Natterer, F. D. *et al.* Reading and writing single-atom magnets. *Nature* **543**, 226–228 (2017).
- [50] Bae, Y. *et al.* Enhanced quantum coherence in exchange coupled spins via singlet-triplet transitions. *Sci. Adv.* **4**, eaau4159 (2018).
- [51] Willke, P. *et al.* Probing quantum coherence in single-atom electron spin resonance. *Sci. Adv.* **4**, eaaq1543 (2018).
- [52] Yang, K. *et al.* Coherent spin manipulation of individual atoms on a surface. *Science* **366**, 509–512 (2019).
- [53] Willke, P. *et al.* Hyperfine interaction of individual atoms on a surface. *Science* **362**, 336–339 (2018).
- [54] Yang, K. *et al.* Electrically controlled nuclear polarization of individual atoms. *Nat. Nanotechnol.* **13**, 1120–1125 (2018).
- [55] Yang, K. *et al.* Probing resonating valence bond states in artificial quantum magnets. *Nat. Commun.* **12**, 993 (2021).
- [56] Willke, P., Yang, K., Bae, Y., Heinrich, A. J. & Lutz, C. P. Magnetic resonance imaging of single atoms on a surface. *Nat. Phys.* (2019).
- [57] Gurevich, A. G. & Melkov, G. A. *Magnetization Oscillations and Waves* (CRC Press, Boca Raton, Florida, 1996).
- [58] Thompson, J. Flat Attraction. *Sci. Am.* **325**, 21 (2021).
- [59] Fert, A., Cros, V. & Sampaio, J. Skyrmions on the track. *Nat. Nanotechnol.* **8**, 152–156 (2013).
- [60] Koshibae, W. *et al.* Memory functions of magnetic skyrmions. *Jpn. J. Appl. Phys.* **54**, 053001 (2015).
- [61] Bar, A. K., Kalita, P., Singh, M. K., Rajaraman, G. & Chandrasekhar, V. Low-coordinate mononuclear lanthanide complexes as molecular nanomagnets. *Coord. Chem. Rev.* **367**, 163–216 (2018).
- [62] Chen, X. *et al.* Probing Superexchange Interaction in Molecular Magnets by Spin-Flip Spectroscopy and Microscopy. *Phys. Rev. Lett.* **101**, 197208 (2008).

- [63] Diller, K. *et al.* Magnetic properties of on-surface synthesized single-ion molecular magnets. *RSC Adv.* **9**, 34421–34429 (2019).
- [64] Dreiser, J. Molecular lanthanide single-ion magnets: From bulk to submonolayers. *J. Phys.: Condens. Matter* **27**, 183203 (2015).
- [65] Dreiser, J. *et al.* Out-of-Plane Alignment of Er(trensal) Easy Magnetization Axes Using Graphene. *ACS Nano* **10**, 2887–2892 (2016).
- [66] Dreiser, J. *et al.* X-ray induced demagnetization of single-molecule magnets. *Appl. Phys. Lett.* **105**, 032411 (2014).
- [67] Goodwin, C. A. P., Ortu, F., Reta, D., Chilton, N. F. & Mills, D. P. Molecular magnetic hysteresis at 60 kelvin in dysprosocenium. *Nature* **548**, 439–442 (2017).
- [68] Gould, C. A. *et al.* Synthesis and Magnetism of Neutral, Linear Metallocene Complexes of Terbium(II) and Dysprosium(II). *J. Am. Chem. Soc.* **141**, 12967–12973 (2019).
- [69] Guo, F.-S. *et al.* A Dysprosium Metallocene Single-Molecule Magnet Functioning at the Axial Limit. *Angew. Chem. Int. Ed.* **56**, 11445–11449 (2017).
- [70] Guo, F.-S. *et al.* Magnetic hysteresis up to 80 kelvin in a dysprosium metallocene single-molecule magnet. *Science* **362**, 1400–1403 (2018).
- [71] Ishikawa, N., Sugita, M., Ishikawa, T., Koshihara, S.-y. & Kaizu, Y. Lanthanide Double-Decker Complexes Functioning as Magnets at the Single-Molecular Level. *J. Am. Chem. Soc.* **125**, 8694–8695 (2003).
- [72] Lunghi, A., Totti, F., Sessoli, R. & Sanvito, S. The role of anharmonic phonons in under-barrier spin relaxation of single molecule magnets. *Nat. Commun.* **8**, 14620 (2017).
- [73] Pedersen, K. S. *et al.* Toward Molecular 4f Single-Ion Magnet Qubits. *J. Am. Chem. Soc.* **138**, 5801–5804 (2016).
- [74] Thiele, S. *et al.* Electrically driven nuclear spin resonance in single-molecule magnets. *Science* **344**, 1135–1138 (2014).
- [75] Ungur, L. & Chibotaru, L. F. Magnetic anisotropy in the excited states of low symmetry lanthanide complexes. *Phys. Chem. Chem. Phys.* **13**, 20086 (2011).
- [76] Ungur, L. & Chibotaru, L. F. Strategies toward High-Temperature Lanthanide-Based Single-Molecule Magnets. *Inorg. Chem.* **55**, 10043–10056 (2016).
- [77] Wäckerlin, C. *et al.* Giant Hysteresis of Single-Molecule Magnets Adsorbed on a Non-magnetic Insulator. *Adv. Mater.* **28**, 5195–5199 (2016).
- [78] Wang, X. *et al.* Ferroelectric control of single-molecule magnetism in 2D limit. *Sci. Bull.* **65**, 1252–1259 (2020).

Bibliography

- [79] Westerström, R. *et al.* An Endohedral Single-Molecule Magnet with Long Relaxation Times: DySc₂N@C₈₀. *J. Am. Chem. Soc.* **134**, 9840–9843 (2012).
- [80] Zhang, W., Muhtadi, A., Iwahara, N., Ungur, L. & Chibotaru, L. F. Magnetic Anisotropy in Divalent Lanthanide Compounds. *Angew. Chem. Int. Ed.* **59**, 12720–12724 (2020).
- [81] Baltic, R. *et al.* Superlattice of Single Atom Magnets on Graphene. *Nano Lett.* **16**, 7610–7615 (2016).
- [82] Donati, F. *et al.* Correlation between Electronic Configuration and Magnetic Stability in Dysprosium Single Atom Magnets. *Nano Lett.* **21**, 8266–8273 (2021).
- [83] Donati, F. *et al.* Magnetic remanence in single atoms. *Science* **352**, 318–321 (2016).
- [84] Donati, F. *et al.* Unconventional Spin Relaxation Involving Localized Vibrational Modes in Ho Single-Atom Magnets. *Phys. Rev. Lett.* **124**, 077204 (2020).
- [85] Forrester, P. R. *et al.* Quantum state manipulation of single atom magnets using the hyperfine interaction. *Phys. Rev. B* **100**, 180405 (2019).
- [86] Gambardella, P. *et al.* Giant Magnetic Anisotropy of Single Cobalt Atoms and Nanoparticles. *Science* **300**, 1130–1133 (2003).
- [87] Natterer, F. D., Donati, F., Patthey, F. & Brune, H. Thermal and Magnetic-Field Stability of Holmium Single-Atom Magnets. *Phys. Rev. Lett.* **121**, 027201 (2018).
- [88] Rau, I. G. *et al.* Reaching the magnetic anisotropy limit of a 3d metal atom. *Science* **344**, 988–992 (2014).
- [89] Shick, A. B., Kolorenč, J., Denisov, A. Y. & Shapiro, D. S. Magnetic anisotropy of a Dy atom on a graphene/Cu(111) surface. *Phys. Rev. B* **102**, 064402 (2020).
- [90] Shick, A. & Denisov, A. Magnetism of 4f-atoms adsorbed on metal and graphene substrates. *J. Magn. Magn. Mater.* **475**, 211–215 (2019).
- [91] Balashov, T. *et al.* Magnetic Anisotropy and Magnetization Dynamics of Individual Atoms and Clusters of Fe and Co on Pt(111). *Phys. Rev. Lett.* **102**, 257203 (2009).
- [92] Błoński, P. *et al.* Magnetocrystalline anisotropy energy of Co and Fe adatoms on the (111) surfaces of Pd and Rh. *Phys. Rev. B* **81**, 104426 (2010).
- [93] Donati, F. *et al.* Magnetic Moment and Anisotropy of Individual Co Atoms on Graphene. *Phys. Rev. Lett.* **111**, 236801 (2013).
- [94] Donati, F. *et al.* Tailoring the Magnetism of Co Atoms on Graphene through Substrate Hybridization. *Phys. Rev. Lett.* **113**, 177201 (2014).
- [95] Etzkorn, M. *et al.* Comparing XMCD and DFT with STM spin excitation spectroscopy for Fe and Co adatoms on Cu₂N/Cu(100). *Phys. Rev. B* **92**, 184406 (2015).

-
- [96] Heinrich, A. J., Gupta, J. A., Lutz, C. P. & Eigler, D. M. Single-Atom Spin-Flip Spectroscopy. *Science* **306**, 466–469 (2004).
- [97] Khajetoorians, A. A. *et al.* Itinerant Nature of Atom-Magnetization Excitation by Tunneling Electrons. *Phys. Rev. Lett.* **106**, 037205 (2011).
- [98] Khajetoorians, A. A. *et al.* Spin Excitations of Individual Fe Atoms on Pt(111): Impact of the Site-Dependent Giant Substrate Polarization. *Phys. Rev. Lett.* **111**, 157204 (2013).
- [99] Lehnert, A. *et al.* Magnetic anisotropy of Fe and Co adatoms and Fe clusters magnetically decoupled from Ni₃Al(111) by an alumina bilayer. *Phys. Rev. B* **81**, 104430 (2010).
- [100] Pacchioni, G. E. *et al.* Multiplet features and magnetic properties of Fe on Cu(111): From single atoms to small clusters. *Phys. Rev. B* **91**, 235426 (2015).
- [101] Hirjibehedin, C. F. *et al.* Large Magnetic Anisotropy of a Single Atomic Spin Embedded in a Surface Molecular Network. *Science* **317**, 1199–1203 (2007).
- [102] Paul, W. *et al.* Control of the millisecond spin lifetime of an electrically probed atom. *Nature Phys* **13**, 403–407 (2017).
- [103] Matsukura, E., Tokura, Y. & Ohno, H. Control of magnetism by electric fields. *Nat. Nanotechnol.* **10**, 209–220 (2015).
- [104] Uldry, A., Vernay, F. & Delley, B. Systematic computation of crystal-field multiplets for X-ray core spectroscopies. *Phys. Rev. B* **85**, 125133 (2012).
- [105] Dirac, P. A. M. *The Principles of Quantum Mechanics* (Oxford University Press, Oxford, U.K., 1930).
- [106] Shanavas, K. V., Popović, Z. S. & Satpathy, S. Theoretical model for Rashba spin-orbit interaction in d electrons. *Phys. Rev. B* **90**, 165108 (2014).
- [107] Russell, H. N. & Saunders, F. A. New Regularities in the Spectra of the Alkaline Earths. *Astrophys. J.* **61**, 38 (1925).
- [108] Tiesinga, E., Mohr, P. J., Newell, D. B. & Taylor, B. N. CODATA recommended values of the fundamental physical constants: 2018. *Rev. Mod. Phys.* **93**, 025010 (2021).
- [109] Landé, A. über den anomalen Zeemaneffekt. *Z. Phys.* **5**, 231 (1921).
- [110] Hund, F. Atomtheoretische Deutung des Magnetismus der seltenen. Erden. *Z. Phys.* **33**, 855–859 (1925).
- [111] Abragam, A. & Bleaney, B. *Electron Paramagnetic Resonance of Transition Ions* (Oxford University Press, Oxford, U.K., 1970).
- [112] Griffiths, D. J. *Introduction to Quantum Mechanics* (Pearson Education UK, Harlow, 2013).

Bibliography

- [113] Zeeman, P. VII. Doublets and triplets in the spectrum produced by external magnetic forces. *Lond. Edinb. Dublin philos. mag. j. sci.* **44**, 55–60 (1897).
- [114] Bethe, H. Termaufspaltung in Kristallen. *Ann. Phys.* **395**, 133–208 (1929).
- [115] Rudowicz, C. & Chung, C. Y. The generalization of the extended Stevens operators to higher ranks and spins, and a systematic review of the tables of the tensor operators and their matrix elements. *J. Phys.: Condens. Matter* **16**, 5825–5847 (2004).
- [116] Stevens, K. W. H. Matrix Elements and Operator Equivalents Connected with the Magnetic Properties of Rare Earth Ions. *Proc. Phys. Soc. A* **65**, 209–215 (1952).
- [117] Altshuler, S. A. & Kozyrev, B. M. *Electron Paramagnetic Resonance in Compounds of Transition Elements* (John Wiley & Sons, New York NY, 1974), second edn.
- [118] Thomas, L. *et al.* Macroscopic quantum tunnelling of magnetization in a single crystal of nanomagnets. *Nature* **383**, 145–147 (1996).
- [119] Kramers, H. A. Théorie générale de la rotation paramagnétique dans les cristaux. *Proc. R. Acad. Sci. Amsterdam* **33**, 959 (1930).
- [120] Goedkoop, J. B. *et al.* Calculations of magnetic x-ray dichroism in the 3d absorption spectra of rare-earth compounds. *Phys. Rev. B* **37**, 2086–2093 (1988).
- [121] Thole, B. T. *et al.* 3d x-ray-absorption lines and the $3d^9 4f^{n+1}$ multiplets of the lanthanides. *Phys. Rev. B* **32**, 5107–5118 (1985).
- [122] Baltic, R. *Magnetic Stability of Single Lanthanide Atoms on Graphene*. Ph.D. thesis, EPFL, Lausanne (2018).
- [123] Carra, P., König, H., Thole, B. & Altarelli, M. Magnetic X-ray dichroism: General features of dipolar and quadrupolar spectra. *Phys. B: Condens. Matter* **192**, 182–190 (1993).
- [124] Teramura, Y., Tanaka, A., Thole, B. T. & Jo, T. Effect of Coulomb Interaction on the X-Ray Magnetic Circular Dichroism Spin Sum Rule in Rare Earths. *J. Phys. Soc. Jpn.* **65**, 3056–3059 (1996).
- [125] Cheong, S.-W., Fiebig, M., Wu, W., Chapon, L. & Kiryukhin, V. Seeing is believing: Visualization of antiferromagnetic domains. *npj Quantum Mater.* **5**, 3 (2020).
- [126] Mandal, S., Das, J. & Menon, K. S. Surface magnetism of NiO investigated by magnetic spectromicroscopies. *J. Electron Spectrosc. Relat. Phenom.* **208**, 51–55 (2016).
- [127] Rinehart, J. D. & Long, J. R. Exploiting single-ion anisotropy in the design of f-element single-molecule magnets. *Chem. Sci.* **2**, 2078 (2011).
- [128] van der Laan, G. Magnetic Linear X-Ray Dichroism as a Probe of the Magnetocrystalline Anisotropy. *Phys. Rev. Lett.* **82**, 640–643 (1999).

- [129] Röntgen, W. C. On a New Kind of Rays. *Nature* **53**, 274–276 (1896).
- [130] Margaritondo, G. A Primer in Synchrotron Radiation: Everything You Wanted to Know about SEX (Synchrotron Emission of X-rays) but Were Afraid to Ask. *J. Synchrotron Radiat.* **2**, 148–154 (1995).
- [131] Piamonteze, C. *et al.* X-Treme beamline at SLS: X-ray magnetic circular and linear dichroism at high field and low temperature. *J. Synchrotron Radiat.* **19**, 661–674 (2012).
- [132] Condon, E. U. & Shortley, G. H. *The Theory of Atomic Spectra* (Cambridge University Press, Cambridge, 1935).
- [133] Cowan, R. D. *The Theory of Atomic Structure and Spectra* (University of California Press, Berkeley, 1981).
- [134] de Groot, F. Multiplet effects in X-ray spectroscopy. *Coord. Chem. Rev.* **249**, 31–63 (2005).
- [135] Moreno-Pineda, E., Godfrin, C., Balestro, F., Wernsdorfer, W. & Ruben, M. Molecular spin qubits for quantum algorithms. *Chem. Soc. Rev.* **47**, 501–513 (2018).
- [136] Singha, A. *et al.* 4f occupancy and magnetism of rare-earth atoms adsorbed on metal substrates. *Phys. Rev. B* **96**, 224418 (2017).
- [137] Fernandes, E. *et al.* Adsorption sites of individual metal atoms on ultrathin MgO(100) films. *Phys. Rev. B* **96**, 045419 (2017).
- [138] Jorgensen, C. K., Pappalardo, R. & Schmidtke, H.-H. Do the “Ligand field” parameters in lanthanides represent weak covalent bonding? *J. Chem. Phys.* **39**, 1422–1430 (1963).
- [139] Watson, R. E. & Freeman, A. J. Covalent effects in rare-earth crystal-field splittings. *Phys. Rev.* **156**, 251–258 (1967).
- [140] Zolnierrek, Z. Crystal field parameters in a modified point charge model. *J. Phys. Chem. Solids* **45**, 523–528 (1984).
- [141] Porcher, P., Couto Dos Santos, M. & Malta, O. Relationship between phenomenological crystal field parameters and the crystal structure: The simple overlap model. *Phys. Chem. Chem. Phys.* **1**, 397–405 (1999).
- [142] Baldoví, J. J. *et al.* Rational design of single-ion magnets and spin qubits based on mononuclear lanthanoid complexes. *Inorg. Chem.* **51**, 12565–12574 (2012).
- [143] Jiang, S.-D. & Qin, S.-X. Prediction of the quantized axis of rare-earth ions: The electrostatic model with displaced point charges. *Inorg. Chem. Front.* **2**, 613–619 (2015).
- [144] Chang, S. S., Tompson, C. W., Gürmen, E. & Muhlestein, L. D. Lattice Dynamics of BaO. *J. Phys. Chem. Solids* **36**, 769–773 (1975).

Bibliography

- [145] Sangster, M. J. L., Peckham, G. & Saunderson, D. H. Lattice dynamics of magnesium oxide. *J. Phys. C: Solid State Phys.* **3**, 1026–1036 (1970).
- [146] Parlinski, K., Łażewski, J. & Kawazoe, Y. Ab initio studies of phonons in MgO by the direct method including LO mode. *J. Phys. Chem. Solids* **61**, 87–90 (2000).
- [147] Henke, B. L., Gullikson, E. M. & Davis, J. C. X-ray interactions: Photoabsorption, scattering, transmission, and reflection at E=50–30000 eV, Z=1–92. *At. Data Nucl. Data Tables* **54**, 181–342 (1993).
- [148] Blaha, P., Schwarz, K., Madsen, G. K. H., Kvasnicka, D. & Luitz, J. *WIEN2k, an Augmented Plane Wave + Local Orbitals Program for Calculating Crystal Properties*. (Karlheinz Schwarz, Techn. Universität Wien, Austria) (2001).
- [149] Perdew, J. P., Burke, K. & Ernzerhof, M. Generalized gradient approximation made simple. *Phys. Rev. Lett.* **77**, 3865–3868 (1996).
- [150] Tran, F., Blaha, P., Schwarz, K. & Novák, P. Hybrid exchange–correlation energy functionals for strongly correlated electrons: Applications to transition-metal monoxides. *Phys. Rev. B* **74**, 155108 (2006).
- [151] Lucaccini, E. *et al.* Relaxation dynamics and magnetic anisotropy in a low-symmetry DyIII complex. *Chem. Eur. J.* **22**, 5552–5562 (2016).
- [152] Gatteschi, D., Sessoli, R. & Villain, J. *Molecular Nanomagnets* (Oxford University Press, Oxford, 2006).
- [153] Fort, A., Rettori, A., Villain, J., Gatteschi, D. & Sessoli, R. Mixed Quantum-Thermal Relaxation in Mn 12 Acetate Molecules. *Phys. Rev. Lett.* **80**, 612–615 (1998).
- [154] Heilmann, P., Heinz, K. & Müller, K. The Superstructures of the Clean Pt(100) and Ir(100) Surfaces. *Surf. Sci.* **83**, 487–497 (1979).
- [155] Srikant, V. & Clarke, D. R. On the optical band gap of zinc oxide. *J. Appl. Phys.* **83**, 5447–5451 (1998).
- [156] Borysiewicz, M. A. ZnO as a Functional Material, a Review. *Crystals* **9**, 505 (2019).
- [157] Özgür, Ü. *et al.* A comprehensive review of ZnO materials and devices. *J. Appl. Phys.* **98**, 041301 (2005).
- [158] Liu, C., Yun, F. & Morkoç, H. Ferromagnetism of ZnO and GaN: A Review. *J. Mater. Sci.: Mater. Electron.* **16**, 555 (2005).
- [159] Zelenka, J. *Piezoelectric Resonators and Their Applications* (Elsevier, Amsterdam, 1986).
- [160] Shiotari, A. *et al.* Local Characterization of Ultrathin ZnO Layers on Ag(111) by Scanning Tunneling Microscopy and Atomic Force Microscopy. *J. Phys. Chem. C* **118**, 27428–27435 (2014).

- [161] Tusche, C., Meyerheim, H. L. & Kirschner, J. Observation of Depolarized ZnO(0001) Monolayers: Formation of Unreconstructed Planar Sheets. *Phys. Rev. Lett.* **99**, 026102 (2007).
- [162] Fidelis, I. *et al.* Electronic properties of ultrathin O-terminated ZnO (0001) on Au (111). *Surf. Sci.* **679**, 259–263 (2019).
- [163] Stavale, F., Pascua, L., Nilius, N. & Freund, H.-J. Luminescence Properties of Nitrogen-Doped ZnO. *J. Phys. Chem. C* **118**, 13693–13696 (2014).
- [164] Weirum, G. *et al.* Growth and Surface Structure of Zinc Oxide Layers on a Pd(111) Surface. *J. Phys. Chem. C* **114**, 15432–15439 (2010).
- [165] Liu, B.-H., McBriarty, M. E., Bedzyk, M. J., Shaikhutdinov, S. & Freund, H.-J. Structural Transformations of Zinc Oxide Layers on Pt(111). *J. Phys. Chem. C* **118**, 28725–28729 (2014).
- [166] Liu, B.-H., Groot, I. M., Pan, Q., Shaikhutdinov, S. & Freund, H.-J. Ultrathin Zn and ZnO films on Cu(111) as model catalysts. *Appl. Catal. A: Gen.* **548**, 16–23 (2017).
- [167] Liu, B.-H., Boscoboinik, J. A., Cui, Y., Shaikhutdinov, S. & Freund, H.-J. Stabilization of Ultrathin Zinc Oxide Films on Metals: Reconstruction versus Hydroxylation. *J. Phys. Chem. C* **119**, 7842–7847 (2015).
- [168] Lauritsen, J. V. *et al.* Stabilization Principles for Polar Surfaces of ZnO. *ACS Nano* **5**, 5987–5994 (2011).
- [169] Benedetti, S. *et al.* Spectroscopic identification of the chemical interplay between defects and dopants in Al-doped ZnO. *Phys. Chem. Chem. Phys.* **19**, 29364–29371 (2017).
- [170] Cho, D.-Y. *et al.* Spectroscopic evidence for limited carrier hopping interaction in amorphous ZnO thin film. *Appl. Phys. Lett.* **95**, 261903 (2009).
- [171] Guglieri, C. & Chaboy, J. O K-Edge X-ray Absorption Spectroscopy in Al-Doped ZnO Materials: Structural vs Electronic Effects. *J. Phys. Chem. C* **118**, 25779–25785 (2014).
- [172] Brune, H., Bales, G. S., Jacobsen, J., Boragno, C. & Kern, K. Measuring surface diffusion from nucleation island densities. *Phys. Rev. B* **60**, 5991–6006 (1999).
- [173] Sarasamak, K., Limpijumnong, S. & Lambrecht, W. R. L. Pressure-dependent elastic constants and sound velocities of wurtzite SiC, GaN, InN, ZnO, and CdSe, and their relation to the high-pressure phase transition: A first-principles study. *Phys. Rev. B* **82**, 035201 (2010).
- [174] Samsonov, G. V. *Handbook of the Physicochemical Properties of the Elements* (Springer, Boston, MA, 1968).

Bibliography

- [175] Sakudo, T. & Unoki, H. Dielectric Properties of SrTiO₃ at Low Temperatures. *Phys. Rev. Lett.* **26**, 851–853 (1971).
- [176] Müller, K. A. & Burkard, H. SrTiO₃ : An intrinsic quantum paraelectric below 4 K. *Phys. Rev. B* **19**, 3593–3602 (1979).
- [177] Joseph, M., Tabata, H. & Kawai, T. Ferroelectric behavior of Li-doped ZnO thin films on Si(100) by pulsed laser deposition. *Appl. Phys. Lett.* **74**, 2534 (1999).
- [178] Maiz, J. *et al.* Ferroelectricity in Undoped ZnO Nanorods. *J. Phys. Chem. C* **123**, 29436–29444 (2019).
- [179] Novoselov, K. S. *et al.* Electric Field Effect in Atomically Thin Carbon Films. *Science* **306**, 666–669 (2004).
- [180] Avila, J. *et al.* Exploring electronic structure of one-atom thick polycrystalline graphene films: A nano angle resolved photoemission study. *Sci. Rep.* **3**, 2439 (2013).
- [181] Endlich, M., Molina-Sánchez, A., Wirtz, L. & Kröger, J. Screening of electron-phonon coupling in graphene on Ir(111). *Phys. Rev. B* **88**, 205403 (2013).
- [182] Giovannetti, G. *et al.* Doping Graphene with Metal Contacts. *Phys. Rev. Lett.* **101**, 026803 (2008).
- [183] Khomyakov, P. A. *et al.* First-principles study of the interaction and charge transfer between graphene and metals. *Phys. Rev. B* **79**, 195425 (2009).
- [184] Pletikosić, I. *et al.* Dirac Cones and Minigaps for Graphene on Ir(111). *Phys. Rev. Lett.* **102**, 056808 (2009).
- [185] Rusponi, S. *et al.* Highly Anisotropic Dirac Cones in Epitaxial Graphene Modulated by an Island Superlattice. *Phys. Rev. Lett.* **105**, 246803 (2010).
- [186] Sutter, P., Sadowski, J. T. & Sutter, E. Graphene on Pt(111): Growth and substrate interaction. *Phys. Rev. B* **80**, 245411 (2009).
- [187] Walter, A. L. *et al.* Electronic structure of graphene on single-crystal copper substrates. *Phys. Rev. B* **84**, 195443 (2011).
- [188] Cushing, G. W., Johánek, V., Navin, J. K. & Harrison, I. Graphene Growth on Pt(111) by Ethylene Chemical Vapor Deposition at Surface Temperatures near 1000 K. *J. Phys. Chem. C* **119**, 4759–4768 (2015).
- [189] Merk, D. C. *Transfer of Graphene under Ultra-High Vacuum*. Ph.D. thesis, EPFL, Lausanne (2022).
- [190] Losurdo, M., Giangregorio, M. M., Capezzuto, P. & Bruno, G. Graphene CVD growth on copper and nickel: Role of hydrogen in kinetics and structure. *Phys. Chem. Chem. Phys.* **13**, 20836 (2011).

-
- [191] Cho, J. *et al.* Atomic-Scale Investigation of Graphene Grown on Cu Foil and the Effects of Thermal Annealing. *ACS Nano* **5**, 3607–3613 (2011).
- [192] Marsden, A. J. *et al.* Is graphene on copper doped? *Phys. Status Solidi RRL* **7**, 643–646 (2013).
- [193] Ullah, S. *et al.* Graphene transfer methods: A review. *Nano Res.* **14**, 3756–3772 (2021).
- [194] Natterer, F., Patthey, F. & Brune, H. Quantifying residual hydrogen adsorption in low-temperature STMs. *Surf. Sci.* **615**, 80–87 (2013).
- [195] Uchoa, B., Yang, L., Tsai, S.-W., Peres, N. M. R. & Neto, A. H. C. Orbital symmetry fingerprints for magnetic adatoms in graphene. *New J. Phys.* **16**, 013045 (2014).
- [196] Pivetta, M. *et al.* Measuring the Intra-Atomic Exchange Energy in Rare-Earth Adatoms. *Phys. Rev. X* **10**, 031054 (2020).
- [197] Pivetta, M., Rusponi, S. & Brune, H. Direct capture and electrostatic repulsion in the self-assembly of rare-earth atom superlattices on graphene. *Phys. Rev. B* **98**, 115417 (2018).
- [198] Al Taleb, A., Yu, H. K., Anemone, G., Farías, D. & Wodtke, A. M. Helium diffraction and acoustic phonons of graphene grown on copper foil. *Carbon* **95**, 731–737 (2015).
- [199] Al Taleb, A., Anemone, G., Farías, D. & Miranda, R. Resolving localized phonon modes on graphene/Ir(111) by inelastic atom scattering. *Carbon* **133**, 31–38 (2018).
- [200] Chen, L., Huang, Z. & Kumar, S. Phonon transmission and thermal conductance across graphene/Cu interface. *Appl. Phys. Lett.* **103**, 123110 (2013).
- [201] Cocemasov, A. I., Nika, D. L. & Balandin, A. A. Phonons in twisted bilayer graphene. *Phys. Rev. B* **88**, 035428 (2013).
- [202] King, A., Johnson, G., Engelberg, D., Ludwig, W. & Marrow, J. Observations of Intergranular Stress Corrosion Cracking in a Grain-Mapped Polycrystal. *Science* **321**, 382–385 (2008).
- [203] He, R. *et al.* Observation of Low Energy Raman Modes in Twisted Bilayer Graphene. *Nano Lett.* **13**, 3594–3601 (2013).
- [204] Jorio, A. & Cançado, L. G. Raman spectroscopy of twisted bilayer graphene. *Solid State Commun.* **175–176**, 3–12 (2013).
- [205] Yan, J.-A., Ruan, W. Y. & Chou, M. Y. Phonon dispersions and vibrational properties of monolayer, bilayer, and trilayer graphene: Density-functional perturbation theory. *Phys. Rev. B* **77**, 125401 (2008).
- [206] Bilgeri, T. *Quantum Dynamics in Individual Surface Spins*. Ph.D. thesis, EPFL, Lausanne (2021).

Bibliography

- [207] Bader, R. & Bader, R. *Atoms in Molecules: A Quantum Theory*. International Series of Monographs on Chemistry (Clarendon Press, 1990).

Boris Sorokin

04.11.1991, Russian

EDUCATION

- **Ph.D. Physics** *2022*
École Polytechnique Fédérale de Lausanne (EPFL)
- **M.S. Applied Mathematics and Physics** *2015*
Moscow Institute of Physics and Technology (MIPT)
- **B.S. Applied Mathematics and Physics** *2013*
Moscow Institute of Physics and Technology (MIPT)

EXPERIMENTAL TECHNIQUES

- **Main:** X-ray magnetic circular dichroism, XAS, XLD
- **Surface characterisation:** LEED, Auger spectroscopy, Raman spectroscopy
- **Auxiliary:** ultra-fast XAS and XES, FMR, ESR

SCIENTIFIC INTERESTS

- **Main:** single-atom magnets, 2D magnets, magnetism of nanostructures, single-molecule magnets
- **Auxiliary:** spin dynamics, ultrafast demagnetisation, quantum computing

IT SKILLS

MATLAB, Python, Linux (BASH), multiplet simulations (multiX and Quanta), LaTeX, OriginPro, Ansys High Frequency Structural Simulator (HFSS), Wolfram Mathematica, Lua

PROFESSIONAL EXPERIENCE

- **Maloja Group, PSI** *2022 - present*
Postdoctoral Fellow
- **Laboratory of Nanostructures at Surfaces (LNS), EPFL** *2018 - 2022*
Doctoral assistant
- **Laboratory of Ultrafast Spectroscopy (LSU), EPFL** *2016 - 2018*
Doctoral assistant
- **Laboratory of Magnetic Resonance and Spin Relaxation in Solids, IRE RAS (Moscow)** *2012 - 2015*
Engineer

LANGUAGES

- English (advanced, C1)
- French (intermediate, B2)
- German (basic, A2)
- Russian (mother tongue, C2)

PUBLICATIONS

- **Sorokin, B. V.**, Pivetta, M., Merk, D., Reynaud, S., Bellini, V., Barla, A., Brune, H. & Rusponi, S. Magnetic stability of Dy and Ho single atoms on alkaline earth oxides. *ACS Nano*, in preparation (2022).
- Bellini, V., Rusponi, S., Kolorenč, J., Mahatha, S. K., Valbuena, M., Persichetti, L., Pivetta, M., **Sorokin, B. V.**, Merk, D., Reynaud, S., Sblendorio, D., Stepanow, S., Nistor, C., Gargiani, P., Betto, D., Mugarza, A., Gambardella, P., Brune, H., Carbone, C. & Barla, A. Slow magnetic relaxation of Dy adatoms with in-plane magnetic anisotropy on a two-dimensional electron gas. *ACS Nano*, in press (2022).
- Kinschel, D., Bacellar, C., Cannelli, O., **Sorokin, B.**, Katayama, T., Mancini, G. F., Rouxel, J. R., Obara, Y., Nishitani, J., Ito, H., Ito, T., Kurahashi, N., Higashimura, C., Kudo, S., Keane, T., Lima, F. A., Gawelda, W., Zalden, P., Schulz, S., Budarz, J. M., Khakhulin, D., Galler, A., Bressler, C., Milne, C. J., Penfold, T., Yabashi, M., Suzuki, T., Misawa, K. & Chergui, M. Femtosecond X-ray emission study of the spin cross-over dynamics in haem proteins. *Nat. Commun.* **11**, 4145 (2020).
- Atsarkin, V. A., **Sorokin, B. V.**, Borisenko, I. V., Demidov, V. V. & Ovsyannikov, G. A. Resonance spin-charge phenomena and mechanism of magnetoresistance anisotropy in manganite/metal bilayer structures. *J. Phys. D: Appl. Phys.* **49**, 125003 (2016).
- Atsarkin, V. A., Demidov, V. V. & **Sorokin, B. V.** Resonance dc phenomena in manganite thin films. *Magn. Reson. Solids* **16**, 14201 (2014).
- Atsarkin, V. A. & **Sorokin, B. V.** Magnetoresonance EMF in Thin Manganite Films. *J. Exp. Theor. Phys.* **119**, 567 (2014).
- Chelyshev, Y., Gafurov, M., Ignatyev, I., Zanochnik, A., Mamin, G., **Sorokin, B.**, Sorokina, A., Lyapkalo, N., Gizatullina, N., Mukhamedshina, Y. & Orlinskii, S. Paramagnetic manganese in the atherosclerotic plaque of carotid arteries. *Biomed Res. Int.* **2016**, 3706280 (2016).

TALKS

- **Sorokin, B. V.** Atsarkin, V. A., Demidov, V.V. & Borisenko, I. V. Resonance spin-charge phenomena in manganite thin films in the neighborhood of the phase transition. Youth school-conference ‘*Spinus – 2014, Magnetic resonance and its applications*’, St Petersburg, Russia (2014).

CONFERENCES, WORKSHOPS and DOCTORAL SCHOOLS

- Ultrafast X-ray Summer School, Hamburg (Germany), 12-15 June 2017.
- X-ray Spectroscopy of Magnetic Materials workshop, ESRF, Grenoble (France), 7-9 October 2019.
- 5th Italian School of Magnetism, Rome (Italy), 3-7 February 2020.